

Molecular Dynamics Simulation of Cluster Ion Impact on Solid Surface

Takaaki Aoki

January 2000

Abstract

In this thesis, the impact process of cluster ions on solid surfaces was studied using molecular dynamics (MD) simulation. Cluster is an aggregated material which consists of a few to thousand atoms. The impact process of cluster ion on solid surface is of great interest because the effect of impact by cluster ion cannot be explained by the summation of individual monomer ions, and it is termed as ‘nonlinear effect.’ In order to understand the nonlinear effect by cluster, the dynamics of collisional process between cluster and solid surface should be examined. MD simulation is one method of computer simulation to solve numerically the Newton’s equation of motion for each atom in the system using difference equation technique, so MD can make it possible to trace the time evolution of coordinates and velocity for every atom with high resolution.

The basic theory of molecular dynamics and the acceleration method are described in chapter 2. For this study, the original MD program was developed, which can accelerate the calculation speed of collisional process of high-energy atoms with a solid surface by applying different timestep to each atom depending on its velocity. Due to this acceleration technique and recent progress in computers, it can be possible to simulate the system with a large number of atoms, or more than hundred simulations in order to obtain statistics.

In the following chapters, MD simulation is used to examine the impacts of various types of clusters on a number of well defined substrates. Chapter 3 describes the typical impact process of cluster on solid surface examined using large argon cluster and silicon substrate. The differences between cluster and monomer impact are shown in penetration range, damage formation and sputtering. The energy dependence of penetration depth of cluster was examined and it was found that the penetration depth is pro-

portional to the cube root of the incident energy. This is due to a large number of collisions between cluster atoms and surface atoms, which cause isotropic propagation of incident energy. Through this multiple-collision process, a crater-shaped damage is formed on the surface.

In chapter 4, the impacts of carbon cluster onto carbon substrate are examined both by MD simulation and experimentally. Carbon is a suitable material to generate well-defined small size clusters such as C_7 , C_{19} and C_{60} in experiments. It was found that the penetration depth of carbon clusters with several keV/atom is similar to that of monomer ion, but a larger number of displacements are formed with the cluster size of larger than 10. From this study, the boundary size of cluster size where a cluster shows the nonlinear effect is discussed.

Shallow junction formation by boron cluster implantation into silicon substrate is discussed in chapter 5. Decaborane ($B_{10}H_{14}$) is a stable material of boron cluster and each boron atom can be irradiated with 1/10 energy of the total acceleration energy. This implies that the low-energy implantation can be obtained easily. The penetration depth by $B_{10}H_{14}$ is shown to be the same as that by boron monomer ions with same acceleration energy per atom. Furthermore, it is found that $B_{10}H_{14}$ implantation can form larger number of displacements in the near surface region, with lower atomic dose than monomer ions. The high-yield damage formation on the surface suggested to suppress the transient enhanced diffusion (TED). These properties of $B_{10}H_{14}$ implantation are considered as advantageous for small LSI fabrication.

In chapter 6, the impact of fluorine cluster and neon cluster onto silicon substrate are compared, in order to examine the sputtering effect by reactive cluster ion. Fluorine cluster shows higher sputtering yield than both fluorine atom and neon cluster at low energy region. It is suggested that the high-density atomic and energy deposition by cluster ion impact prompt the formation of volatile silicon-fluoride materials and desorption of fluoride materials. As the incident energy increases, fluorine and neon cluster shows similar sputtering yield because the physical sputtering effect through atomic collisions is major effect in high energy region.

From these results, characteristics of cluster ion impact depending on

incident energy, cluster size and cluster and substrate species are discussed.

Acknowledgments

The author would like to express his deep gratitude to Professor Isao Yamada of Kyoto University for his continuous guidance and encouragement throughout this study. The author also would like to express his thanks and gratitude to the following people:

- Professor Nobutsugu Imanishi of Kyoto University for his helpful comments and discussion on the manuscript.
- Associate Professor Gikan Takaoka for many helpful comments.
- Research Associate Jiro Matsuo and Visiting Professor Zinetulla Insepov for invaluable assistance and stimulating discussions in this study.
- Visiting Professor Rafael Manory for helpful comments in correcting and improving the English in this thesis.

This research was made possible by cooperation and assistance of many students and research fellows at Kyoto University. The author would like to thank:

- Dr. Daisuke Takeuchi, Dr. Makoto Akizuki and Dr. Noriaki Toyoda for fruitful discussions.
- Mr. Hiroaki Kitani and Mr. Masahiro Tanomura for helpful discussions and continuous encouragement in this work.

As well, the assistance of Mr. Takuya Kusaba, Mr. Masahiro Saito, Mr. Shun-ichi Chiba was also very helpful to this study and the author wishes to express appreciation to them and to all members of Ion Beam Engineering Experimental Laboratory in Kyoto University.

To Mr. Toshio Seki, I would like to show deep gratitude for continuous cooperation and encouragement during our nine years of student life in Kyoto University.

Finally, I especially thank my parents and brother for their kind care, support and encouragement.

Contents

1	Introduction	1
1.1	Kinetics in Macro and Microscopic Scale	1
1.2	Atomic Collisional Processes in Solids	2
1.3	Cluster Ion Impact and the Nonlinear Effect	3
1.4	Computer Simulation of Atomic Collision	4
1.5	Purpose of Study and Structure of the Thesis	6
2	Development of MD Program for Atomic Collisions	9
2.1	Integration Algorithm	9
2.2	Interatomic Forces	10
2.2.1	Potential Models	10
2.2.2	Cut-off Radius	16
2.3	Boundary Conditions	17
2.3.1	Periodic Boundary Conditions	17
2.3.2	Temperature Control	20
2.4	Acceleration Methods for MD Calculations	22
2.4.1	Book-keeping Method	22
2.4.2	Linked Cell Method	22
2.4.3	Different Time-step Method	24
3	Impact Processes of Cluster Ions	29
3.1	Introduction	29
3.2	Simulation Model	29
3.3	The Impact Processes of Monomer and Cluster Ions	30
3.3.1	Monomer Ion Impact	30
3.3.2	Cluster Ion Impact	31
3.3.3	Multiple-collision Effect and Thermalization	34

3.4	Energy and Size Dependence of Penetration Depth	37
3.4.1	Energy-per-atom Dependence	37
3.4.2	Total Energy Dependence	40
3.4.3	Cluster Size Dependence	41
3.5	Damage Formation and Lateral Sputtering	42
3.5.1	Damage Formation Mechanism by Cluster Impact	42
3.5.2	Size Dependence of Damage Formation	43
3.5.3	Lateral Sputtering	46
3.6	Summary	50
4	Nonlinear Effects by High-energy Cluster Impact	53
4.1	Introduction	53
4.2	Simulation Model	54
4.3	The Penetration Process of C_{60} into Diamond	56
4.3.1	Penetration Depth of C_{60}	56
4.3.2	Clearing-way Effect	58
4.3.3	Multiple-collision Effect	58
4.3.4	Nonlinearity in Stopping Power	59
4.3.5	Damage Formation by C_{60} Impact	65
4.4	Cluster-size Effect on Small Carbon Cluster Impact	70
4.4.1	MD Simulation of Small Carbon Cluster Impact	70
4.4.2	Overlapping Model for Damage Formation by Small Cluster Impact	72
4.4.3	STM Observation of the Damage Formation by Clus- ter Ion Impact	74
4.5	Summary	76
5	Shallow Implantation by Boron Cluster Ions	79
5.1	Introduction	79
5.2	Simulation Model	80
5.3	Implant Profile and Efficiency	82
5.4	Damage Formation by Boron Cluster Impact	85
5.4.1	Time Evolutions of Damage Formation	85
5.4.2	Depth Profile	88

5.5	Summary	90
6	Reactive Sputtering by Fluorine Cluster Impact	93
6.1	Introduction	93
6.2	Simulation Model	96
6.3	Penetration and Sticking Mechanism	97
6.3.1	The Impact Event	97
6.3.2	Sticking Probability	99
6.4	Sputtering Effect	101
6.4.1	Sputtering Yield	101
6.4.2	Sputtered Species	102
6.4.3	High Performance Etching by Reactive Cluster Ion .	105
6.5	Summary	105
7	Summary and Conclusions	109
	References	115

List of Figures

2.1	Modified potential curve of the repulsive part in Tersoff potential model for high-energy atomic collision.	17
2.2	Schematic of 2-dimensional periodic boundary condition. . .	18
2.3	Schematic diagram of mapping method under 1-dimensional periodic boundary condition.	18
2.4	Boundary conditions of MD simulation in this study.	19
2.5	Schematic of linked cell method.	23
2.6	Flowchart of the different time-step method.	26
2.7	Relationship between the estimated and achieved acceleration ratio by different time-step method.	27
2.8	Velocity distribution of Si substrate atoms at 300K.	27
3.1	Snapshots of Ar monomer with 7keV impacting on Si(001). .	31
3.2	Snapshots of Ar ₆₈₈ with 10eV/atom impacting on Si(001). .	32
3.3	STM images of Si(111) surface irradiated with Ar cluster ions. .	33
3.4	Snapshots of Ar ₆₈₈ impacting on Si(001) with various incident energies, 3.85ps after impact.	35
3.5	Time dependence of the total kinetic energy and the penetration depth of Ar ₆₈₈ cluster.	36
3.6	Kinetic energy distribution of re-evaporated Ar cluster atoms, 3.85ps after impact.	37
3.7	Energy-per-atom dependence of the maximum penetration depth of Ar ₄₃ and Ar ₆₈₈ cluster.	38
3.8	Energy dependence of the crater diameters with Ar cluster ions on Au surfaces, measured by STM.	39
3.9	Total energy dependence of the maximum penetration depth of Ar clusters.	40

3.10	Cluster size dependence of the maximum penetration depth of Ar clusters.	41
3.11	Compression and relaxation process in damage formation by Ar ₆₈₈ (10eV/atom) impact.	43
3.12	Profiles of damage formed by Ar ₁₃ , Ar ₄₃ and Ar ₆₈₈ with the same total incident energy of 7keV.	44
3.13	Penetration-depth dependence of the transitional kinetic energy of Ar cluster and Si substrate, and the potential energy of Si.	45
3.14	Model of damage formation process by large and small cluster impact.	47
3.15	Snapshots of Ar ₆₈₈ with 80eV/atom impacting on Si(001) substrate.	48
3.16	Energy and momentum profile at the impact of Ar ₆₈₈ with 80eV/atom.	49
3.17	Kinetic energy distribution of substrate atoms, irradiated with Ar ₆₈₈ (80eV/atom) cluster, 1.2ps after impact.	49
4.1	Snapshots of C ₁ and C ₆₀ impacting on diamond (001) surface, 0.1ps after impact.	55
4.2	Energy dependence of the penetration depth of C ₆₀ and C ₁ into diamond.	57
4.3	Penetration depth dependence of the ratio of lateral component of kinetic energy to the total kinetic energy.	59
4.4	Kinetic energy loss and stopping power of C ₆₀ impacting on a diamond substrate.	60
4.5	Classification of the nonlinearity in the stopping power at C ₆₀ impact.	61
4.6	Schematic model of the transformation of stopping power by the clearing-way effect.	62
4.7	Schematic model of the transformation of stopping power by the multiple-collision effect.	63
4.8	Profiles of shadow cones formed by carbon atoms impacting on a diamond substrate with various incident energies.	64

4.9	Time dependence of the number of displacements per one carbon atom formed by irradiation of C_{60} and C_1 with the energy of 200eV/atom, 500eV/atom or 2keV/atom.	66
4.10	Incident energy dependence of the number of displacements formed by C_{60} and C_1	66
4.11	Depth profile of displaced carbon atoms in diamond by C_{60} and C_1 impacting with 200eV/atom and 2keV/atom, 0.1ps after impact.	68
4.12	Atomic dose dependence of the number of displaced Al atoms in sapphire irradiated with C_{60} and C_2 , measured by RBS.	69
4.13	Snapshots of various sizes of cluster ion impacting on HOPG surface with the energy of 2keV/atom.	70
4.14	Time dependence of the number of displacements on the surface induced by various sizes of carbon clusters.	71
4.15	Size dependence of the number of displacements on the surface at 0.05ps and 0.1ps after the impact.	72
4.16	Schematic of the ‘overlapping model’ to explain nonlinear damage formation effect by cluster impact.	73
4.17	STM images of HOPG substrate irradiated with various sizes of carbon clusters.	75
4.18	Cluster size dependence of the trace area on HOPG surface, measured by STM.	76
5.1	Structures and orientations at impact of B_1 , B_2 , B_4 and B_{10} prepared for MD simulation.	81
5.2	Implant profile and efficiency of B atom implantation by B_1 , B_2 , B_4 and B_{10}	82
5.3	Implant profile of B atoms by vertical B_{10} chain cluster according to the initial position in the cluster.	84
5.4	Schematic model of the implant process by vertically-stacked B cluster.	84
5.5	Time dependence of the number of displacements per B atom by B clusters with various sizes.	86

5.6	Time dependence of the mean kinetic energy of B atom at the impact of B ₁ and B ₁₀	86
5.7	Snapshots of B ₁ and B ₁₀ impacting on Si(001) surface, 0.16ps and 8ps after impact.	88
5.8	Depth profile of displaced Si atoms by the impact of B ₁ , B ₄ and B ₁₀ on Si(001) surface, 0.16ps and 8ps after impact. . .	89
6.1	Sputtering yield by Ar monomer, Ar cluster and SF ₆ cluster impact to various target materials.	94
6.2	QMS mass spectra after introducing SF ₆ cluster and during SF ₆ cluster ion irradiation on Si substrate with the total energy of 20keV.	95
6.3	Snapshots of (F ₂) ₃₀ cluster impacting on bare Si(001) surface at 1, 10 and 100eV/atom taken at 0, 0.15, 1.5 and 8ps after impact.	98
6.4	Incident energy dependence of the sticking probability of F, F ₂ and (F ₂) ₃₀ to bare Si surface and Si mono-fluoride surface, 8ps after impact.	99
6.5	Incident energy dependence of the Si sputtering yield of F, F ₂ , (F ₂) ₃₀ , Ne and Ne ₆₀ to bare Si surface, and Si mono-fluoride surface, 8ps after impact.	101
6.6	Incident energy dependence of the sputtering yield of Si atoms with or without F, at the impact of (F ₂) ₃₀ on Si(001) surface.	102
6.7	Distribution of sputtered species by F and Ne cluster.	103
6.8	Depth profile of displaced Si atoms at the impact of F ₁ , F ₂ and (F ₂) ₃₀ with various energies, 8ps after impact.	106
6.9	Relationship between the mean damage depth and the sputtering yield by F ₁ , F ₂ and (F ₂) ₃₀ impact.	107

List of Tables

2.1	Parameters of Stillinger-Weber potential for silicon.	13
2.2	Parameters of Stillinger-Weber potential for fluorine–fluorine and silicon–fluorine.	15
2.3	Parameters of Tersoff potential model for carbon.	16
5.1	Mean implant depth and implant efficiency of boron cluster.	83

Chapter 1

Introduction

1.1 Kinetics in Macro and Microscopic Scale

In the 17th century, the motion of celestial bodies was the subject of most interest among scientists. Numerous data were collected with careful observation by Tycho Brahe, Kepler and Galilei. From these results, Kepler and Galilei determine a number of laws about motion of objects.

Sir Isaac Newton, the most famous physicist and mathematician in the 17-18th centuries, proposed three laws about motion and described his idea using a new mathematical concept developed by himself¹⁾. First, he explicitly defined the parameters such as coordinates, velocity and acceleration, in order to describe the motion of an object. Then, he formulated the relationships between these parameters in the manner of differential equations. In these works, he introduced a simple formula of force between two objects, which is proportional to the product of masses of two objects and to the inverse square of the distance (r_a) between them. His theory and mathematical method were successful in explaining the motion of celestial and other objects. For example, he proved that, if the motion of two bodies is governed by a force which depends on r_a^{-2} , their trajectories give an ellipse, parabola or hyperbola curve: this is a generalization of Kepler's law²⁾.

Another system in which a physical phenomenon is described as the motion of isolated objects was found on a very small scale, about the order of 10^{-9}m . During the middle 19th to the early 20th century, the kinetic theory of gases based on atomism was established by Maxwell, Boltzmann and Einstein. On the other hand, many experiments were done to prove the

existence of atoms and molecules by Perrin et al. Geiger and Marsden³⁾ made experiments of α -ray collision on gold film and Rutherford⁴⁾ explained the structure of the atom from their results. As the atomic hypothesis became explicit, the material began to be considered as a bulk of small and rigid particles. The properties of materials started to be analyzed with the consideration of interactions between many atoms, instead of continuous properties such as density, temperature and pressure.

1.2 Atomic Collisional Processes in Solids

The motion of energetic atoms in a solid is an attractive subject not only for physics but also for materials engineering because the collisional process provides the method to control the composition and structure of materials. In order to understand the motion of atoms in solids, it is essential to find suitable descriptions of the forces between atoms. Unlike celestial objects in space, the nucleus is usually surrounded by electrons which cause the ‘screening effect.’ The motion of electrons in such a small scale became to be understood by the development of quantum mechanics in the early 20th century, which is based on the solution to the Schrödinger equation deals with the ‘duality’ of electrons as waves or as particles. This was a new and different concept from classical Newtonian mechanics. Inter-atomic force including electrons was studied using quantum mechanics by many physicists such as Bohr⁵⁾, Thomas⁶⁾, Fermi⁷⁾ and Firsov⁸⁾. Additionally, incident atoms also interact with free electrons in the material and affected electrons can be excited, which is termed as ‘electronic stopping.’ Lindhard and Scharff⁹⁾ developed the electronic stopping theories based on the Thomas-Fermi model. Due to the complexity of the mechanisms affecting one atom, these interatomic forces cannot be solved analytically except in some specific cases.

In collisional process of ions in solid, there usually is a contribution of multiple atoms differently from atoms in gases. This is also one of the more difficult points to analyze the collisional process of atoms. However, at middle incident energy range (1-100keV), it is possible to consider the impact process as a sequence of the collisions of a projectile atom and one

target atom in a solid. This ‘binary collision’ approximation is supported by the fact that the range of significant interatomic force for the collision is shorter than distances of target atoms in the bulk because of the screening effect, and the collisional process lasts for times in the order of 10^{-15} s, which is much less than the lattice vibration period of atoms.

Under the binary collision approximation, the impact parameter, which is given by the initial coordinates of projectile and target atoms, for each collision and collision frequency can be given randomly from the density of materials. Lindhard, Scharff and Schiøtt solved this stochastic process analytically and succeeded to obtain the implant range and distribution of implanted atoms in a solid¹⁰⁾. The possible effects occurring during the irradiation of a substrate are point defects formation (creation of vacancies or interstitials), removal of atoms from the surface (sputtering), as well as physical and chemical adsorption. Sigmund¹¹⁾ proposed a linear cascade theory, which is based on the assumption that the energetic atoms including both projectile and knocked-on target atom do not interact with each other but only collide with a static target atom. He developed the equation of transport of an energetic target atom in the solid and derived the formula to explain the sputtering yield depending on incident energy of the projectile.

These theories showed good agreement with experimental results and contributed to the progress of the ion beam engineering in industrial application such as ion implantation and ion beam sputtering.

1.3 Cluster Ion Impact and the Nonlinear Effect

Cluster, an aggregate consisting of a few to thousand atoms, is an interesting topic of study because of its different properties from both atomic and bulk states. The collisional process of a cluster also shows the interesting so-called ‘nonlinear’ effect. ‘Nonlinear’ means that the effect of cluster impact cannot be explained by summation of the single ion effect. For example, Benguerba et al. irradiated with gold cluster having the size ranging 1 to 5 on organic and metallic targets, and they found that the yield of secondary ion emission per atom is largely enhanced by cluster irradiation compared with a monomer with the same energy-per-atom¹²⁾.

The nonlinear effect of cluster impact has been introduced into industrial use in various studies by Yamada and co-workers at Kyoto University^{13, 14, 15)}. They developed a high current gas cluster ion source and showed that the irradiation by large gas clusters, Ar, O₂ and SF₆ with mean size of about 2000, can be used for high-quality thin film formation^{16, 17)}, surface smoothing^{18, 19)} and etching²⁰⁾ processes. On the other hand, it was found that shallow implantation can be achieved by decaborane (B₁₀H₁₄) implantation with ten times higher acceleration energy than conventional B monomer ion implantation and high-performance small p-MOS with 40nm of gate length can be fabricated^{21, 22)}. These results indicate that the cluster ion process has many advantages compared to the monomer ion beam process.

The collisional process between a cluster and a solid surface is still not understood as well as that of a single atom, because the collisional process depends on a cluster size, shape and density, which are not necessary for a single atom impact. In case of the collision of a cluster with a solid, interactions among more than three atoms should be considered, so that a simple binary collision approximation cannot be applied for analyzing the collisional process of cluster. It was shown that, if a cluster is considered as one large and heavy particle, the stopping parameters of the cluster can be calculated by introducing a correlation function to describe shape and density of the cluster²³⁾. However, it is hard to describe the evolution of the correlation function itself, i.e. when a cluster collapses and the nonlinear effect is lost. Because of the various new technological applications of cluster ion beam technique, it is an issue of high priority to establish a theory for the dynamics of cluster impacts on solid targets.

1.4 Computer Simulation of Atomic Collision

Due to the advancements in computers, it became possible to calculate the trajectory of a high energy ion directly and to derive statistical properties of ion irradiation through a certain number of trials. The binary collision process was studied using Monte-Carlo (MC) computer simulation by Oen²⁴⁾, Robinson²⁵⁾, Biersack²⁶⁾ and Ziegler²⁷⁾. These simulations basically rep-

resent the Lindhald and Sigmund theory mentioned in the section 1.2; the impact parameter and mean free path are given randomly and interactions between high-energy projectile and knocked-on atoms are ignored. MC simulations made it possible to examine the evolution of a collision cascade, the formation of damage as well as ion-beam mixing and sputtering, not only for a single, but also complex materials, which is a more difficult case to be solved analytically.

Binary collision simulations were successful in analyzing the impact process of a single atom, however, as mentioned previously, this method is not available for analyzing the cluster impact process. In order to analyze the collision of cluster and solid, it is required to describe the motion of all atoms concerned in the collisional process, and to establish and solve numerically the Newton's equation of motion for all atoms in the system. This method is termed as 'molecular dynamics (MD)' simulation. The concept of MD is simple but longer computational time and larger memory resources are required than the MC method based on binary collision theory. However, MD simulation can provide atomic and structural information which is not possible by other methods, such as channeling effect, and time and space evolution of atomic coordinates in the order of fs to ps, which are like *in-situ* and real-time observations. The idea of MD simulation was proposed by Alder and Wainwrite in 1957²⁸⁾ and they found the phase transition mechanism of hard-sphere particles in 1959²⁹⁾. Rahman³⁰⁾ and Verlet³¹⁾ simulated about thousand argon atoms in liquid phase using Lennard-Jones potential model and showed good agreement in thermodynamical properties under various temperature and pressure conditions between 'real' and 'computer' experiments.

The analysis of the collisional process of cluster ion using MD simulation started in around 1990. Shulga³²⁾, Averback³³⁾ and Insepov³⁴⁾ performed MD simulations and explained the nonlinearity of cluster impact depending on the particle (mass ratio of cluster to target atom), cluster size and incident energy. As the performance of computers was improved and the price decreased, larger and more complex systems can be treated by MD simulations. Recently, Moseler et al.³⁵⁾ simulated the cluster ion deposition through sequential irradiation. The system in simulation rapidly ap-

proaches the real experimental condition and the nonlinear effects of cluster impact can be analyzed more precisely by computer simulation.

1.5 Purpose of Study and Structure of the Thesis

As mentioned in section 1.3, the cluster ion beam process is expected to provide a solution to the problems which arise in the conventional ion beam engineering. In order to apply the cluster ion beam to the industrial field, it is important to establish the theoretical background about cluster ion impact. This study is aimed to understand the nonlinear collisional process of cluster ion impact using molecular dynamics (MD) simulation. The structure of the thesis is as follows:

The basic theory of MD is described in chapter 2. MD simulation is a suitable method to analyze the atomic collisional process with high time and space resolution, but it requires longer calculation time than the Monte-Carlo method under binary collision approximation. Chapter 2 describes the design of MD simulation for atomic collisions and explains the method to accelerate the MD calculation which is especially useful for the collisions between high-energy particles and static solid target atoms.

In the following chapters, MD simulation is used to examine the impacts of various types of clusters on a number of well defined substrates. In chapter 3 and 4, basic characteristics about cluster ion impact are discussed by MD simulations of argon and carbon clusters. Chapter 3 deals with the impact process of Ar cluster on Si solid surface, because it is an inert gas with no chemical reaction with the surface. The effect observed with Ar cluster will reveal effects of mass and energy impact with no effects of chemical identity of the ion. The differences between cluster and monomer impact are shown in penetration range, damage formation and sputtering. In chapter 4, the impact of carbon cluster onto a carbon substrate is examined. Experiments of carbon cluster irradiation were also performed under similar condition of energy, cluster size and species to MD. The simulation and experimental results are compared and the size dependence of implantation range and damage formation yield at the energy range of several keV/atom are discussed.

Chapter 5 deals with shallow junction formation by B cluster implantation. Decaborane ($B_{10}H_{14}$) is a stable molecule which can be considered as a boron cluster and it has been shown that the low-energy implantation can be obtained easily using $B_{10}H_{14}$. By MD simulations of small B cluster implantation, the penetration depth, implant efficiency and damage formation are examined and the advantages of cluster ion implantation from the view point of LSI fabrication.

In chapter 6, the sputtering effect by reactive cluster ions is examined. It has been observed that higher sputtering yield can be achieved by reactive cluster ion impact, such as SF_6 cluster on Si target, because high-density atomic irradiation high-density energy deposition effect. The impacts of fluorine and neon cluster onto silicon substrate are compared using MD simulations. The energy dependence of sputtering yield and distribution of sputtered products are examined and the sputtering mechanism by reactive cluster ions is discussed.

From these results, characteristics of cluster ion impact depending on incident energy, cluster size and cluster and substrate species are summarized in chapter 7.

Chapter 2

Development of MD Program for Atomic Collisions

In this chapter, the elemental topics about MD methods, such as integration algorithm, potential model and boundary conditions are explained. The original MD code ‘*MDsim*’ was developed for this study. We also discuss the acceleration and optimization methods for the MD simulation for high-energy atomic impact on a solid target.

2.1 Integration Algorithm

Molecular dynamics (MD) is the way to calculate the time evolution of atomic coordinates by solving differential equation numerically³⁶⁾. An object in a system moves under Newton’s law of motion. The classical Newton’s equation of motion for an object in the system²⁾ is given by

$$\frac{d\mathbf{v}(t)}{dt} = \frac{d^2\mathbf{r}(t)}{dt^2} = \frac{\mathbf{F}(t)}{m}, \quad (2.1)$$

where \mathbf{F} is the force affecting on the object, which has mass of m , velocity \mathbf{v} and coordinate \mathbf{r} at the time of t . If the time is advanced or disadvanced by a short time-step, Δt , the coordinate $\mathbf{r}(t \pm \Delta t)$ can be approximated to

$$\begin{aligned} \mathbf{r}(t \pm \Delta t) &\simeq \mathbf{r}(t) \pm \frac{d\mathbf{r}(t)}{dt}\Delta t + \frac{1}{2} \frac{d^2\mathbf{r}(t)}{dt^2}\Delta t^2 \\ &= \mathbf{r}(t) \pm \mathbf{v}(t)\Delta t + \frac{1}{2} \frac{\mathbf{F}(t)}{m}\Delta t^2, \end{aligned} \quad (2.2)$$

using Taylor’s expansion theory. The summation of $\mathbf{r}(t + \Delta t)$ and $\mathbf{r}(t - \Delta t)$ in eqn. (2.2) leads to the formula to calculate the coordinate, \mathbf{r} , at $t + \Delta t$

from the one at $t - \Delta t$ and t ,

$$\mathbf{r}(t + \Delta t) = -\mathbf{r}(t - \Delta t) + 2\mathbf{r}(t) + \frac{\mathbf{F}(t)}{m}\Delta t^2. \quad (2.3)$$

This method is termed as Verlet's algorithm³¹⁾. In the Verlet's algorithm, $\mathbf{v}(t)$ can be derived from the difference of $\mathbf{r}(t + \Delta t)$ from $\mathbf{r}(t - \Delta t)$,

$$\mathbf{v}(t) = \frac{\mathbf{r}(t + \Delta t) - \mathbf{r}(t - \Delta t)}{2\Delta t}. \quad (2.4)$$

The leap-frog method^{37, 38)} is another representation of Verlet's algorithm, with which $\mathbf{r}(t)$ and $\mathbf{v}(t + \frac{\Delta t}{2})$ lead to $\mathbf{r}(t + \Delta t)$,

$$\begin{cases} \mathbf{v}(t + \frac{\Delta t}{2}) = \mathbf{v}(t - \frac{\Delta t}{2}) + \frac{\mathbf{F}(t)}{m}\Delta t \\ \mathbf{r}(t + \Delta t) = \mathbf{r}(t) + \mathbf{v}(t + \frac{\Delta t}{2})\Delta t \end{cases}. \quad (2.5)$$

In the leap-frog method, both the coordinate and the velocity can be stored and their time evolution can be calculated. For each time step, the velocities for current time t may be calculated by formula:

$$\mathbf{v}(t) = \frac{\mathbf{v}(t - \frac{\Delta t}{2}) + \mathbf{v}(t + \frac{\Delta t}{2})}{2} = \mathbf{v}(t - \frac{\Delta t}{2}) + \frac{1}{2} \frac{\mathbf{F}(t)}{m}\Delta t, \quad (2.6)$$

and the total energy $H = K + \Phi$ (where K :kinetic energy, Φ :potential energy) can be calculated at the same time t as for potential energy. This is necessary because for an isolated system the total energy should be conserved. Therefore, this is the main test for any MD program to be run correctly.

The leap-frog method is useful when the velocity is required at the same instant for reasons of kinetic energy calculation, applying friction force for Langevin dynamics (shown in section 2.3.2), etc. The *MDsim* code applies the leap-frog method to time integration algorithm.

2.2 Interatomic Forces

2.2.1 Potential Models

Usually, the interactions between atoms are described in the form of potential energy depending on the interatomic distance. The force on particle i

can be given by the derivative of the potential function,

$$\mathbf{F}_i = -\frac{\partial}{\partial \mathbf{r}_i} \phi_{\text{tot}}(\mathbf{r}_1, \mathbf{r}_2, \dots). \quad (2.7)$$

In this formula, the total potential energy of ϕ_{tot} can be expanded according to the number of atoms to construct the potential model as following,

$$\phi_{\text{tot}}(\mathbf{r}_1, \mathbf{r}_2, \dots) = \sum_i \phi_1(\mathbf{r}_i) + \sum_{i < j} \phi_2(\mathbf{r}_i, \mathbf{r}_j) + \sum_{i < j < k} \phi_3(\mathbf{r}_i, \mathbf{r}_j, \mathbf{r}_k) + \dots, \quad (2.8)$$

where the $\sum_{i < j}$ notation indicates a summation over all distinct pairs i and j without counting any pair twice. The first term in eqn. (2.8), $\phi_1(\mathbf{r}_i)$, represents the effect of an external field on the system. The remaining terms represent interactions between particles. The ϕ_2 and ϕ_3 are termed as two-body and three-body potential, respectively. Large number of potential models have been proposed in order to represent the properties of various atoms. The interatomic potentials applied used in this study are described as follows.

ZBL model

In usual atomic collisional process with the energy ranging from several eV to several tens keV, the interaction between atoms can be described as 2-body potential model taking into account the screening effect. The ‘screening effect’ is that the Coulomb interaction between nuclei of atoms in the collisional process is compensated by the charge due to the electrons surrounding the nuclei, so that the screened Coulomb potential can be formulated as;

$$\phi(r) = \frac{Z_1 Z_2 e^2}{4\pi\epsilon r} \Phi(r), \quad (2.9)$$

where Z_1 and Z_2 are the atomic number of two atoms and r is the interatomic distance. Various types of the screening function, $\Phi(r)$, have been proposed. In the *MDsim* code, the screening function developed by Ziegler, Biersack and Littmark²⁷⁾ is applied to the interactions concerned with rare gas atoms such as Ar and Ne. In the ZBL model, the screening function, $\Phi_{\text{ZBL}}(r)$, is given as the function of the interatomic distance r and scaling

parameter a ;

$$\Phi_{\text{ZBL}}(r) = \sum_{i=1}^4 c_i \exp\left(-d_i \frac{r}{a}\right), \quad \sum_{i=1}^4 c_i = \Phi(0) = 1, \quad (2.10)$$

and

$$a = \left(\frac{9\pi^2}{128}\right)^{1/3} \frac{a_{\text{B}}}{Z_{12}^{1/3}}, \quad Z_{12} = (Z_1^{0.23} + Z_2^{0.23})^3, \quad (2.11)$$

where a_{B} is the first Bohr radius. The screening parameters, (c_i, d_i) , in eqn. (2.10) are given by²⁷⁾,

$$\begin{aligned} (c_i, d_i) = & (0.028171, 0.20162), \\ & (0.28022, 0.40290), \\ & (0.50986, 0.94229), \\ & (0.18175, 3.1998). \end{aligned} \quad (2.12)$$

The ZBL potential model monotonically decreases with increasing inter-atomic distance, but does not expire at long distance. In order to reduce the calculation time in MD simulation, it is required to introduce a cut-off radius as mentioned in the following section. Thus, the ZBL potential model are modified to reduce to 0 at cut-off length (r_c) using a spline function of 3rd order,

$$\phi_{\text{ZBL}}(r) = \phi_{\text{ZBL}}(r)S(r) \quad (2.13)$$

$$S(r) = \begin{cases} 1 & (r < a) \\ \frac{(2r - 3a + b)(r - b)^2}{(b - a)^3} & (a < r < b) \\ 0 & (b < r) \end{cases} \quad (2.14)$$

In this study, the a and b in eqn. (2.14) are set at $0.8r_c$ and r_c , respectively, and r_c usually is the bond length of molecule. The interactions concerned with rare-gas atoms, such as Ar and Ne, are described with only repulsive potential of the ZBL model. This is because, for example, the binding energy of Ar–Ar and Ar–Si are considered to be less than 0.1eV, and this energy is much less than the incident energy of ions, which is in the range from several-eV to several-keV, and the binding energy between Si atoms, which is about 2eV.

Table 2.1: Parameters of Stillinger-Weber potential for silicon³⁹⁾.

ϵ (eV)	2.1673	σ (Å)	2.0951
a	1.8		
A	7.049556277	B	0.6022245584
p	4	q	0
λ	21.0	γ	1.20

Stillinger-Weber model

The multi-body terms, ϕ_3 and other terms with relating to more atoms described in eqn. (2.8), represent the effect of the coordination of atomic bond, which becomes more significant when the dynamics of solids and the structure of the molecule are considered. Stillinger and Weber³⁹⁾ developed a potential model to describe the structure and properties of silicon at both solid and liquid phase. The Stillinger-Weber (SW) potential is formulated as;

$$\phi_2(\mathbf{r}_i, \mathbf{r}_j) = \begin{cases} \epsilon A \left(B \left(\frac{r_{ij}}{\sigma} \right)^{-p} - \left(\frac{r_{ij}}{\sigma} \right)^{-q} \right) \times \exp \left[\left(\frac{r_{ij}}{\sigma} - a \right)^{-1} \right] & \text{(if } r_{ij}/\sigma < a \text{)} \\ 0 & \text{(if } r_{ij}/\sigma \geq a \text{)} \end{cases}, \quad (2.15)$$

$$\begin{aligned} \phi_3(\mathbf{r}_i, \mathbf{r}_j, \mathbf{r}_k) = & h(r_{ij}, r_{ik}, \theta_{jik}) + h(r_{jk}, r_{ji}, \theta_{kji}) \\ & + h(r_{ki}, r_{kj}, \theta_{ikj}), \end{aligned} \quad (2.16)$$

$$\begin{aligned} h(r_1, r_2, \theta) = & \epsilon \lambda \exp \left[\gamma \left(\left(\frac{r_1}{\sigma} - a \right)^{-1} + \left(\frac{r_2}{\sigma} - a \right)^{-1} \right) \right] \\ & \times \left(\cos \theta + \frac{1}{3} \right)^2, \end{aligned} \quad (2.17)$$

where r_{ij} , for example, is the distance between atom i and j , and θ_{jik} is the angle around atom i formed by i - j and i - k bonds. The parameters of this potential model for Si atom are shown in table 2.1. As shown in eqn. (2.17), the element of three-body potential, $h(r_1, r_2, \theta)$, gives the minimum value of 0 at $\cos \theta = -1/3$, which means that the three-body term induces the silicon atoms to form the tetrahedral structure, whereas the two-body term gives the bond length and the binding energy of silicon.

The interatomic potentials between F–F and Si–F were also developed

by Stillinger et al.^{40, 41, 42)} and modified by Weakliem et al.⁴³⁾ in a similar manner to that of Si atoms. The 2-body terms for F–F and Si–F are given by;

$$\phi_{2,\text{FF}}(r) = \epsilon_{\text{FF}} A_{\text{FF}} (r^{-8} - r^{-4}) \exp \left[\left(\frac{r}{\sigma_{\text{FF}}} - a_{\text{FF}} \right)^{-1} \right], \quad (2.18)$$

$$\phi_{2,\text{SiF}}(r) = \epsilon_{\text{SiF}} A_{\text{FF}} (B_{\text{SiF}} r^{-3} - r^{-2}) \exp \left[\gamma_{\text{SiF}} \left(\frac{r}{\sigma_{\text{SiF}}} - a_{\text{SiF}} \right)^{-1} \right], \quad (2.19)$$

and 3-body elements depending on the atomic species are given by;

$$\begin{aligned} h_{\text{FFF}} = & \epsilon_{\text{FF}} A_{\text{FFF}} (r_1 r_2)^{-4} \exp \left[\left(\frac{r_1}{\sigma_{\text{FF}}} - a_{\text{FF}} \right)^{-1} + \left(\frac{r_2}{\sigma_{\text{FF}}} - a_{\text{FF}} \right)^{-1} \right] \\ & + (50 - 25 \cos^2 \theta) \\ & \times \exp \left\{ \gamma_{\text{FFF}} \left[\left(\frac{r_1}{\sigma_{\text{FF}}} - b_{\text{FF}} \right)^{-1} + \left(\frac{r_2}{\sigma_{\text{FF}}} - b_{\text{FF}} \right)^{-1} \right] \right\}, \end{aligned} \quad (2.20)$$

$$\begin{aligned} h_{\text{SiSiF}} = & \epsilon_{\text{SiF}} A_{\text{SiSiF}} \left[\left(\cos \theta + \frac{1}{3} \right)^2 - c_{\text{SiSiF}} \right] \\ & \times \exp \left\{ \gamma_{\text{SiSiF}} \left[\left(\frac{r_1}{\sigma_{\text{SiF}}} - a_{\text{SiF}} \right)^{-1} + \left(\frac{r_2}{\sigma_{\text{SiF}}} - a_{\text{SiF}} \right)^{-1} \right] \right\}, \end{aligned} \quad (2.21)$$

$$h_{\text{SiFSi}} = \epsilon_{\text{SiF}} A_{\text{SiFSi}} \exp \left\{ \gamma_{\text{SiFSi}} \left[\left(\frac{r_1}{\sigma_{\text{SiF}}} - a_{\text{SiF}} \right)^{-1} + \left(\frac{r_2}{\sigma_{\text{SiF}}} - a_{\text{SiF}} \right)^{-1} \right] \right\}, \quad (2.22)$$

$$h_{\text{SiFF}} = \epsilon_{\text{SiF}} A_{\text{SiFF}} \exp \left\{ \gamma_{\text{SiFF}} \left[\left(\frac{r_1}{\sigma_{\text{SiF}}} - a_{\text{SiF}} \right)^{-1} + \left(\frac{r_2}{\sigma_{\text{SiF}}} - a_{\text{SiF}} \right)^{-1} \right] \right\}, \quad (2.23)$$

$$\begin{aligned} h_{\text{FSiF}} = & \epsilon_{\text{SiF}} \left[A_{\text{FSiF}} (\cos \theta - \cos 103^\circ)^2 - c_{\text{FSiF}} \right] \\ & \times \exp \left\{ \gamma_{\text{SiSiF}} \left[\left(\frac{r_1}{\sigma_{\text{SiF}}} - a_{\text{SiF}} \right)^{-1} + \left(\frac{r_2}{\sigma_{\text{SiF}}} - a_{\text{SiF}} \right)^{-1} \right] \right\}. \end{aligned} \quad (2.24)$$

The SW potential parameters for F-F and Si-F are given in table 2.2.

Tersoff model

As for the interaction between carbon atoms, Tersoff's empirical model potential⁴⁴⁾ is applied. The Tersoff's model is formulated as follows;

$$E = \sum_i E_i = \frac{1}{2} \sum_{i \neq j} V_{ij}, \quad V_{ij} = f_{\text{C}}(r_{ij}) [f_{\text{R}}(r_{ij}) - b_{ij} f_{\text{A}}(r_{ij})], \quad (2.25)$$

where $f_{\text{C}}(r_{ij})$ is a cut-off function that restricts interactions to nearest neighbors, $f_{\text{R}}(r_{ij})$ and $f_{\text{A}}(r_{ij})$ are Morse-like pair functions of the interatomic separation, r_{ij} , and b_{ij} is a many-body function that can be regarded

Table 2.2: Parameters of Stillinger-Weber potential for fluorine–fluorine and silicon–fluorine^{40, 41, 42, 43}).

ϵ_{FF} (eV)	1.66	σ_{FF} (Å)	1.2141
a_{FF}	3.6	b_{FF}	2.8
A_{FF}	6.052463017	A_{FFF}	8.4
γ_{FFF}	3		
ϵ_{SiF} (eV)	2.1673	σ_{SiF} (Å)	2.0951
a_{SiF}	1.8	γ_{SiF}	1.339450
A_{SiF}	21.199221	B_{SiF}	0.546418
A_{SiSiF}	3.624533	c_{SiSiF}	0.218615
γ_{SiSiF}	0.463088	A_{SiFSi}	50.874092
γ_{SiFSi}	1.371580	A_{SiFF}	2.792073
γ_{SiFF}	1.0	A_{FSiF}	22.406434
c_{FSiF}	2.068601	γ_{FSiF}	0.890132

as an effective Pauling bond order;

$$f_{\text{R}}(r_{ij}) = A \exp(-\lambda r_{ij}), \quad (2.26)$$

$$f_{\text{A}}(r_{ij}) = B \exp(-\mu r_{ij}), \quad (2.27)$$

$$f_{\text{C}}(r_{ij}) = \begin{cases} 1 & (r_{ij} < R) \\ \frac{1}{2} + \frac{1}{2} \cos \frac{\pi(r_{ij} - R)}{S - R} & (R < r_{ij} < S) \\ 0 & (r_{ij} > S) \end{cases}, \quad (2.28)$$

$$b_{ij} = (1 + \beta^n \zeta_{ij}^n)^{-\frac{1}{2n}}, \quad (2.29)$$

$$\zeta_{ij} = \sum_{k \neq i, j} f_{\text{C}}(r_{ik}) g(\theta_{jik}), \text{ and} \quad (2.30)$$

$$g(\theta_{jik}) = 1 + \frac{c^2}{d^2} - \frac{c^2}{d^2 + (h - \cos \theta_{jik})^2} \quad (2.31)$$

where θ_{jik} is a bond angle. This potential is suitable to describe equilibrium properties in various phases of carbon, such as graphite and diamond, but is not suitable at the high-energy collisional condition because the 2-body repulsive term, $f_{\text{R}}(r_{ij})$ in eqn. (2.26), gives finite value at $r_{ij} = 0$. In order to simulate collisions of high-energy ions, $f_{\text{R}}(r_{ij})$ is replaced by the ZBL model given by eqn. (2.9), when the r_{ij} is less than 0.4069\AA . The difference in potential energy between the two models at this distance is 136.97eV .

Table 2.3: Parameters of Tersoff potential model for carbon ⁴⁴⁾.

$A(\text{eV})$	1.3936×10^3	$B(\text{eV})$	3.467×10^2
$\lambda(\text{\AA}^{-1})$	3.4876	$\mu(\text{\AA}^{-1})$	2.2119
β	1.5724×10^{-7}	n	7.2751×10^{-1}
c	3.8049×10^4	d	4.384×10^0
h	-5.7058×10^{-1}		
$R(\text{\AA})$	1.8	$S(\text{\AA})$	2.1

This energy is subtracted from the ZBL potential at $r_{ij} < 0.4069\text{\AA}$ to connect these two potential curves and their derivatives smoothly. Thus, the repulsive part of Tersoff's model is replaced by

$$f_R'(r_{ij}) = \begin{cases} \phi_{\text{ZBL}}(r_{ij}) - 136.97\text{eV} & (r_{ij} < 0.4069\text{\AA}) \\ f_R(r_{ij}) & (r_{ij} \geq 0.4069\text{\AA}) \end{cases} . \quad (2.32)$$

The parameters for eqn. (2.26)-(2.31), and the modified potential curve given by eqn. (2.32) are shown in table 2.3 and figure 2.1, respectively.

2.2.2 Cut-off Radius

As the number of atoms to deal with for potential calculation becomes larger, longer simulation time is required. For the calculation of m -body potential in the system with N atoms, the number of pairs taken into consideration counts up to the order of N^m . In order to reduce the calculation time, the usual potential functions, except the long range force such as Coulomb force, are designed to have the cut-off radius — the maximum atomic distance in which a surrounding atom affects on the central atom. In the case of SW potential model in eqn. (2.15)–(2.17), for example, the cut-off radius can be set at σa . By introducing the cut-off radius, the number of atoms for potential calculation considered as constant, is a few or several tens atoms, so that the calculation times can be reduced from the order of N^m to N .

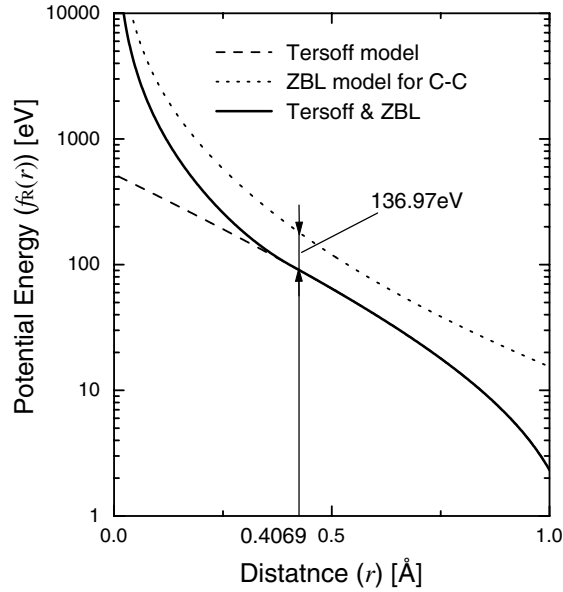


Figure 2.1: Modified potential curve of the repulsive part in Tersoff potential model for high-energy atomic collision.

2.3 Boundary Conditions

2.3.1 Periodic Boundary Conditions

The problem of surface effects can be overcome by implementing periodic boundary conditions (PBC). A schematic of 2-dimensional PBC is shown in figure 2.2. The central box is replicated throughout the space to form an infinite lattice. If an atom moves in the original box (framed with thick line), its periodic image in each of the neighboring boxes moves in exactly the same way. Thus, if an atom leaves the central box, such as the atom ‘a’ in figure 2.2, one of its images will enter through the opposite face, which is shown as ‘a’

In a course of simulation, the relative distance between two atoms might be modified according to the original position of them. Figure 2.3 shows the schematic of 1-dimensional PBC. The original periodic cell with the periodic length $L(=L_1, L_2)$ and the two atoms, ‘O’ and ‘a’, are drawn with thick line. In figure 2.3, the atom ‘a’ can be considered to be out of the

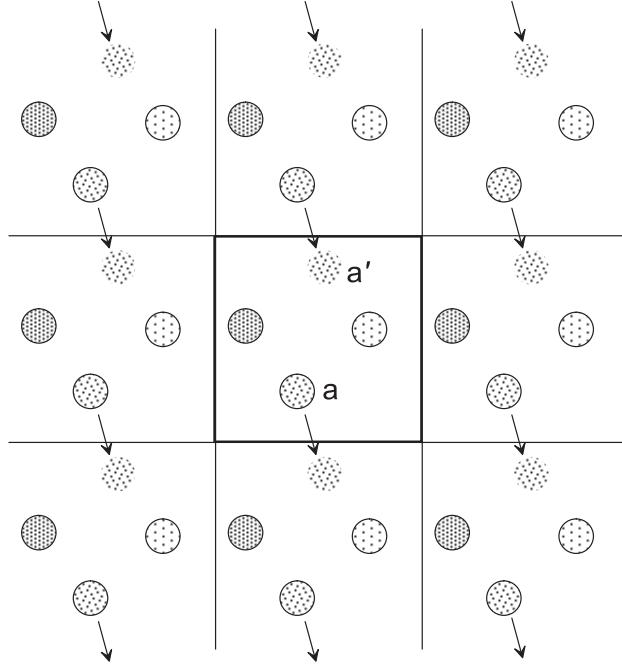


Figure 2.2: Schematic of 2-dimensional periodic boundary condition.

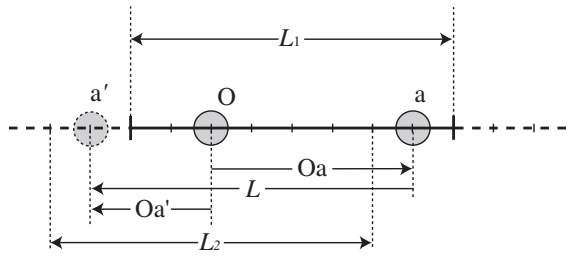


Figure 2.3: Schematic of mapping method under 1-dimensional periodic boundary condition. If $\overline{Oa} > L/2$, the atom a is wrapped to a' and the distance $\overline{Oa'}$ is calculated as $\overline{Oa} - L$.

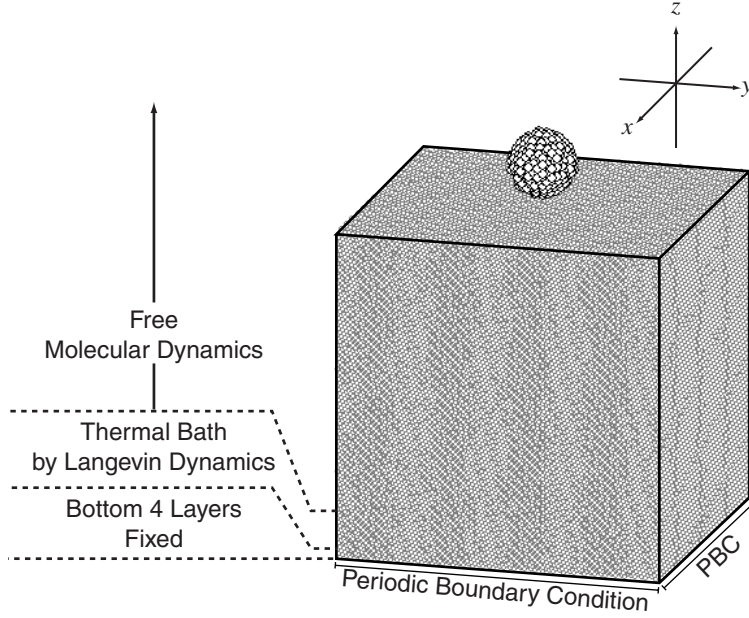


Figure 2.4: Boundary conditions of MD simulation in this study.

periodic cell from the view point of the atom ‘O’, which is indicated as L_2 , so that the interatomic distance between ‘O’ and ‘a’ should be considered as one between ‘O’ and the periodic image ‘a’’. Thus, the relative distance \overline{Oa} is given by,

$$\overline{Oa} = \begin{cases} \overline{Oa'} = \overline{Oa} - L & (\overline{Oa} > L/2) \\ \overline{Oa'} = \overline{Oa} + L & (\overline{Oa} < -L/2) \\ \overline{Oa} & (\text{else}) \end{cases} . \quad (2.33)$$

This formula can be applied to the calculation under 2- or 3-dimensional PBC. The PBC cannot be applied if the interatomic force is governed by long range potential. In order to simplify the implementation of PBC, the periodic length L should be longer than double the cut-off radius mentioned in section 2.2.2, otherwise the force calculation should take into consideration the contributions of both original and duplicated atoms.

2.3.2 Temperature Control

Figure 2.4 shows the boundary conditions of the system used in this study. The 2-dimensional periodic boundary condition is applied in the two horizontal x and y directions. The boundary in the upper z -direction is free and the atoms in bottom 4 mono-layers are fixed keeping the bulk structure. The several mono-layer atoms on fixed layers act as thermal bath. This thermal bath releases the excess kinetic energy out of the system because the solid target is irradiated with monomer and cluster ions with up to several tens keV.

The motion of atoms in the thermal bath is governed by Langevin Dynamics^{45, 46}. The classical Langevin dynamics for 1-dimensional system is described as the stochastic differential equation about velocity v ,

$$\dot{v}(t) = -\gamma v(t) + \mathcal{A}(t), \quad (2.34)$$

where γ and \mathcal{A} are the friction coefficient and the acceleration by a random force, respectively. If $\mathcal{A}(t)$ represents a Gaussian random process, it should satisfy the following condition about the average, $\langle \mathcal{A}(t) \rangle$, and the autocorrelation function, $\langle \mathcal{A}(t)\mathcal{A}(t + \tau) \rangle$;

$$\langle \mathcal{A}(t) \rangle = 0 \quad (2.35)$$

$$\langle \mathcal{A}(t)\mathcal{A}(t + \tau) \rangle = 2\tilde{D}\delta(\tau), \quad (2.36)$$

where $\delta(\tau)$ is a delta function and $2\tilde{D}$ gives the variance of \mathcal{A} . The Fourier transformation of eqn. (2.34) can be given by

$$\tilde{v}_T(\omega) = \frac{\tilde{\mathcal{A}}_T(\omega)}{i\omega + \gamma}. \quad (2.37)$$

In eqn. (2.37), $\tilde{v}_T(\omega)$ and $\tilde{\mathcal{A}}_T(\omega)$ are Fourier-transformed expressions of v and \mathcal{A} clipped by window function, respectively:

$$\begin{aligned} \tilde{X}_T(\omega) &= \int_{-\infty}^{\infty} \Pi_T(t) X(t) \exp(-i\omega t) dt \\ \Pi_T(t) &= \begin{cases} 1 & (-T/2 < t < T/2) \\ 0 & (\text{else}) \end{cases} \\ &\quad (X \equiv \mathcal{A}, v). \end{aligned} \quad (2.38)$$

Eqns. (2.36) and (2.38) lead to the spectral density of $\tilde{\mathcal{A}}_T(\omega)$ and $\tilde{v}_T(\omega)$,

$$\begin{aligned}
 S_{\mathcal{A}}(\omega) &= \lim_{T \rightarrow \infty} \frac{1}{\pi T} |\tilde{\mathcal{A}}_T(\omega)|^2 \\
 &= \frac{1}{\pi} \int_{-\infty}^{\infty} \langle \mathcal{A}(t) \mathcal{A}(t + \tau) \rangle \exp(-i\omega\tau) d\tau \\
 &= \frac{1}{\pi} \int_{-\infty}^{\infty} 2\tilde{D}\delta(\tau) \exp(-i\omega\tau) d\tau \\
 &= \frac{2\tilde{D}}{\pi},
 \end{aligned} \tag{2.39}$$

and

$$\begin{aligned}
 S_v(\omega) &= \lim_{T \rightarrow \infty} \frac{1}{\pi T} |\tilde{v}_T(\omega)|^2 \\
 &= \frac{1}{\pi} \int_{-\infty}^{\infty} \langle v(t) v(t + \tau) \rangle \exp(-i\omega\tau) d\tau \\
 &= \frac{1}{\omega^2 + \gamma^2} S_{\mathcal{A}}(\omega) \\
 &= \frac{2\tilde{D}}{\pi(\omega^2 + \gamma^2)}.
 \end{aligned} \tag{2.40}$$

The simple equation of autocorrelation function of v can be given by second and forth formula in eqn. (2.40),

$$\langle v(t) v(t + \tau) \rangle = \frac{1}{2} \int_{-\infty}^{\infty} S_v(\omega) \exp(i\omega\tau) d\omega = \frac{\tilde{D}}{\gamma} \exp(-\gamma\tau). \tag{2.41}$$

If τ converges to 0, the left term in eqn. (2.41) gives the variance of velocity, which is $k_b T/m$ if v allows Boltzmann distribution (k_b : Boltzmann constant, T : temperature, m : mass of object). Thus, eqn. (2.41) leads to the relationship between \tilde{D} and γ ,

$$\tilde{D} = \frac{k_b T \gamma}{m}. \tag{2.42}$$

Consequently, the probability of a random acceleration \mathcal{A} is given as the Gaussian distribution;

$$P(\mathcal{A}) = \frac{1}{\sqrt{2\pi 2\tilde{D}}} \exp\left(-\frac{\mathcal{A}^2}{2(2\tilde{D})}\right). \tag{2.43}$$

In the *MDsim* code, the $P(\mathcal{A})$ is approximated to uniform distribution

$$P(\mathcal{A}) \simeq P'(\mathcal{A}) = \begin{cases} \frac{1}{6\sqrt{2\tilde{D}}} & (-3\sqrt{2\tilde{D}} < \mathcal{A} < 3\sqrt{2\tilde{D}}) \\ 0 & (\text{else}) \end{cases}. \quad (2.44)$$

Thus, the acceleration by random force \mathcal{A} can be generated by following formula,

$$\mathcal{A} = 3\sqrt{2\tilde{D}}(1 - 2R[0, 1]) = 3\sqrt{\frac{2k_b T \gamma}{m}}(1 - 2R[0, 1]), \quad (2.45)$$

where $R[0, 1]$ is random value uniformly distributed on 0 to 1.

2.4 Acceleration Methods for MD Calculations

2.4.1 Book-keeping Method

It is a significant subject to accelerate the calculation speed of MD simulation. If the potential model is described with the cut-off length (r_c) explained in section 2.2.2, the book-keeping method, which is one of the most conventional and efficient methods to accelerate the calculation speed, can be applied. In the book-keeping method, each atom has the list of neighboring atoms which reside within the cut-off sphere. This ‘book-keeping’ list can be updated after a certain number of time-steps. In this method, updating the list takes a time of $O(N^2)$, however, the time for usual potential calculation can be reduced to $O(N)$.

The cut-off radius for the book-keeping list, r_{list} , should be long enough for another atom not to come into the r_{list} sphere until the next update time. Thus, the minimum r_{list} is given by

$$r_{\text{list}} \geq r_c + u \cdot v_{\text{max}} \Delta t, \quad (2.46)$$

where u and v_{max} are frequency of list-update and maximum velocity in the system, respectively.

2.4.2 Linked Cell Method

Another conventional method for acceleration is the so-called ‘linked cell’ method. In this method, the space is divided into cubic cells, as shown in

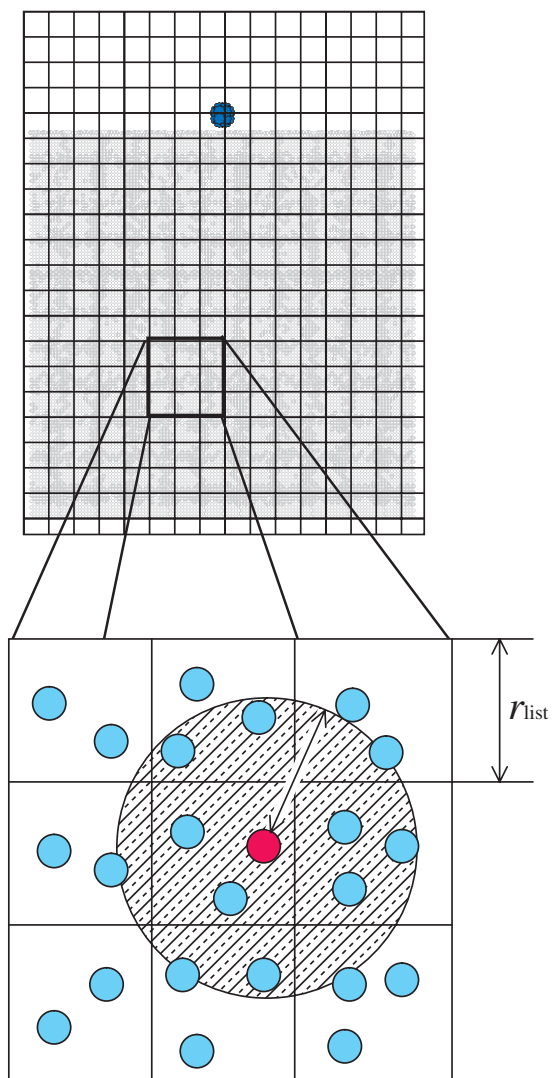


Figure 2.5: Schematic of linked cell method.

figure 2.5. The length of the cell is set at larger than r_{list} . Every atom in the system is distributed in one of these cells at similar frequency with the book-keeping method. In the course of simulation, the neighboring atoms within the r_c sphere will be found from the cell where the atom of interest itself belongs, and the cells surrounding. In the linked-cell method, the number of atoms to be considered during the force calculation is several times larger than that of the book-keeping method. However, every procedure in the program, such as distributing the atoms and searching neighboring atoms will be finished within the $O(N)$ order, and less memory resources are required than in the book-keeping method. If enough memory resources are available, it would be a more efficient method to use both the book-keeping and the linked-cell methods; atoms are distributed in cells first, and then book-keeping lists are made in the manner of linked-cell method.

2.4.3 Different Time-step Method

The displaced length, Δr_i , with which the atom i moves during time-step, Δt , is given by $v_i(t + \Delta t/2)\Delta t$. This indicates that the time-step should be set short enough to keep the precision, which usually depends on v_i . As for the usual MD simulation of high-energy ion impacts on a solid surface, the time-step should be decided depending on the velocity of the incident atom, which is extremely high compared with that of target atoms, i.e. the target atoms in the majority are simulated on excessive precision.

The different time-step method is the way to apply independent time-step to each atom according to its velocity and accelerate the calculation speed of high-energy atomic collisional process. If the maximum displacements per 1 time-step, Δr , is given, the ‘short’ time-step can be given by

$$\Delta t_{\text{short}} = \frac{\Delta r}{v_i}, \quad (2.47)$$

where the v_i is the maximum velocity in the system, which usually corresponds to the velocity of an incident atom. On the other hand, the MD calculation for almost all of atoms in the system can be done with a longer time-step than Δt_{short} ,

$$\Delta t_{\text{long}} = \frac{\Delta r}{v_s}, \quad (2.48)$$

where v_s is considered as the maximum velocity only among the substrate atoms. Thus, the maximum acceleration ratio by the different time-step method, s , can be estimated as

$$s = \frac{\Delta t_{\text{long}}}{\Delta t_{\text{short}}} = \frac{v_i}{v_s}. \quad (2.49)$$

Figure 2.6 shows the flowchart of different time-step methods applied to the *MDsim* code. First, all atoms in the system are categorized in four types after they are distributed to linked cells:

- Atom-1, having high velocity and requiring short time-step of Δt .
- Atom-2, having low velocity and interacting with atom-1 directly.
- Atom-3, having low velocity and interacting with atom-2.
- Atom-4, other low velocity atoms.

The threshold value to distinguish between high and low velocity is given by v_s in eqn. (2.48). The velocity and position of atom-1 and -2 are updated every short time-step, Δt , so that the interactions concerned with atom-1 and -2, f_{12} and f_{23} , should be calculated every Δt . On the other hand, slow atoms, atom-3 and -4, are updated every $s\Delta t$, where s is defined in eqn. (2.49), so that the interaction between atom-3 and -4, f_{34} is calculated only once in this routine. It should be noted that the interaction between atom-2 and -3 should be calculated every Δt , but atom-3 does not move during the short time-step calculation. The force on atom-3 concerned with atom-2 is averaged by accumulating the force divided by s , i.e. the force on atom-3 is given by

$$F_3(0 \sim (s-1)\Delta t) = f_{34}(0) + \sum_{l=0}^{s-1} \frac{f_{23}(l\Delta t)}{s}. \quad (2.50)$$

Figure 2.7 shows the relationship between the estimated and achieved acceleration ratio by the different time-step method in the *MDsim* code. In this test, the Si(001) substrate which consists of 262144 Si atoms is prepared and simulated at the temperature of 300K with v_i and v_s varied, but with Δr fixed. In figure 2.7, each velocity is described in a reduced unit, vu , which is given by $\sqrt{\epsilon/m}$ (where m is mass of Si atom and ϵ is in

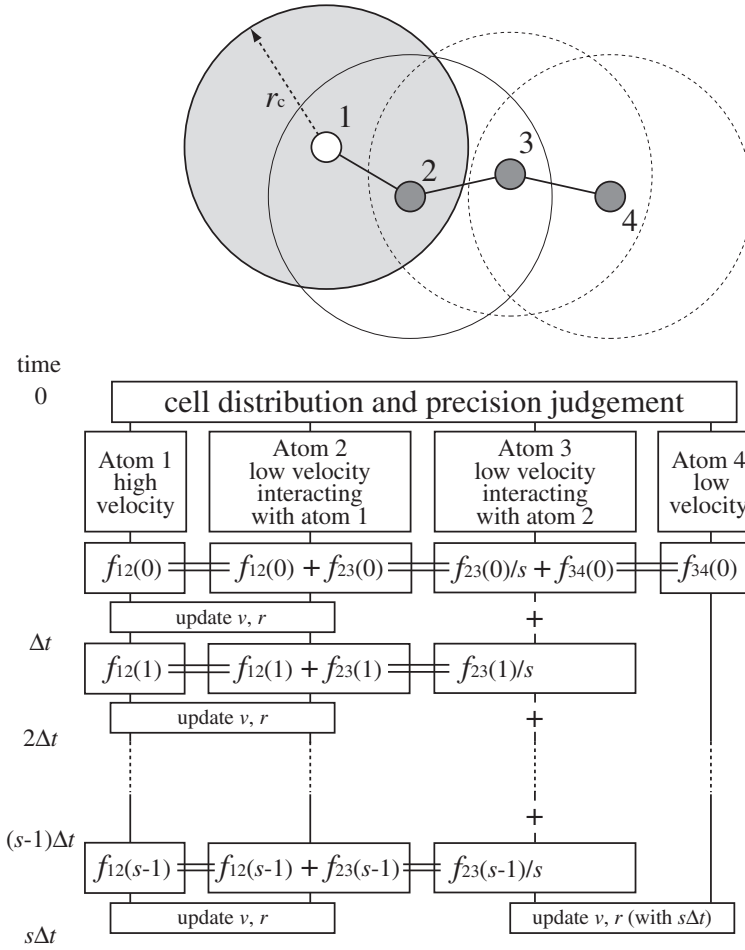


Figure 2.6: Flowchart of the ‘different time-step’ method. The atom-1 has high velocity and requires a short time-step. v and r of atom-1 and -2 are updated every Δt and those of -3 and -4, every $s\Delta t$.

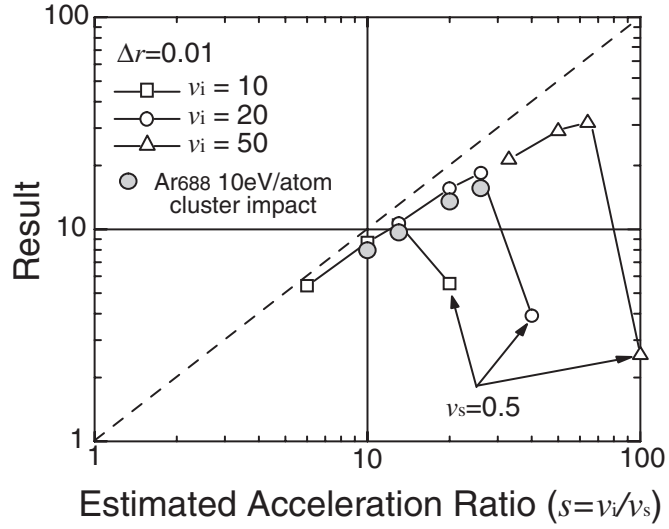


Figure 2.7: Relationship between the estimated and achieved acceleration ratio by different time-step method, for the simulations of Si(001) substrate, and Ar₆₈₈ cluster impacting on the Si(001) substrate.

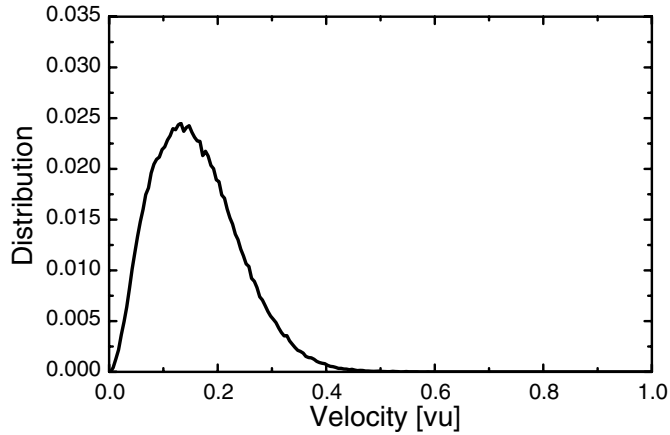


Figure 2.8: Velocity distribution of Si substrate atoms at 300K. Velocity is scaled with reduced unit, which is given in $\sqrt{\epsilon/m}$ (where m is mass of Si atom and ϵ is given in table 2.1).

table 2.1). As can be seen in figure 2.7, the calculation speed is improved by as much as the estimated ratio, except at $v_s=0.5vu$. This is because some Si atoms are considered as fast atoms at $v_s=0.5vu$, as shown in figure 2.8 — the velocity distribution of Si atoms at 300K. The difference in s value between estimation and result increases with increasing s , because a longer r_{list} is required with increasing v_i and the number of atoms taken into consideration at each force calculation also increases proportionally to r_{list}^3 , as shown in eqn. (2.46). Figure 2.7 also shows the results at the impact of Ar₆₈₈ cluster with the incident energy of 10eV/atom on Si(001) target. The calculation speed is also accelerated, which means that, for such a large system, almost all of the calculation time is consumed by the calculation of static target atoms.

Chapter 3

Impact Processes of Cluster Ions

3.1 Introduction

When a cluster ion impacts on a solid surface, high-density atomic collisions occur between the cluster and substrate atoms. This multiple collision mechanism cause phenomena different from those of monomer ions. For example, it has been found by STM observation of a surface irradiated by cluster ions, that cluster impact forms a large crater-like damage on the surface, which is not shown with monomer ion irradiation^{47, 48, 49}. In this chapter, MD simulations of Ar monomer and Ar cluster, with size ranging from several to thousands atoms, impacting on the Si(001) surface will were performed. The penetration, damage formation and sputtering process are examined and the nonlinear collisional processes of cluster ions are discussed.

3.2 Simulation Model

The Stillinger-Weber (SW) potential model³⁹ is employed as the inter-atomic potential between Si atoms. The formula of SW potential model and its parameters are given by eqn. (2.15)–(2.17) and table 2.1. The SW model well represents the properties of solid and liquid Si under widely ranging temperature and pressure, which means it is capable to simulate the collisional process of ion impact.

As for the interactions between Ar–Ar and Ar–Si, the 2-body potential model developed by Ziegler, Biersack and Littmark²⁷ is applied, which is given by eqn. (2.9)–(2.14). The cut-off radius (r_c) for Ar–Ar under ZBL

model is set at 3.84\AA which corresponds the bond length of Ar_2 molecule. On the other hand, the r_c for Ar-Si is 3.1\AA , which is the mean bond length of Ar-Ar and Si-Si (2.35\AA).

$\text{Si}(001)$ substrate is prepared as the target material. The periodic boundary condition and thermal bath are applied as shown in figure 2.4. The dimension of the target is varied depending on the cluster size and the energy of the incident particle. The largest Si substrate consists of about 260,000 atoms, 128 mono-layers with 2048 atoms, and its dimensions are about 180\AA cubic. Before irradiation of ions, the substrate temperature is set at 300K by the simulation with the Langevin dynamics applied to the whole part of substrate except bottom-fixed layer for 8ps first, and then by the simulation of free molecular dynamics for 8ps. In this heating process, the surface Si atoms form the stable 2×1 surface structure⁵⁰⁾.

Ar cluster and monomer are irradiated on the Si surface in order to understand the nonlinear effect by cluster ion impact due to the physical atomic collision process. The total energy of the Ar cluster is varied from 0.5keV to 55keV and the number of atoms in the cluster (cluster size) is changed from 13 to about 1000. In each simulation, the Ar cluster has a spherical shape and icosahedral structure, which is supported by the experimental results reported by Farges⁵¹⁾ and Miehel⁵²⁾. These clusters impact on the surface in the normal direction. The internal temperature of the cluster is considered negligible, so that each atom in the cluster has the same velocity in both magnitude and direction at the beginning of the impact.

3.3 The Impact Processes of Monomer and Cluster Ions

3.3.1 Monomer Ion Impact

First, the MD simulation of Ar monomer impact was performed. Figure 3.1 shows snapshots of Ar monomer accelerated with 7keV impacting on a $\text{Si}(001)$ substrate. The large white, small light-gray and dark-gray circles indicate incident Ar, stable Si and displaced Si atoms, respectively. Dis-

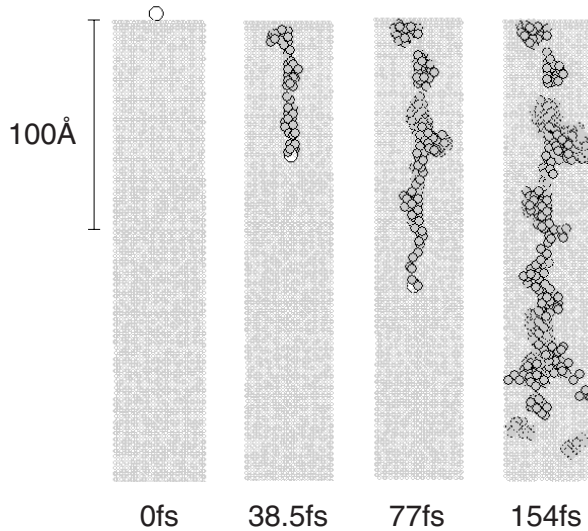


Figure 3.1: Snapshots of Ar monomer impacting on Si(001) with 7keV.

placed Si atom is defined as an atom having potential energy 0.4eV above the bulk state⁵³). The incident Ar atom penetrates the surface and displacements are formed along trajectory of incident atom. At 154fs after impact, the displacements show a branched structure due to the ‘cascade model’¹¹); some knocked-on substrate atoms obtain high energy and they generate new displacements in a similar manner to the incident atom.

3.3.2 Cluster Ion Impact

The impact process of large Ar cluster was simulated and compared with that of monomer ion. Figure 3.2 shows the snapshots of an Ar₆₈₈ cluster impacting on a Si(001) surface. Comparing with figure 3.1 and 3.2, it is shown that the impact process of cluster is very different from that of monomer ion. At this size and incident energy, almost all of incident Ar atoms are once implanted into the substrate maintaining themselves as cluster state, whereas the monomer ion with 10eV/atom cannot penetrate the surface but is only reflected on the surface. This is because that the

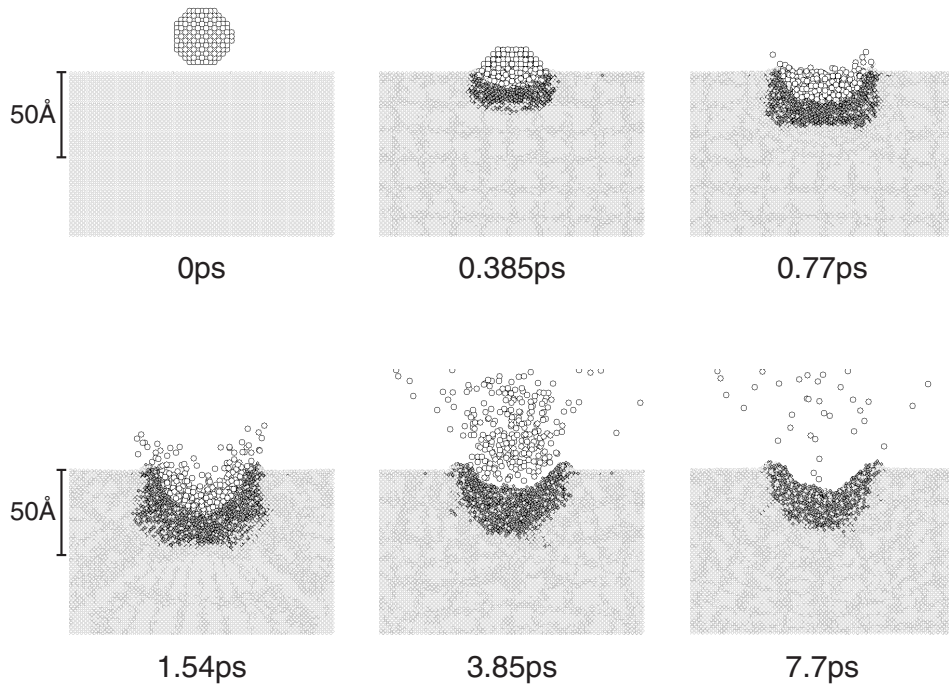


Figure 3.2: Snapshots of Ar_{688} with 10 eV/atom impacting on $\text{Si}(001)$.

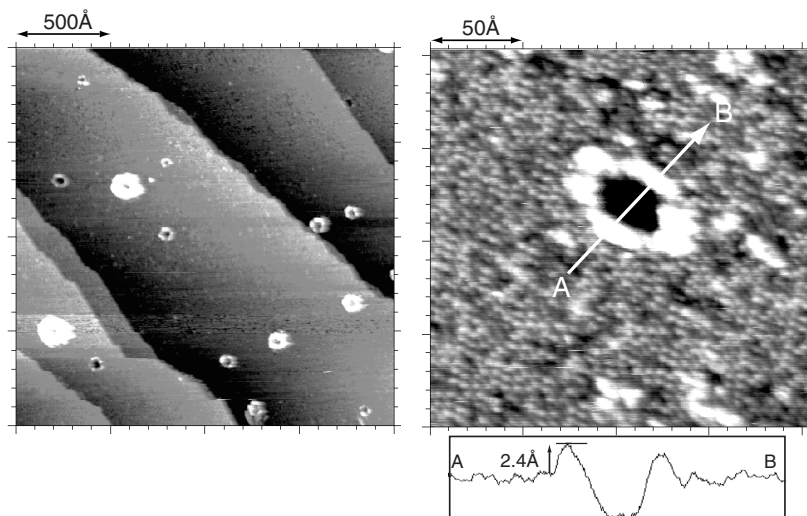


Figure 3.3: STM images of Si(111) surface irradiated with Ar cluster ions at totally 8keV, 6.3×10^{10} ions/cm².

first cluster atom at the collision with a substrate atom is given the kinetic energy from the following cluster atoms to penetrate the surface, and then, if the substrate atom is pushed aside from its original site, the next following cluster atom can impinge into the substrate without collision with a substrate atom and kinetic energy loss. This characteristic penetration effect by cluster is termed as ‘acceleration effect’ or ‘clearing-way’ effect³²⁾. In this impact process, the incident atoms are confined into a narrow region, so that the collisional point on the surface gains extremely high-pressure and high-temperature during several pico seconds. The surface atoms at the impact point are largely displaced and a homogeneous damaged region is formed surrounding the cluster. At a few ps after impact, these displacements start to recover, and then the incident cluster atoms are reflected. Consequently, almost all of the cluster atoms re-evaporate to the vacuum because of the small interatomic force between cluster, and surface atoms and a crater-like damage remains on the surface.

This crater-like damage formation is also observed experimentally. Figure 3.3 shows the STM image of a Si(111) surface irradiated with Ar cluster accelerated with a total energy of 8keV and with a dose of 6.3×10^{10}

ions/cm². The left and right images show a 200nm×200nm and a 20nm×20nm ares, respectively. Those images obtained by experiment and simulation show similar shape and size of the crater-like damage, which means that this MD simulation has been done correctly and it can be considered that the impact process of cluster ion proceeds as in the course shown in figure 3.2.

3.3.3 Multiple-collision Effect and Thermalization

Figure 3.4 shows the impact of Ar₆₈₈ clusters with the total incident energy of 1, 3, 5 and 7keV on the Si(001) substrate at 3.85ps after impact. Additionally, the time evolution of the total kinetic energy and penetration depth of the cluster in each case is shown in figure 3.5. In figure 3.5, the penetration depth of the cluster is defined as the position of the center-of-mass of the cluster. The interacting time between cluster and surface is as long as several ps, whereas the interaction between monomer and surface with same incident energy usually lasts less then 1ps. As the incident energy decreases, the penetration depth and interacting time decrease. When the incident energy is as low as 1keV (1.5eV/atom), the cluster does not penetrate the surface but collapses on the surface. The upper graph in figure 3.5 shows that the kinetic energy of re-evaporated cluster atoms is about 0.7keV totally and about 1eV per atom, at any incident energy. This phenomenon is considered to be the result of the thermalization of incident energy through the ‘multiple-collision’ effect.

Figure 3.6 shows the kinetic energy distributions of re-evaporated Ar atoms with different incident energy, 3.85ps after impact. In order to represent velocity distribution, the distributions are plotted as the function of the square root of kinetic energy. At the low energy impact, such as 5keV and less, collisions between the cluster atoms are not frequent, so that the incident cluster atoms directory reflected at the surface and the velocity distribution of the cluster atoms is shifted from the ideal Boltzmann distribution. As the incident energy increases, the number of collisions increases and the impact point is well thermalized during the period in which the incident cluster collides with the surface. Thus, the distribution becomes

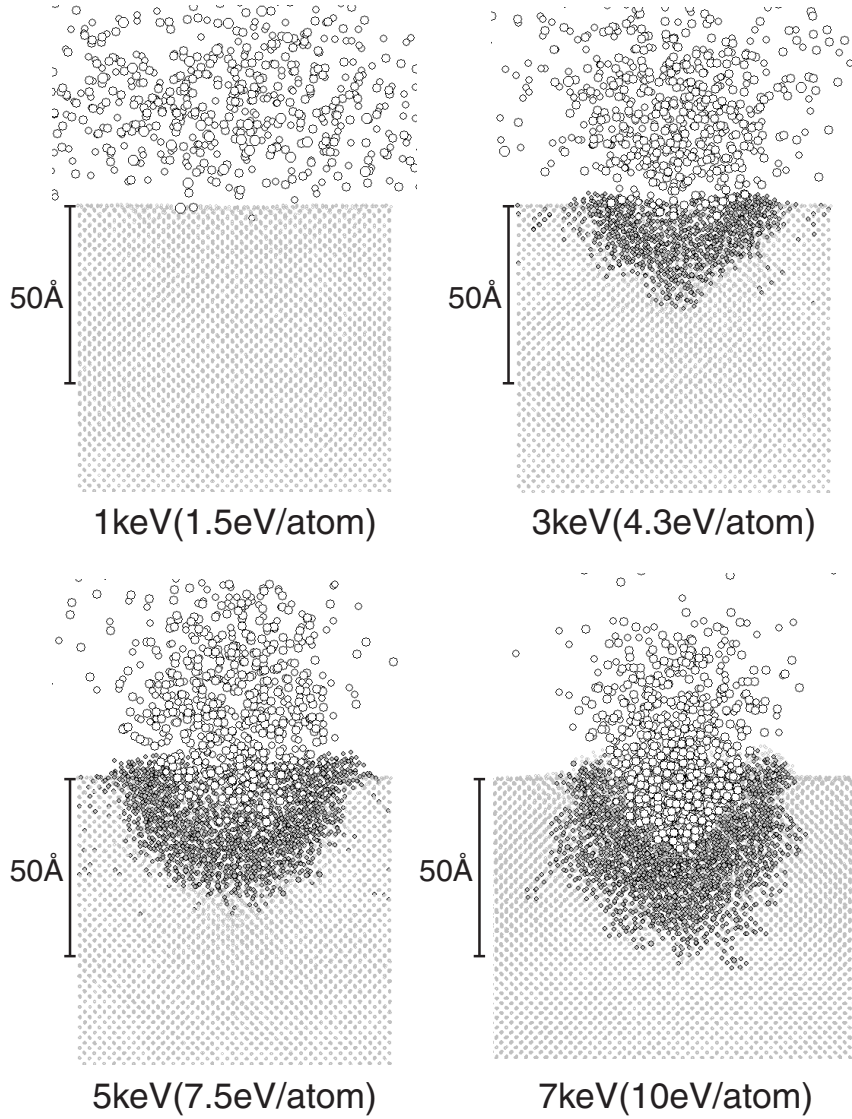


Figure 3.4: Snapshots of Ar_{688} impacting on $\text{Si}(001)$ with various incident energies, 3.85 ps after impact.

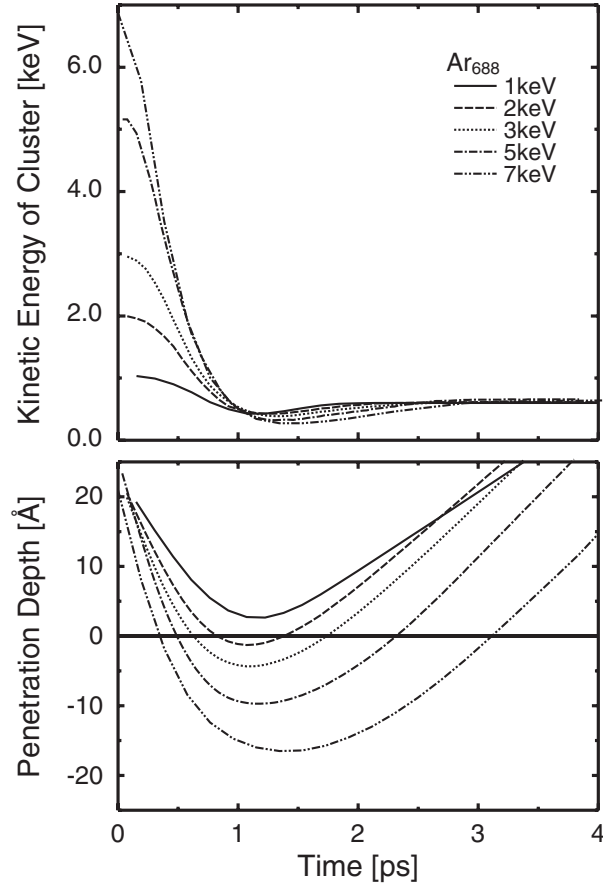


Figure 3.5: Time dependence of the total kinetic energy and the penetration depth of Ar_{688} cluster.

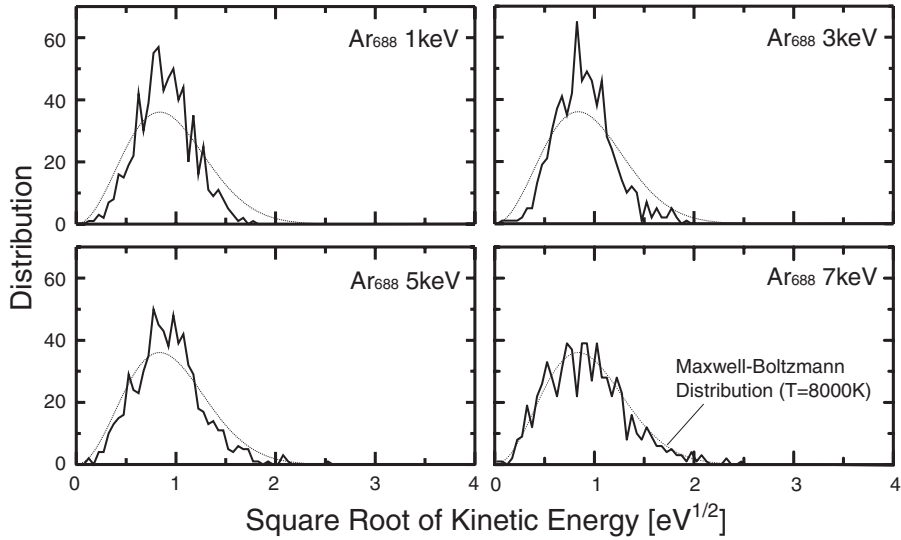


Figure 3.6: Kinetic energy distribution of re-evaporated Ar cluster atoms, 3.85ps after impact. Distributions are plotted as the function of square root of kinetic energy, which corresponds to velocity of particles.

similar in profile to the ideal Maxwell-Boltzmann distribution at a total incident energy of 7keV.

3.4 Energy and Size Dependence of Penetration Depth

3.4.1 Energy-per-atom Dependence

Figure 3.7 shows the energy-per-atom dependence of the maximum penetration depth (R_p) of Ar₄₃, Ar₆₈₈ cluster and Ar monomer. The R_p of Ar monomer is calculated by TRIM, which is a Monte-Carlo method to simulate the impact process of monomer ions^{26, 27}). The R_p of both Ar₄₃ and Ar₆₈₈ cluster are larger than that of monomer ion and are proportional to the cube root of the incident energy between 10eV/atom to 100eV/atom. The cluster can penetrate the surface even with low energy per atom because of the clearing-way effect and cause multiple-collision in the substrate. In this multiple-collision process, the incident energy and momentum are

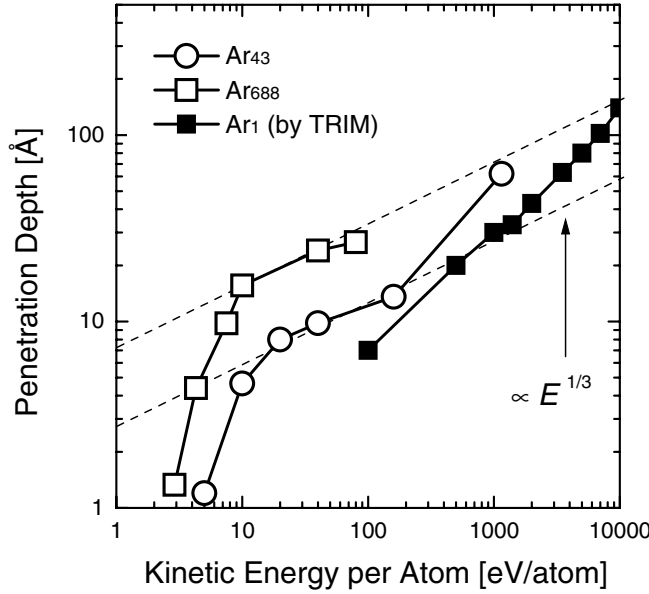


Figure 3.7: Energy-per-atom dependence of the maximum penetration depth of Ar_{43} and Ar_{688} cluster.

transferred isotropically and the cluster atoms expand hemispherically in the substrate. If the whole incident energy of the cluster is deposited onto the substrate to form a crater-like damage, the volume of the displaced region corresponds to the incident energy. Thus, if the shape of the displaced region keeps similar aspect ratio at any incident energy, it is considered that the penetration depth obeys a cube-root law as well as the radius and the depth of crater on the surface.

The cube-root law does not apply at both high-energy and low-energy regions as shown in figure 3.7. The threshold energy of nonlinear effect at low-energy side is 10 eV/atom and this energy is very close to the threshold energy of ion implantation for monomer ion⁵⁴⁾. If the incident energy is less than 10 eV/atom, the cluster does not penetrate the surface even with the help of the clearing-way effect and it collapses on the surface as shown in figure 3.4. Therefore, the R_p decreases rapidly at energies below 10 eV/atom, and approaches that of monomer ion with the decreasing incident energy. On the other hand as shown in figure 3.7, the threshold

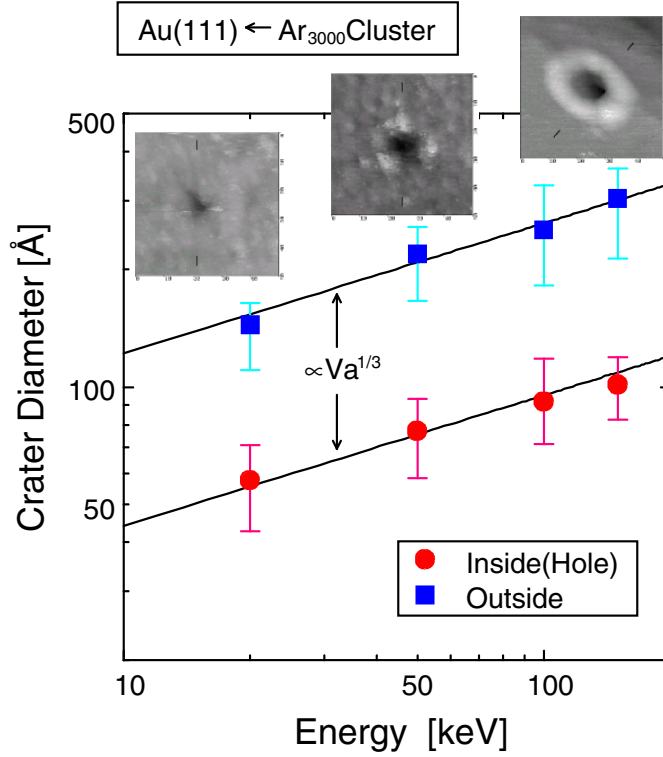


Figure 3.8: Energy dependence of the crater diameters with Ar cluster ions on Au surfaces, measured by STM.

energy at high-energy side is around 500eV/atom for Ar_{43} cluster. The R_p of Ar_{43} with 1150eV/atom, which is higher than this threshold energy, is larger than the one estimated by cube-root law. In this case, each Ar atom in the cluster collides with the substrate atoms and penetrates the substrate independently. Thus, the multiple-collision between incident atoms and the lateral expansion of cluster become less probable.

The cube-root law is confirmed by the experimental results by STM observation of gold surface irradiated with Ar cluster ions. Figure 3.8 shows the energy dependence of the inside and outside of the crater diameters measured by STM⁴⁹⁾. The target is Au(111) surface and is irradiated by Ar cluster with the energy ranging from 20keV to 150keV. The mean cluster size was 3000 atoms, so that the incident energy per one Ar atom ranges

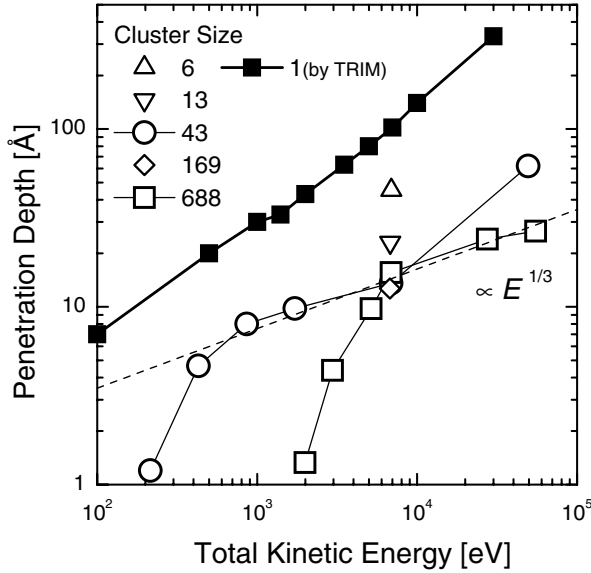


Figure 3.9: Total energy dependence of the maximum penetration depth of Ar clusters.

from 6.7eV/atom to 50eV/atom. As can be seen in figure 3.8, the diameter of crater is proportional to a cube root of the incident energy, which agrees result by MD shown in figure 3.7.

3.4.2 Total Energy Dependence

The total energy dependence of the R_p is shown in figure 3.9. Cluster is implanted to shallower region than monomer with same total acceleration energy, and the difference of R_p between monomer and cluster increases with the increase of incident energy. Figure 3.9 indicates that two different clusters in size but having same total kinetic energy, Ar₄₃ with 160eV/atom and Ar₆₈₈ with 10eV/atom, show same R_p , and the R_p of both Ar₄₃ and Ar₆₈₈ form one line represents cube-root law. These results imply that there is not size effect in R_p if the kinetic energy of the cluster is in the range where the R_p is proportional to a cube root of the incident energy. The R_p of Ar₁₆₉ with 7keV of the total incident energy shows similar value to Ar₄₃ and Ar₆₈₈, however, Ar₆ and Ar₁₃, which is smaller than Ar₄₃, shows deeper

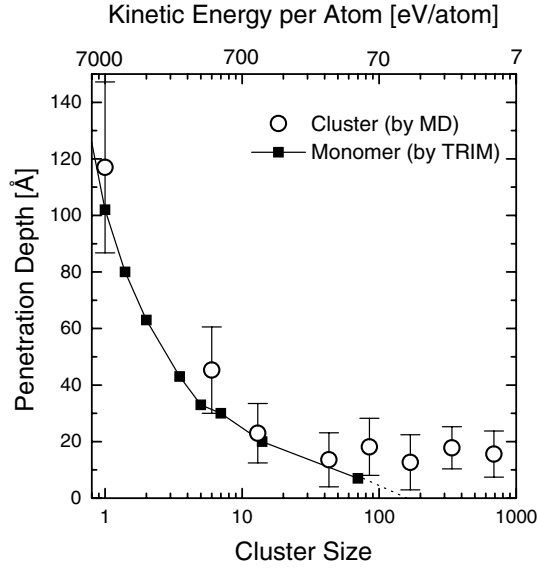


Figure 3.10: Cluster size dependence of the maximum penetration depth of Ar clusters.

R_p and become similar to that of monomer as the cluster size decreases. These result suggests that, as for the penetration depth, more than several tens atoms of cluster size is required to cause nonlinear effect at 7keV of total incident energy.

3.4.3 Cluster Size Dependence

Figure 3.10 shows the cluster size dependence of R_p at 7keV of total incident energy. The cluster size is changed from 1 (monomer) to 688. In order to obtain statistics, 100 simulations for Ar_1 , and 4 simulations for Ar_6 and Ar_{13} are performed with different impact point. The R_p of cluster shows the same value of about 17\AA at the cluster size of more than 43. However, the R_p of small cluster, Ar_6 and Ar_{13} are similar to that of monomer ion with same incident energy per atom, which means that the impact process of such small clusters can be considered as the independent monomer ion impacts. The incident energy per atom of Ar_{43} and Ar_{13} are given by 160eV/atom and 540eV/atom , respectively, so that the threshold energy-

per-atom to cause nonlinear effect can be considered as several hundreds eV/atom. This result consistent with the results in previous section and figure 3.7.

From these results, the conditions, with which a cluster shows the nonlinear effect in the penetration depth, are concluded as following;

- Cluster size is ranging from several tens to thousand.
- Incident energy is ranging from ten to several hundreds eV/atom.

A cluster which satisfies these conditions can be considered as one large particle independent of the cluster size and the R_p is proportional to cube root of the incident energy.

3.5 Damage Formation and Lateral Sputtering

3.5.1 Damage Formation Mechanism by Cluster Impact

As shown in figure 3.2, cluster impact causes characteristic damage on solid surface. The formation process of the damage by cluster impact is examined. Figure 3.11 shows the time evolution of the shape of displaced region at the impact of Ar_{688} cluster with 10eV/atom. The shape of damage is obtained from the mean radial distance of displacements, which are shown as dark-gray circles in figure 3.2, from the impact point on the surface. The displaced region spreads in both lateral and normal direction, and the hemispherical damage is formed because of the isotropic propagation of incident energy by the multiple-collision mechanism. This damage formation is different from so-called ‘point defect’ by monomer ion impact. In the case of cluster impact, a large number of substrate atoms are moved at the same instant, so that the damage region is considered to be amorphized under high-pressure and high-temperature. As can be seen in figure 3.11, the size of the damaged region reaches maximum at 1.5ps after impact and then it recovers and the incident Ar atoms are reflected. Finally, the hemispherical damage with the depth and radius of 30Å remains on the surface at 12ps after impact.

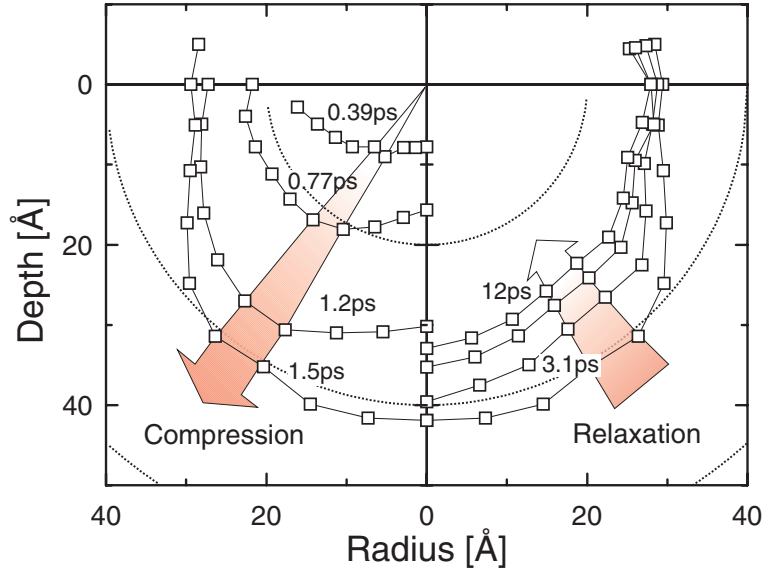


Figure 3.11: Compression and relaxation process in damage formation by Ar_{688} (10eV/atom) impact.

3.5.2 Size Dependence of Damage Formation

Figure 3.12 shows the profiles of damage caused by Ar_{13} , Ar_{43} and Ar_{688} cluster with the same total incident energy of 7keV. Each profile is taken at the time when it shows the maximum crater radius and depth in the collisional process. These argon clusters have different radii, but show almost similar profiles of damage and penetration depth, as shown in figure 3.10.

Figure 3.13 shows the penetration-depth dependence of the transitional kinetic energy of Ar cluster (ΔEk_{Ar}), kinetic energy of Si substrate (ΔEk_{Si}) and potential energy of Si substrate (ΔEp_{Si}), for Ar_{13} , Ar_{43} and Ar_{688} cluster impacts. Each cluster is accelerated to the same kinetic energy of 7keV. The cluster stops in the very shallow region in the substrate and transfers a large part of its kinetic energy to the substrate. In the case of Ar_{688} cluster impact, for example, the cluster loses 5.7keV of its kinetic energy during the impact process, and the ΔEk_{Si} , ΔEp_{Si} and the thermal bath gain 1.5keV, 3.9keV and 0.3keV, respectively. The profiles of ΔEp_{Si} , which corresponds to the defect formation energy, show a similar curve at

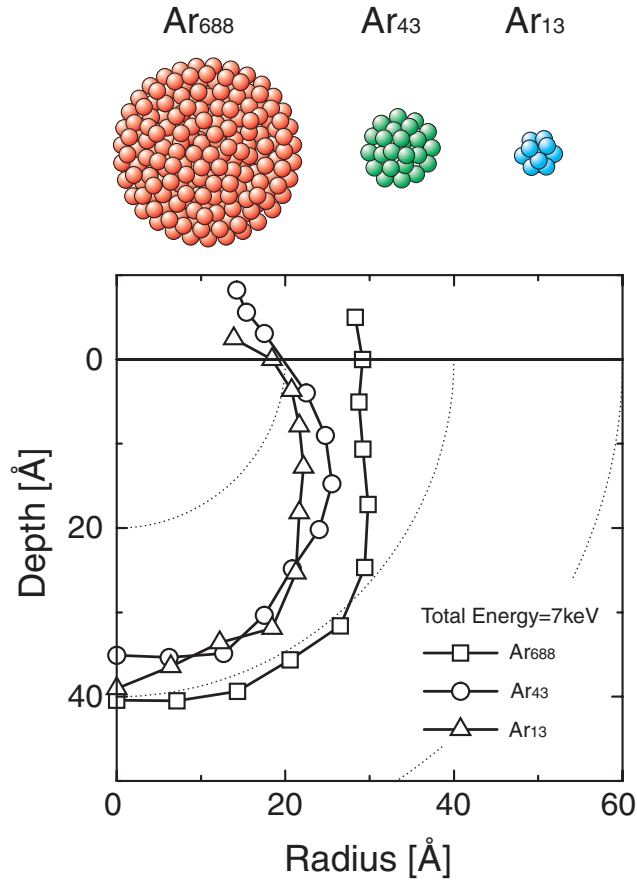


Figure 3.12: Profiles of damage formed by Ar_{13} , Ar_{43} and Ar_{688} with the same total incident energy of 7 keV.

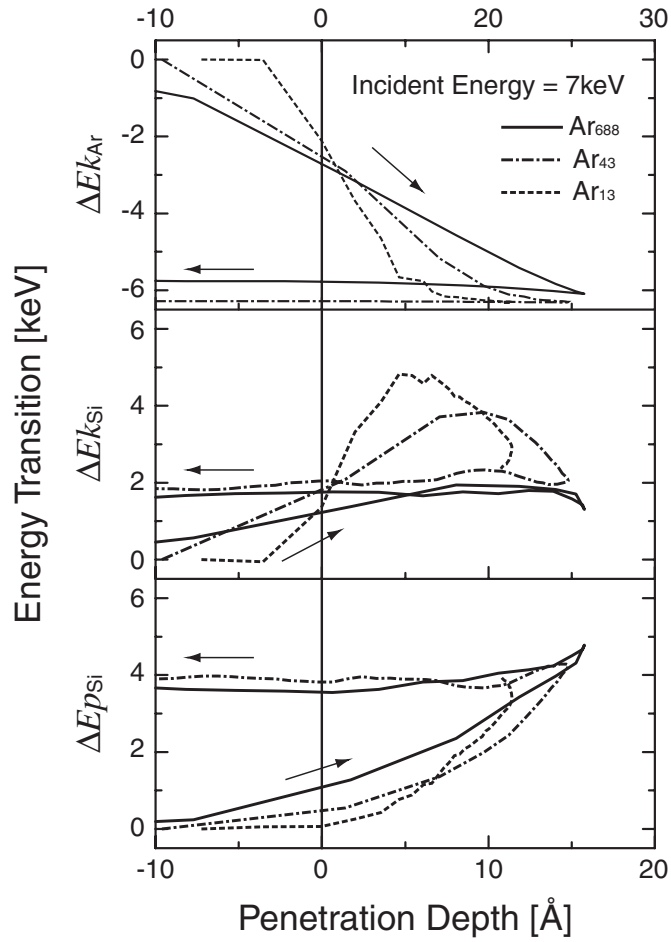


Figure 3.13: Penetration-depth dependence of the transitional kinetic energy of Ar cluster ($\Delta E_{k_{Ar}}$) and Si substrate ($\Delta E_{k_{Si}}$), and the potential energy of Si substrate ($\Delta E_{p_{Si}}$), for Ar₁₃, Ar₄₃ and Ar₆₈₈ cluster impacts

any cluster size, but the ΔEk_{Ar} and ΔEk_{Si} show evident dependency on the cluster size. In the case of the impact of large cluster such as Ar_{688} , the ΔEk_{Ar} transforms directly into ΔEp_{Si} and the ΔEk_{Si} does not change much. In the case of the impact of a small cluster such as Ar_{13} , however, the ΔEk_{Ar} rapidly decreases at the impact and ΔEk_{Si} increases at the same instant, so that the gain of ΔEp_{Si} is provided from the ΔEk_{Si} , and not from the ΔEk_{Ar} .

These results indicate the differences in the damage formation process between small and larger cluster impact. Figure 3.14 shows the model of damage formation process by large and small cluster impact. In the case of large cluster impact, the displacements are formed through direct collisions between the cluster and the surface atoms. On the other hand, the small cluster, in which each cluster atom has much higher kinetic energy than in the large cluster, generates a large number of substrate atoms with high-energy at the impact. These energetic substrate atoms collide with the other substrate atoms in the similar manner to cluster atoms in large cluster. Consequently, a similar shape of the damaged region is formed by both large and small cluster impact.

3.5.3 Lateral Sputtering

Figure 3.15 shows the snapshots of Ar_{688} cluster impacting on $\text{Si}(001)$ substrate with the incident energy of 80eV/atom, about 55keV totally. In such a higher energy impact, the cluster penetrates the substrate keeping itself in cluster state like the Ar_{688} 10eV/atom impact. As the incident energy increases, the height of the rim of the crater increases as well as the radius of the crater and some atoms on the rim of the crater are sputtered.

Figure 3.16 shows the kinetic energy and momentum profile at the impact of Ar_{688} with an acceleration energy of 80eV/atom. Each profile is taken at 0.2ps, 0.4ps and 1.2ps, respectively. The radius of the circle indicates the mean kinetic energy in a 5\AA square. The open circle shows the kinetic energy of the substrate atoms and the filled one shows that of the cluster atoms. The line drawn from each circle represents the magnitude and direction of momentum at each place. The profile of crater and kinetic

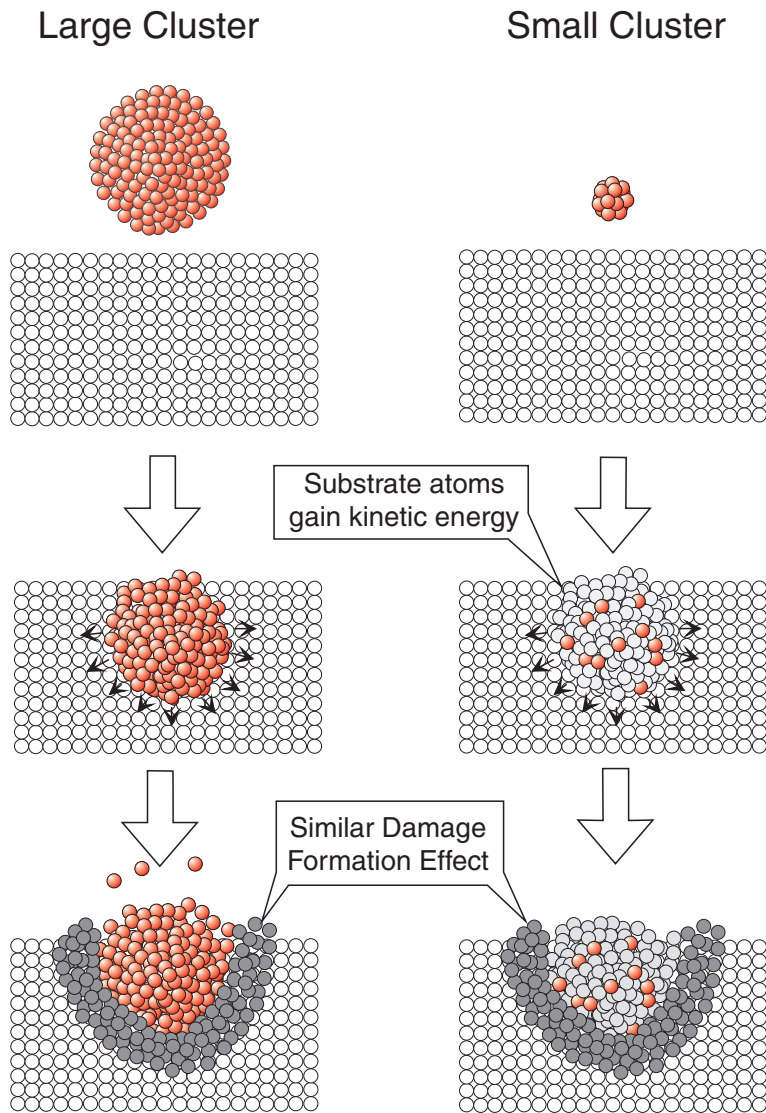


Figure 3.14: Model of damage formation process by large and small cluster impact.

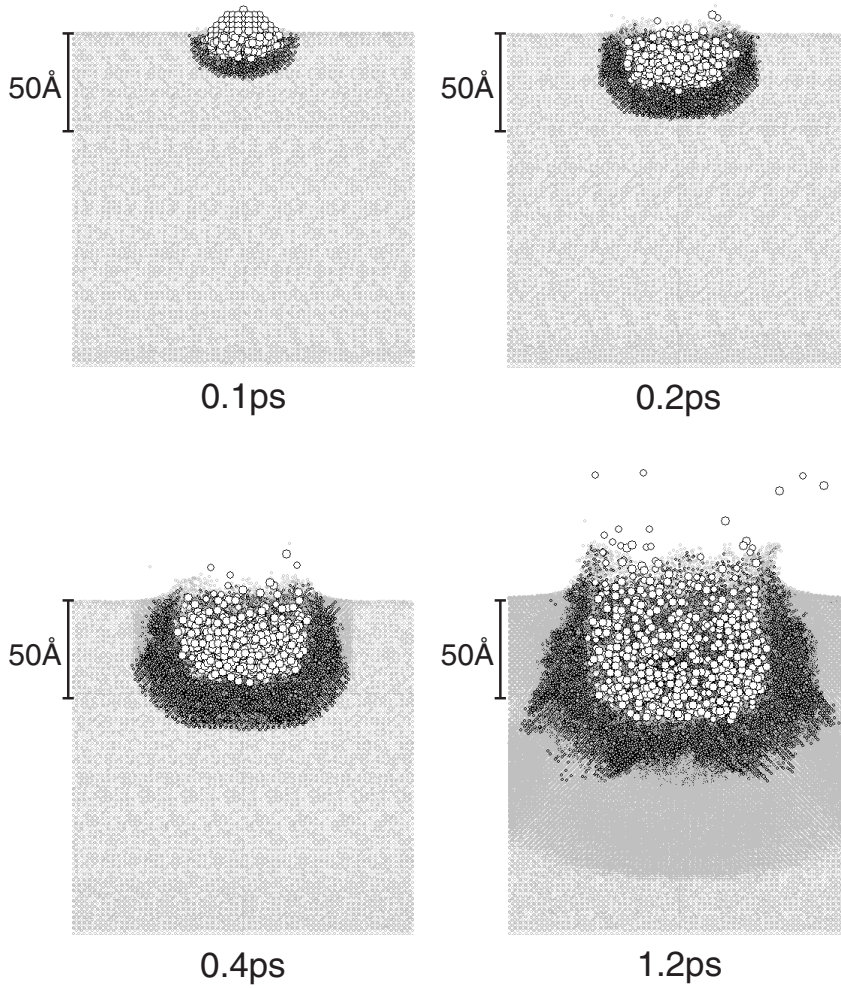


Figure 3.15: Snapshots of Ar_{688} with 80eV/atom impacting on $\text{Si}(001)$ substrate.

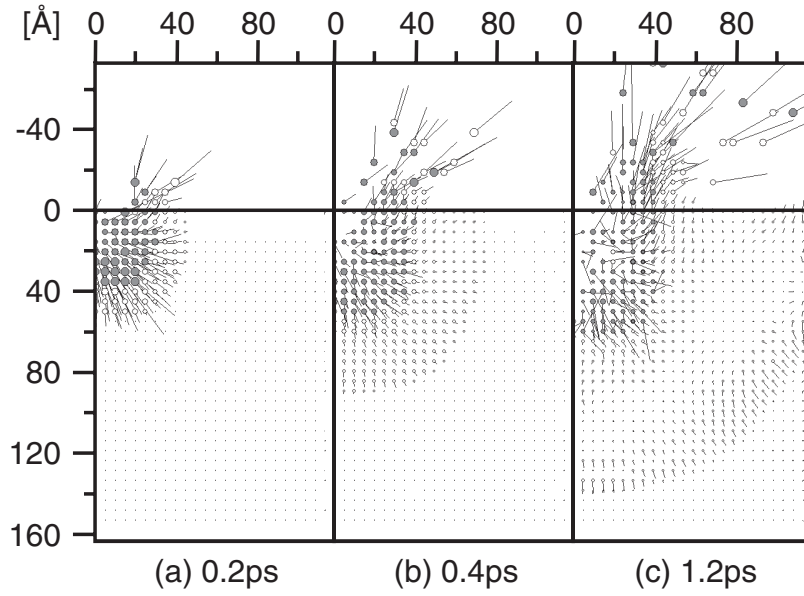


Figure 3.16: Energy and momentum profile at the impact of Ar_{688} with 80eV/atom .

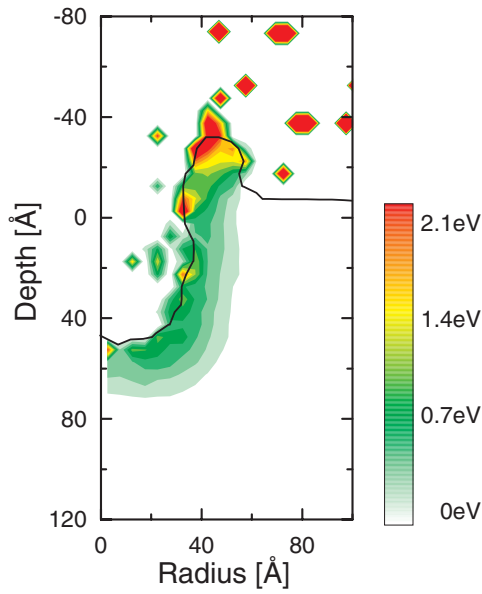


Figure 3.17: Kinetic energy distribution of substrate atoms, irradiated with Ar_{688} (80eV/atom) cluster, 1.2ps after impact.

energy distribution at 1.2ps is also shown in figure 3.17.

The momentum of the incident cluster is transported in the isotropic direction as the cluster impinges into the substrate and the substrate atoms surrounding the cluster are also displaced isotropically to form the crater structure. In this crater formation process, some atoms on the edge of the crater leave the surface in lateral direction to the surface, which is called ‘lateral sputtering’ and has been observed experimentally⁵⁵⁾. In figure 3.16, about 10 atoms are sputtered at 1.2ps after impact, but this number of sputtered atoms is much less than the measured experimental value, which is reported 25atoms/ion for Ar cluster of the size of 2000 and total incident energy of 20keV⁵⁶⁾. It is thought that the substrate atoms on the edge of the crater leave the surface in the following several pico seconds, because each atom in this region still has almost the same momentum and enough kinetic energy, above 2eV, to leave the surface, as shown in figure 3.17. These sputtered atom can be considered to leave the surface in the state of not only monomer, but also dimer, trimer and cluster because of the coherency of the momentum, which is supported by experimental observations⁵⁷⁾. These characteristic sputtering effects of cluster ion irradiation is caused by the crater-like damage formation process at the impact.

3.6 Summary

The characteristic impact processes of cluster ions were studied by molecular dynamics simulation of Ar cluster impacts on Si(001) surface. The results in this chapter are summarized as follows:

1. A large crater-like damage is formed on the surface by the impact of cluster, whereas monomer ion causes branched and interspersed displacements in the target by the cascade-collision model.
2. The penetration depth of cluster ions is larger than that of monomer ions with the same incident energy per atom. This is due to the clearing-way effect, in which the first cluster atom collides with a substrate atom and clears the substrate atom from its original site and

the following cluster atom can penetrate the surface without energy-loss.

3. On the other hand, the penetration depth of cluster shows lower than that of monomer with the same total incident energy. At the impact of a cluster, a large number of collisions occur between the cluster and the substrate atoms and the incident energy of cluster is transferred isotropically from the impact point. This multiple-collision effect causes a crater-like damage on the surface.
4. A cluster impact causes hemispherical crater-like damage whose volume is proportional to the incident energy of the cluster, and the penetration depth of cluster and the radius and depth of crater are proportional to a cube root of the incident energy. This characteristic penetration and damage formation effect by cluster impact can be observed at the cluster size ranging from several tens to thousand and the incident energy ranging several tens to several hundreds eV/atom.
5. During the crater-like damage formation process, some atoms at the edge of the crater leave the surface in lateral direction. This lateral-sputtering process by cluster impact is different from the sputtering by monomer ions and causes larger sputtering yield than monomer ion.

Chapter 4

Nonlinear Effects by High-energy Cluster Impact

4.1 Introduction

In chapter 3, MD simulations of Ar cluster impacting Si (001) surface were performed in order to examine the characteristic impact process by large cluster ion, and the range of cluster size and incident energy at which a cluster impact causes nonlinear effect were discussed. It is desirable to use much smaller and well-defined cluster ion beams to do a more precise analysis of the cluster irradiation effects. However, the Ar gas clusters obtained in experiments lie in the range from 100 to 3000 atoms, and have a broad size distribution, so that it is difficult to discuss the size dependence of nonlinear effect by small cluster impact. Fullerene (C_{60}), which is a large stable carbon molecule, enables us to obtain a well-selected cluster ion beam and is useful for investigating the nonlinear irradiation effects of cluster ions.

A number of groups have examined the peculiar irradiation effects produced by fullerene impact by both simulation and experiment. Webb et al. have performed MD simulation of fullerene impact and have shown that the damage yield per one C atom for cluster size 60 to 84 is the same, but is several times higher than that by a monomer with the same energy-per-atom⁵⁸). On the other hand in experiments, Perez et al. have found that a high energy (about 1MeV/atom) small carbon cluster, with a size of less than 10, shows a larger number of displacements in the shallow region but a similar number in deeper regions⁵⁹). Both their results indicate that

drastic changes in irradiation effects are expected in a cluster size ranging from 1 (monomer) to 60.

In this chapter, molecular dynamics simulations of carbon clusters impacting carbon surface were performed. First, the penetration processes of C_{60} into a diamond substrate are discussed at various incident energies ranging from several tens eV/atom to several keV/atom. The penetration depth and the stopping power of C_{60} are examined, and the boundary energy to discriminate the linear and nonlinear effect are discussed. The energy dependence of damage formation yield is also examined by both MD simulation and experiments of C_{60} impact. Next, MD simulations of various sizes of carbon cluster impacting on a Highly Oriented Pyrolytic Graphite (HOPG) substrate are performed in order to examine the size-dependence of the damage formation by cluster ion impact. The results from MD simulation are compared with those obtained by STM observations of single traces on the surface produced by cluster ion impact, which are performed with the similar conditions to the MD simulations.

4.2 Simulation Model

Tersoff's empirical model potential⁴⁴⁾ was applied to describe the interaction between carbon atoms, which is given by eqn. (2.25)–(2.32) and table 2.3. Diamond (001) and Highly Oriented Pyrolytic Graphite (HOPG) surface were prepared as the target material. For both targets, the maximum number of carbon atoms was about 260,000, where the corresponding dimensions are 120\AA^3 (2048atoms/ML \times 128ML) for diamond, and 120\AA^2 area and 180\AA depth (5408atoms/ML \times 50 ML) for HOPG. Periodic boundary conditions were applied to the horizontal boundaries, and the atoms of the lowest layer were fixed to retain the bulk structure. The initial temperature of the target was 0 K.

The C_{60} molecule was constructed by locating carbon atoms at the vertices of a truncated icosahedron. By using Tersoff's potential model, the radius of C_{60} is 3.68\AA , which gives a minimum potential energy of -405eV . In addition to C_{60} , C_1 , C_4 , C_8 , C_{19} were also irradiated on the HOPG substrate in order to examine the cluster size dependence on the

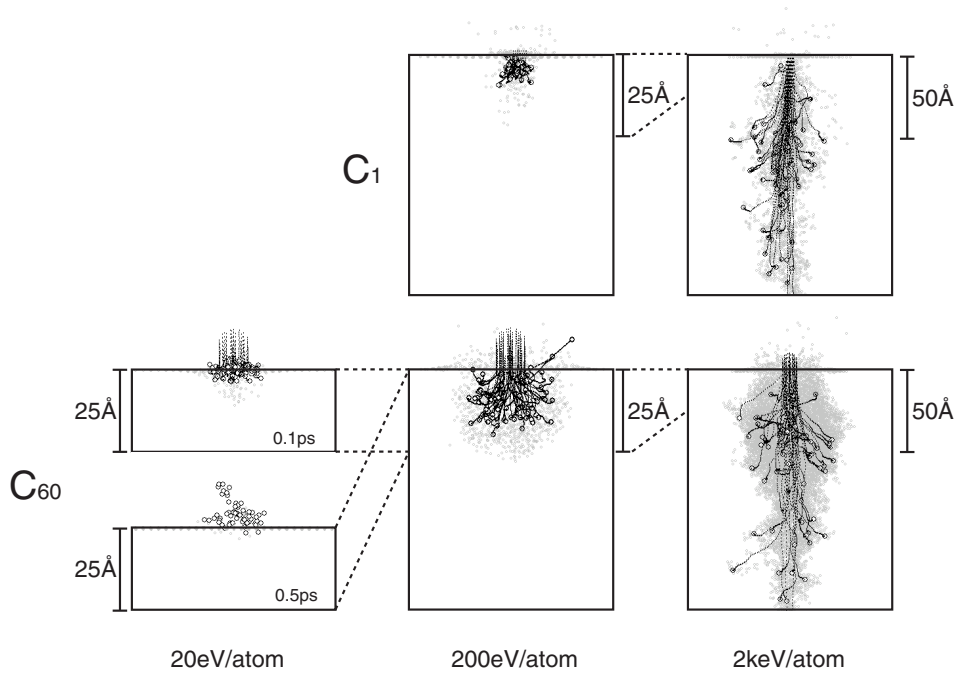


Figure 4.1: Snapshots of C_1 and C_{60} impacting on diamond (001) surface, 0.1ps after impact. White circles and black dots are incident C atoms and their trajectories, respectively. Gray dots are displaced substrate atoms. The snapshots of C_1 are made by overlapping each one of 64 trials.

impact process of a cluster ion. Each cluster was constructed by locating the carbon atom at the vertices of a tetrahedron (C_4), octahedron (C_8) and fcc structure (C_{19}). The radii of both clusters were set to give the minimum potential energy. Both ions were directed and implanted at normal direction toward the surface. For simulation of C_1 , 128 trials have been done and the result is averaged in order to obtain a statistical value of penetration depth and displacement yield.

4.3 The Penetration Process of C_{60} into Diamond

4.3.1 Penetration Depth of C_{60}

The penetration process of C_{60} in the diamond substrate was examined with various energies ranging from several tens eV/atom to several keV/atom.

Figure 4.1 shows the snapshots of C_1 accelerated with 200eV/atom and 2keV/atom, and C_{60} with 20eV/atom, 200eV/atom and 2keV/atom, impacting on a diamond (001) surface. C_{60} impacts on the surface in normal direction to the surface, but C_1 impacts with the incident angle tilted 7° from a surface normal and twisted 30° to (100) direction in order to avoid channeling. In figure 4.1, the open circles indicate the coordinates of irradiated carbon atoms at the moment, black dots show their trajectories and the gray dots indicate displaced substrate atoms that are defined as atoms having potential energy 2eV above the bulk state. Under this definition, the corresponding displaced distance from the lattice site was calculated to be more than 0.4\AA , but this definition avoids displacements due to deformation of the lattice structure to be taken into account. The figure shows the picture 0.1ps after impact for each energy, and for C_{60} with 20eV/atom at 0.5ps after the impact. The snapshots of C_1 were made by overlapping each one of 64 trials.

In the case of 20eV/atom, C_{60} is compressed in the normal direction and consequently collapses at the surface of the target. Almost all of the carbon atoms of C_{60} re-evaporate within the following 1ps, and have short interaction time with the surface atoms. Very few atoms are displaced in the target. This result is in good agreement with other simulations of C_{60} impact reported by other groups^{60, 61, 62}). When the energy is 200eV/atom, C_{60} impinges into the target deeply compared with C_1 with 200eV/atom. In the collisional process, all carbon atoms in C_{60} keep close to each other and a hemispherical displaced region is formed around the impacting C_{60} . Some implanted atoms are leaving the surface, and crater-like damage is left behind. This impact process of C_{60} is similar to that of Ar clusters with size ranging from tens to several thousands and total acceleration energy from 1keV to 50keV onto Si(001) surface, as shown in chapter 3. This result suggests that C_{60} with 200eV/atom, which consists of a smaller number of

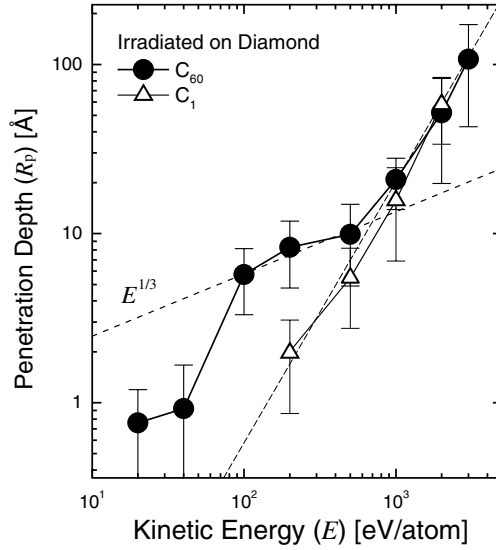


Figure 4.2: Energy dependence of the penetration depth (R_p) of C_{60} and C_1 into diamond.

atoms than the Ar clusters in former experiments and simulations, presents the same characteristics of the cluster impact process as large Ar cluster.

As the incident energy increases, the lateral dispersion of incident atoms reduces, whereas the penetration depth increases. In the case of the incident energy of 2keV/atom, a C_{60} penetrates into the substrate without interruption, but after embedding itself into the substrate it dissociates to individual carbon atoms, and each incident atom implants into the substrate obeying the collision cascade mechanism. The trajectories of C_{60} become similar to those of monomer ions with the same incident energy per atom. The shape of the damaged region in the shallow surface region changes from hemispherical to cylindrical. At the end of the range of the cylindrical displacement, far from the surface, interspersed displacements occur due to a collision cascade mechanism¹¹⁾. In the following section, the nonlinearity of penetration of C_{60} will be explained using two models — the ‘clearing-way’ effect and the ‘multiple-collision’ effect.

4.3.2 Clearing-way Effect

Figure 4.2 shows the dependence of the penetration depth (R_p) of C_{60} and carbon monomer on the kinetic energy per atom. Carbon monomer results are calculated by averaging the penetration depths of 128 carbon atoms. When the kinetic energy is between 100eV/atom to 1keV/atom, C_{60} penetrates deeper than carbon monomer (C_1) with the same kinetic energy per atom. This is caused by the ‘clearing-way (CW) effect’ as a consequence of high-density irradiation. The CW effect occurs when one incident atom follows another atom, which clears the way for the following atom. The following atom can penetrate into the solid without energy loss³²⁾.

4.3.3 Multiple-collision Effect

When the particles of a cluster are implanted into the substrate, a large number of collisions occur between the implanted atoms and the target atoms. These implanted atoms, whose momentum before impact only had a vertical component, are given a lateral component to the surface during the collisional process. Finally, implanted atoms spread isotropically from the center of the impact area and this effect is called the ‘multiple-collision (MC) effect.’ The kinetic energy of C_{60} is transferred to the defect formation energy isotropically because of the MC effect. Consequently, a hemispherical crater-like damaged area is formed, as shown in figure 4.1 (200eV/atom). In this case, both the radius of the crater and the R_p are proportional to the cube root of incident energy. The impact process of cluster ion is therefore described as a combination of two nonlinear effects, the CW effect and the MC effect.

As the energy increases, the R_p of C_{60} does not follow the cube root law and converges to the R_p of carbon monomer with the same velocity. Figure 4.3 shows the penetration depth dependence on the ratio of the lateral component (E_{xy}) to the total kinetic energy (E). When the incident energy is less than 1keV/atom, the ratio E_{xy}/E increase and converges to a value of 2/3 while the cluster implants into the surface. This result confirms that the kinetic energy of the cluster disperses isotropically by the MC effect. However, when the kinetic energy is above 2keV/atom, the MC effect is

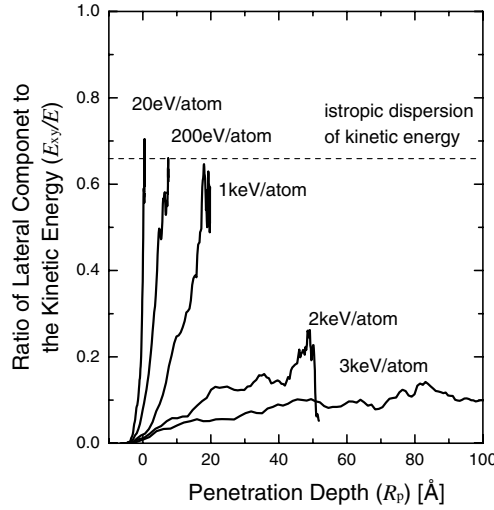


Figure 4.3: Penetration depth dependence of the ratio of lateral component of kinetic energy (E_{xy}) to the total kinetic energy (E). The value of $2/3$ indicates that the incident energy, which has only vertical component before impact, is transferred to isotropic direction from the impact point.

reduced, and C_{60} penetrates into the target without dispersing its kinetic energy in lateral direction.

4.3.4 Nonlinearity in Stopping Power

The stopping power (SP) of C_{60} was examined in order to explain the energy dependence of the CW and MC effects of C_{60} cluster impact. Figure 4.4(a) shows the transition of kinetic energy of C_{60} in the diamond substrate as a function of the penetration depth, and 4.4(b) shows the SP of C_{60} . The SP is which is calculated by differentiating its mean kinetic energy by its mean penetration depth ($-dE/dR_p$), which is given in figure 4.4(a). In figure 4.4(b), thick lines indicate the SP of C_{60} implanted with various energies from 20eV/atom to 5keV/atom. Dashed lines, marked as S_n , represents the nuclear stopping power for a carbon monomer in a diamond target with ZBL potential model given by eqn. (2.9).

For C_{60} , the profile of SP does not follow S_n and varies according to

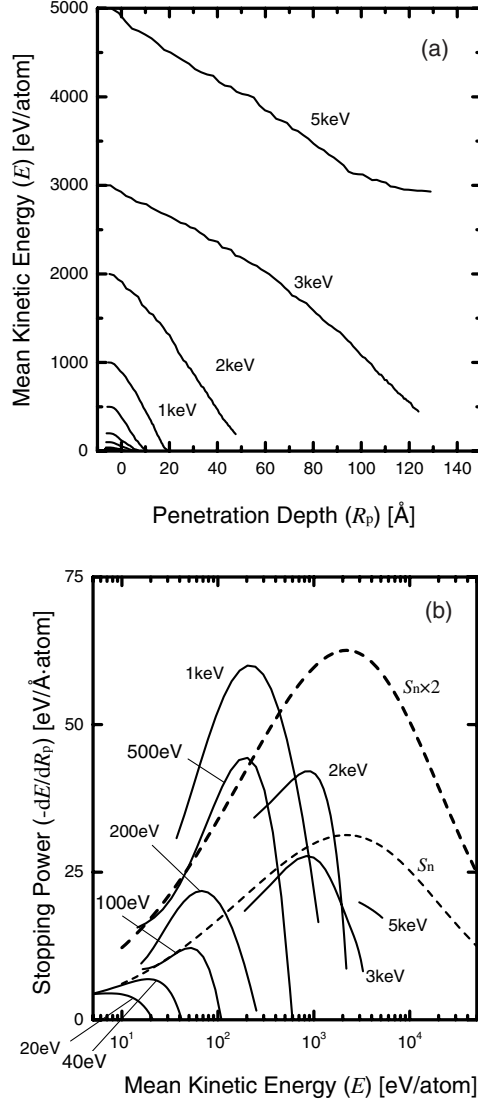


Figure 4.4: Kinetic energy loss of the C_{60} as the function of the penetration depth (upper:a), and stopping power of C_{60} in diamond substrate (lower:b). The stopping power is calculated from the upper graph by differentiating the mean kinetic energy by the penetration depth

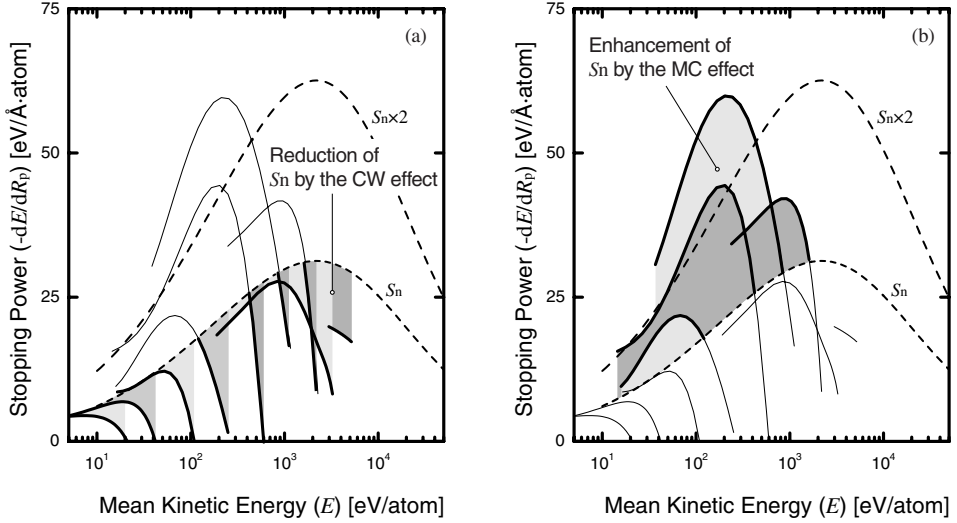


Figure 4.5: Classification of the nonlinearity in the stopping power (SP) at C_{60} impact. The left figure indicates the reduction of SP by the clearing-way (CW) and the right one is the enhancement by multiple-collision (MC) effect.

incident energy. The shift of SP can be classed into two regions, as shown in figure 4.5. The first one is the region where the SP is less than the S_n and appears in the initial stage of the impact of every cluster, which is shown by figure 4.5(a). The other region is where the SP is larger and it appears when the incident energy of the cluster is in the range from 200eV/atom to 2keV/atom, as shown in 4.5(b). The former region is explained as the result of the CW effect and the latter as the result of the MC effect.

Reduction of Stopping-power by the Clearing-way Effect

Figures 4.6 and 4.7 show the schematics to explain the transformation of the SP by the CW and MC effect, respectively. In the very early stage of the impact, only one carbon atom of C_{60} collides with the target. Therefore, the SP of C_{60} in the initial stage can be $1/N$ (where N is cluster size) of S_n as shown in the left side of figure 4.6. In fact, all atoms of C_{60} impact within a finite area of the target with high-density. The SP of the cluster is reduced according to the density of irradiated atoms. If only M atoms

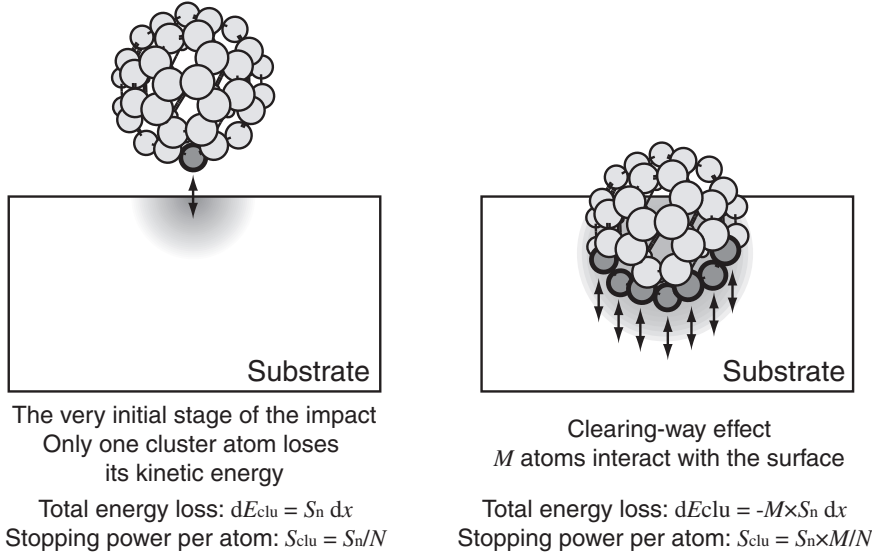


Figure 4.6: Schematic model of the transformation of stopping power by the clearing-way effect.

in the cluster with the size of N collide with the substrate and lose their kinetic energy, but other $(N - M)$ atoms do not transfer the kinetic energy to the substrate because of the CW effect, as shown in the right side of the figure 4.6, the total energy loss of the cluster is given by;

$$dE_{clu} = -M \times S_n dx. \quad (4.1)$$

Thus, the transformed SP of the cluster by CW effect is reduced to;

$$S_{CW} = -\frac{dE_{clu}}{dx} \frac{1}{N} = S_n \times \frac{M}{N}. \quad (4.2)$$

The reduction of the SP causes both the increase of R_p and the decrease of threshold energy of implantation into the surface. The CW effect is an intrinsic characteristic of cluster and is found to be independent of incident energy. When the kinetic energy is less than 100eV/atom, C_{60} cannot overcome the surface potential to penetrate the target even if the CW effect is taken into account and R_p decreases rapidly. C_{60} with such low kinetic energy collapses on the surface of the target.

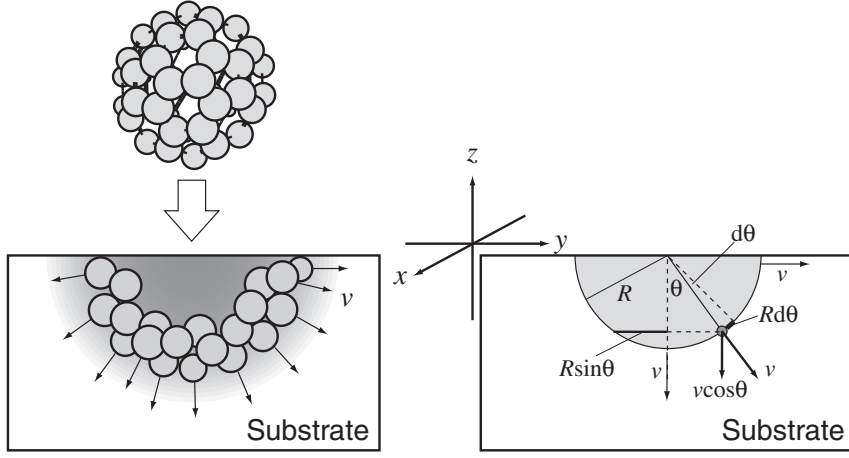


Figure 4.7: Schematic of the transformation of stopping power by the multiple-collision effect. Each cluster atom has same velocity, v , and spreads hemispherically from the impact point.

Enhancement of Stopping-power by the Clearing-way Effect

When the incident energy is between 200eV/atom to 2keV/atom, the SP of C_{60} is higher than S_n . The atoms of C_{60} cluster, which are implanted deeper than C_1 because of the CW effect, are scattered isotropically from the center of C_{60} , due to the MC effect. If we suppose that each cluster atom on the hemispherical interface of cluster and target has the same velocity v and spreads in normal direction to the interface, the velocity of the center of mass of the cluster, \bar{v}_{clu} , can be obtained by averaging the z -axis component of the velocity, as shown in figure 4.7;

$$\bar{v}_{clu} = \frac{1}{2\pi R^2} \int_0^{\pi/2} v \cos \theta \, 2\pi R \sin \theta \, R d\theta = \frac{1}{2}v. \quad (4.3)$$

Eqn. (4.3) leads to the transformed SP by the MC effect;

$$S_{MC} = -\frac{dE_{clu}}{dx} \frac{1}{N} = \frac{S_n N \cdot v dt}{\bar{v}_{clu} dt} \frac{1}{N} = 2S_n. \quad (4.4)$$

Consequently, the total SP of a C_{60} by the MC effect is evaluated as being larger than that of a monomer. The range of incident energies for the MC effect is narrower than that of the CW effect. The reason for this is that

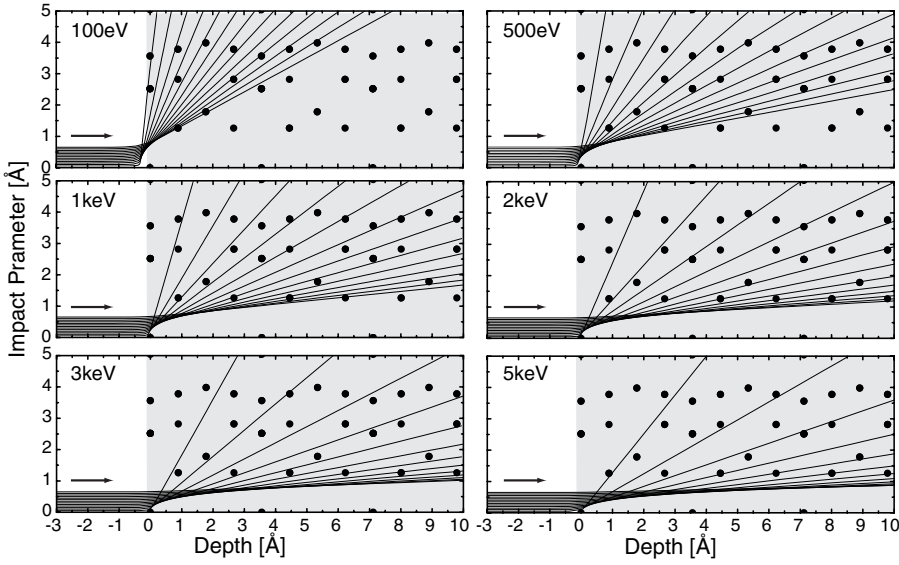


Figure 4.8: Profiles of shadow cones formed by carbon atoms impacting on a diamond substrate with various incident energies. The black circles indicate the position of target carbon atoms in the diamond structure.

the required number of collisions between cluster and surface atoms for the MC effect is larger than that for the CW effect.

Energy Boundaries to Cause Nonlinear Penetration Effect

The number of collisions depends on the cross-section of impact and, therefore, on incident energy. Figure 4.8 shows the profiles of shadow cones formed by carbon atoms impacting on a diamond substrate with various incident energies. Each line in these figures indicates the trajectory of an incident carbon atom, which collides with the target carbon atom at (0,0) with various impact parameters. The black circles are the coordinates of target carbon atoms in the diamond structure, which indicate how long the incident carbon can penetrate into the substrate until next the collision with a substrate atom.

In the case of low-energy ion impact such as 100eV and 500eV, the incident atom is largely scattered at first collision and then it is considered

to collide with the next substrate atom which resides shallower than the depth of 1 unit-cell. If a cluster impacts on the surface with such a low incident energy, the first atom to collide with a surface atom is largely scattered to a lateral direction and the atom can reside in shallow region, which causes the lateral dispersion of the cluster and a large number of collisions between first incident atom and the following ones.

As the incident energy increases, the cross-section of the impact decreases and the incident atom become to penetrate to the deep region substrate without secondary collision with the target atoms, which corresponds to the decrease of the S_n at high energy region. In this case, the incident atoms of the cluster are implanted into the substrate independently and do not cause the MC effect, which means that the penetration process of each cluster atom is similar to that of monomer. As for the impact of carbon on diamond surface, the stopping power decreases at the kinetic energy above 2keV/atom. Therefore, C_{60} with an energy higher than 2keV shows similar property with the independent carbon monomer, as shown in figure 4.2. The kinetic energy of 2keV/atom is the energy where the maximum stopping power is given for C monomer, and also considered as the boundary energy at which the CW and the MC effects are balanced in energy loss, and the R_p shows the same value as that of monomer.

4.3.5 Damage Formation by C_{60} Impact

The characteristics of damage formation by C_{60} cluster impact were examined with various energies. Figure 4.9 shows the time dependence of the number of displacements per incident atom for C_{60} and C_1 . The number of displacements caused by C_1 impact is calculated by averaging the results of 128 trials. At 0.1 ps after impact, about 20, 40 and 200 displacements/atom are formed by C_{60} impact with the incident energy of 200eV/atom, 500eV/atom and 2keV/atom, respectively. Each value is 4 to 7 times higher than those produced by monomer ions because of the different mechanism to form displacements.

In the case of monomer ion impact, displacements are formed by knock-on mechanism and tend to result in point defects. In the case of clusters

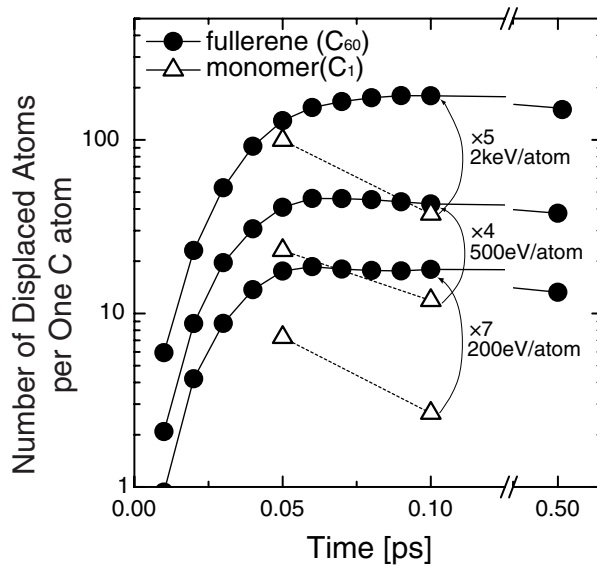


Figure 4.9: Time dependence of the number of displacements per one carbon atom formed by irradiation of C_{60} and C_1 with the energy of 200eV/atom, 500eV/atom or 2keV/atom.

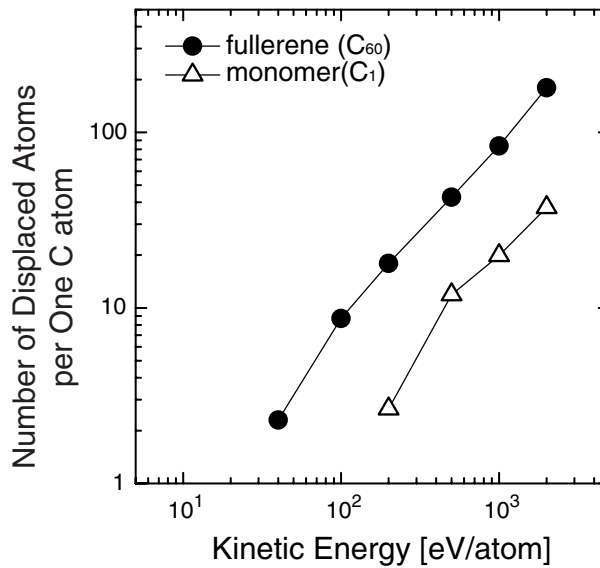


Figure 4.10: Incident energy dependence of the number of displacements formed by C_{60} and C_1 .

such as C_{60} , the opposite occurs. The kinetic energy of cluster is transferred to the substrate atoms around the cluster by a collective movement and more homogeneously. Hence, the mean potential energy of each displacement produced by cluster is much less than by monomer ion, but a large number of displacements are formed. These results imply that the amorphous damaged region can be formed by low-dose cluster radiation. The difference of damage formation process is also shown in the recovery process. In each case of monomer ion irradiation, the number of displacements decreases during the period of 0.05 ps to 0.1 ps, whereas the number of displacements by cluster ion impact remains almost constant even after 0.5ps.

Figure 4.10 shows the energy dependence of the displacement yield, which is the number of displacements induced by one incident atom. As comparing with the penetration depth shown in figure 4.2, the displacement yield by cluster ion shows different property against the incident energy from the penetration depth. In the case of energy ranging from 200eV/atom to 2keV/atom, the displacement yields of C_1 and C_{60} are proportional to the incident energy, and the yield of C_{60} is from 4 to 7 times higher than that of C_1 . However, the profile of penetration depth of C_{60} becomes much steeper, as the incident energy increases above 2keV/atom.

Figure 4.11 shows the depth profiles of displacements in diamond by C_{60} and C_1 implantation, 0.1ps after impact. In figure 4.11, both C_{60} and C_1 are irradiated with the energy of 200eV/atom and 2keV/atom. At 200eV/atom of incident energy, C_{60} impact causes larger displacements and deeper distribution in the substrate than C_1 because of the clearing-way effect. On the other hand, at the impact with 2keV/atom, the range of damaged area by C_{60} is similar to that by C_1 , as well as the penetration depth at the high-energy region. However, a larger number of displacements are formed in the shallow substrate region, whereas a similar profile to C_1 is shown in the deep substrate region, more than 50Å from the surface. At high-energy cluster impact, the atoms in the cluster penetrate the surface without interacting with other cluster atoms, as mentioned in the previous section, but produce a large number of high energy target atoms near the surface region with high density. These high-energy substrate atoms cause

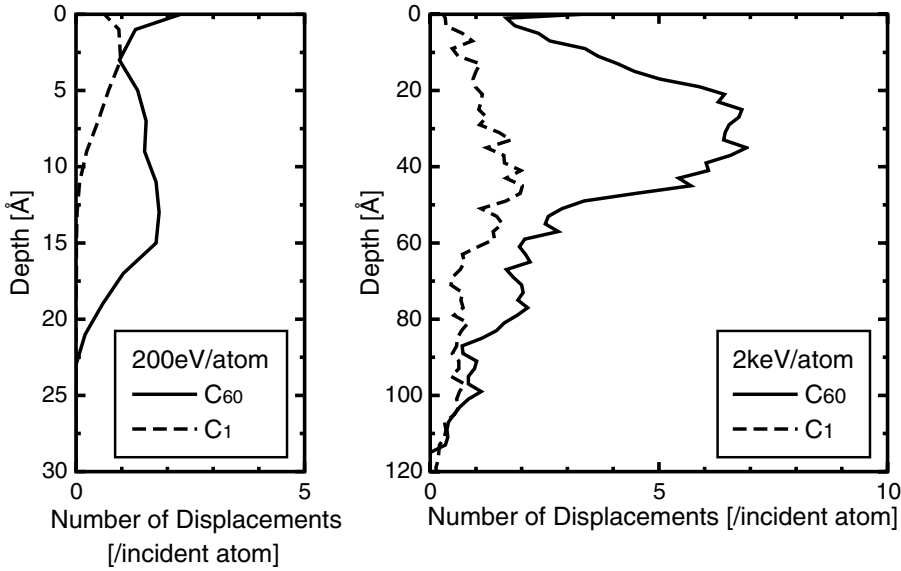


Figure 4.11: Depth profile of displaced carbon atoms in diamond by C_{60} and C_1 impacting with 200 eV/atom and 2 keV/atom, 0.1 ps after impact.

the multiple-collision effects in the similar manner to the cluster atom at the middle range of the kinetic energy.

The damage formation yield by C_{60} were measured experimentally. C_{60} and C_2 ions were radiated onto sapphire surface and the displacement of Al atoms were measured by Rutherford back-scattering (RBS) spectroscopy⁶³⁾. Figure 4.12 shows the atomic dose dependence of the number of displaced Al atoms in sapphire irradiated with C_{60} and C_2 . Both C_{60} and C_2 were radiated with the same energy of 5 keV/atom. In each case, the number of displacements saturates around 8.5×10^{16} atoms/cm² at the atomic dose of 6.0×10^{15} atoms/cm². The saturation value is equivalent to the projection range of incident atoms and this result implies that both C_{60} and C_2 ions with incident energy of 5 keV/atom have the same projection range. When the number of displacements is not saturated, the displacements increase with increasing atomic dose, and the displacement yield can be calculated. The displacement yield of C_{60} and C_2 are about 400 and 90, respectively, and the ratio of the yield of C_{60} to the one of C_2 is 4.4. This

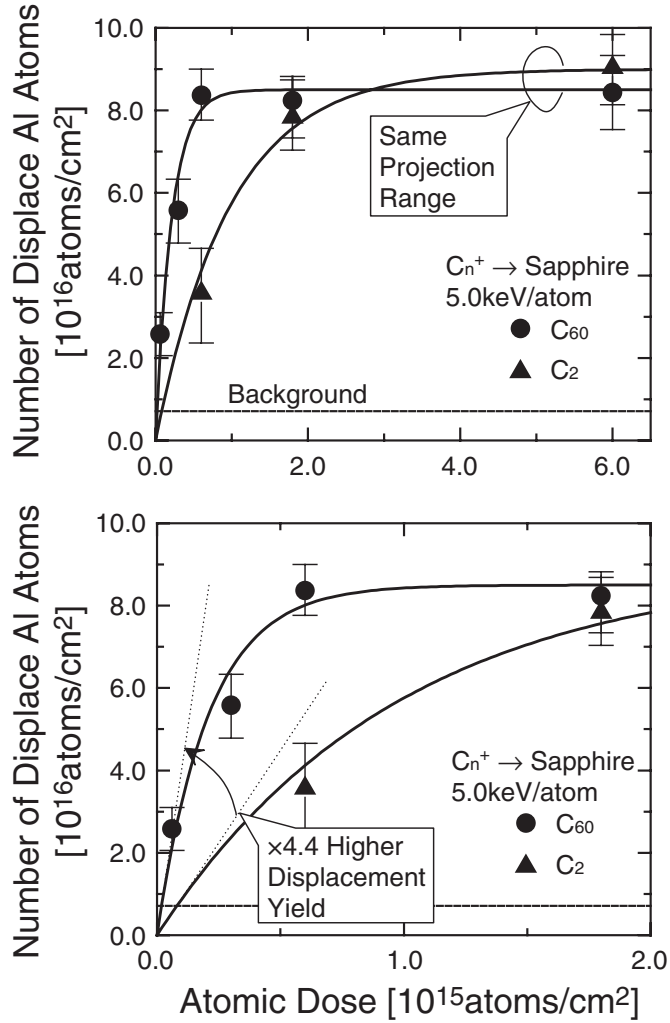


Figure 4.12: Atomic dose dependence of the number of displaced Al atoms in sapphire irradiated with C_{60} and C_2 , measured by RBS. The incidence energy of both C_{60} and C_2 is 5keV/atom. The lower figure shows the magnified view of the upper one.

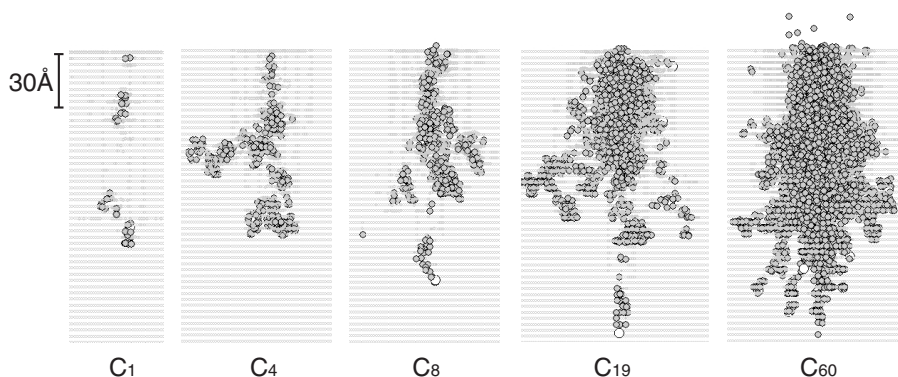


Figure 4.13: Snapshots of various sizes of cluster ion impacting on HOPG surface with the energy of 2keV/atom. Large open circles indicate the incident carbon atoms. Gray ones indicate displaced substrate. Each figure shows the picture 0.1ps after impact.

ratio agrees with the results of MD simulation, as shown in figures 4.2, 4.9 and 4.10.

4.4 Cluster-size Effect on Small Carbon Cluster Impact

4.4.1 MD Simulation of Small Carbon Cluster Impact

Figure 4.13 shows snapshots of various sizes of carbon clusters impacting an HOPG surface at the time of 0.1ps after impact. Each cluster is accelerated with an energy-per-atom of 2keV/atom so that, C_{60} , for example, has 120keV total incident energy. A large white circle indicates the incident carbon atom and a large gray circle indicates the displaced substrate atoms.

In the case of the C_1 impact, interspersed damaged areas are formed through the cascade-collision mechanism. It is shown that both C_4 and C_8 form interspersed displacements in similar way to the C_1 . However, in the case of the C_{19} and C_{60} impacts, a different shape of displacement is formed in the shallow region of the substrate because of a nonlinear effect

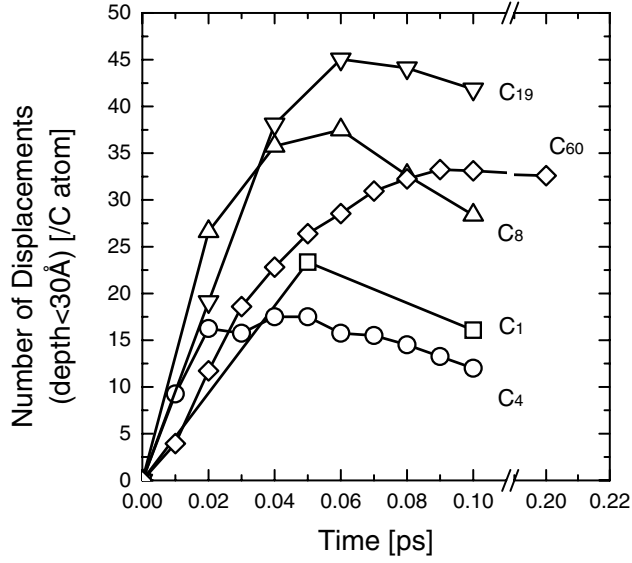


Figure 4.14: Time dependence of the number of displacements on the surface induced by various sizes of carbon clusters. The number of displacements is normalized to that by one constituent atom in the cluster.

of high-density particle irradiation.

When the cluster size increases, the higher energy is deposited in a narrow region and homogeneous displacements are formed in a shallow region near the surface. The cluster impinges into the substrate keeping the incident atoms aggregated and amorphized, and rod-like damage is formed. The lifetime of the aggregated status of the cluster becomes longer with increasing cluster size, so that the rod-like damage formed by C_{60} is found deeper than that of C_{19} . At the end of the rod-like damage zone, the cluster breaks-up and each fragmented C atom acts in a similar manner to the C monomer. Consequently, interspersed damage is formed in the deeper region of the substrate, similarly to the impact on a diamond, as mentioned in the previous section.

The difference in the damage formation process on the surface according to cluster size is examined. Figure 4.14 shows the time dependence of the number of surface displacements induced by various sizes of clusters. Figure

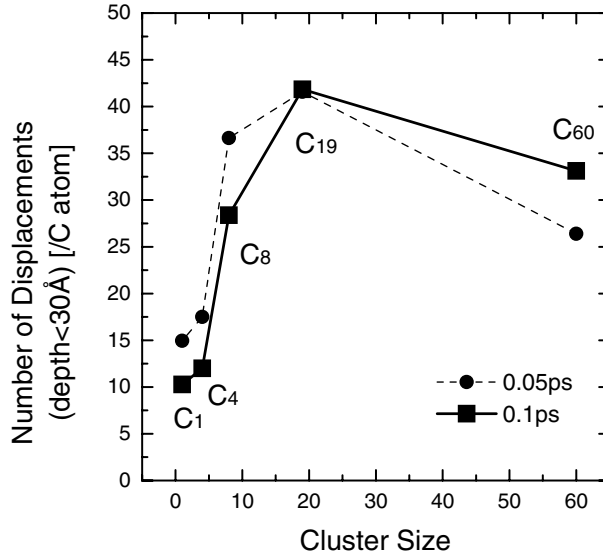


Figure 4.15: Size dependence of the number of displacements on the surface at 0.05ps and 0.1ps after the impact.

4.15 shows the number of surface displacements as a function of cluster size at the time of 0.05ps and 0.1ps after impact. Surface damage is defined as displaced atoms which reside less than 30Å below the surface level. Figures 4.14 and 4.15 show the damage yield induced by 1 carbon atom which was obtained by dividing the total number of surface displacements by cluster size. In figure 4.14, both C₁ and C₄ show the same increasing then decreasing behavior. However, the C₈, C₁₉ and C₆₀ clusters show a larger number of displacements and different dynamics of damage formation than that by smaller cluster. This result implies that a cluster with a threshold size around 10 shows different impact and damage formation processes from monomer ion.

4.4.2 Overlapping Model for Damage Formation by Small Cluster Impact

The size dependence on the surface damage formation is explained by the ‘overlapping damage formation model’⁶⁴⁾ as shown in figure 4.16. When a monomer ion collides with the surface, the incident atom excites the atoms

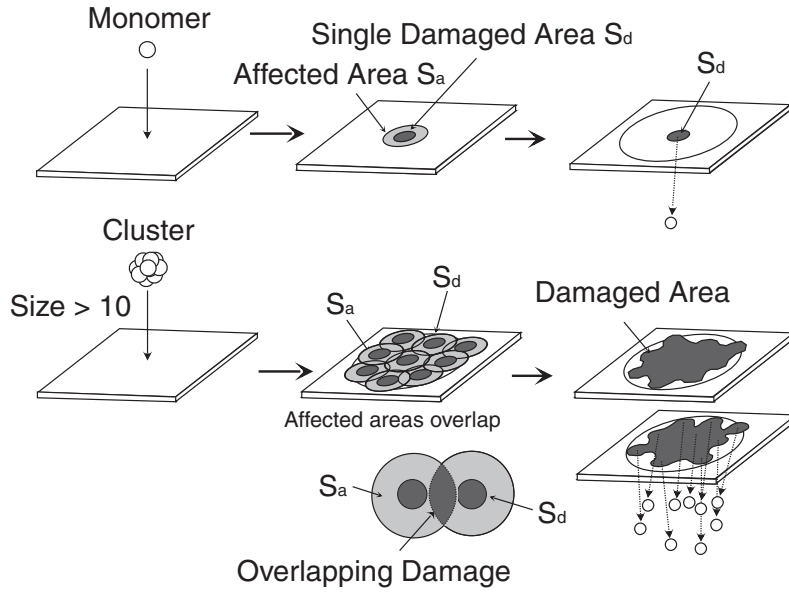


Figure 4.16: Schematic of the 'overlapping model' to explain nonlinear damage formation effect by cluster impact.

in an area (S_a). After the incident atom goes through the first layer, excited atoms in S_a lose their energy and the rim of S_a is not damaged. Finally, the only damage remaining in each S_a is represented by S_d . This assumption is supported by the result shown in figure 4.14 that the number of surface displacements caused by C_1 impact first increases and then decreases towards the end.

When a small cluster ion, such as C_4 , collides with the surface, the cluster breaks-up and each constituent atom in the cluster is scattered. In this case, each S_a area is isolated and only the S_d area remains on the surface. Therefore, the total number of surface displacements atoms equals $S_d \times N$ (where N is cluster size), that is, damage yield per incident atom is the same as that of monomer ion.

When the cluster size increases to as much as 8, the density of incident atoms increases and the affected areas S_a start to overlap with each other. The overlapped area is more excited and remains as damage. This 'overlapped damage' contributes to enhance the yield of surface damage.

In the case of C_8 impact, the number of displacements shows the maximum value of 40 atoms per carbon-atom at the time of 0.06ps and then decreases. However, as the cluster size increases, the decay ratio of the damage decreases because of the increase in overlapped area.

In the case of C_{60} , the number of displacements increases monotonically and converges to 32 atoms per carbon-atom at the time of 0.2ps after the impact. This result means that almost of all S_a areas overlap each other and the impact region is considered to be completely amorphized. The cluster size in which the overlap effect becomes valid depends on the incident energy of the cluster ions. Perez et al. have reported that there is a significant difference in damage formation in the shallow region even between C_1 and C_2 when both are accelerated to about 1MeV/atom⁵⁹⁾. This is because large damaged and affected regions are formed on the surface by such a high-energy ion so that overlapped damage is formed from only two atoms. As the incident energy decreases to as low as a few keV/atom, the affected regions shrink and some incident events are needed to form overlapped damage.

4.4.3 STM Observation of the Damage Formation by Cluster Ion Impact

In order to examine the nonlinear effect in surface damage formation by cluster ions experimentally, STM observations of HOPG surfaces irradiated with various sizes of cluster ion were performed. Figure 4.17 shows STM images of HOPG surfaces irradiated by C_4 , C_7 , C_{19} and C_{60} accelerated with 5keV/atom. Small hills with diameter of about 50Å were observed on the surface irradiated by C_4 or C_7 . Large hills with diameter of 100-150Å were observed on the surfaces irradiated by C_{19} or C_{60} . A large difference was observed between cluster sizes 7 and 19. This indicates that in the case of a size above 19 the mechanism of trace formation is different from that formed by small carbon cluster with a size less than 7.

The dependence of the trace area on the cluster size is shown in figure 4.18 The carbon cluster was accelerated to $V_a=5\text{keV/atom}$ or $V_a=10\text{keV/atom}$. The trace areas are proportional to the cluster size up to 10 for

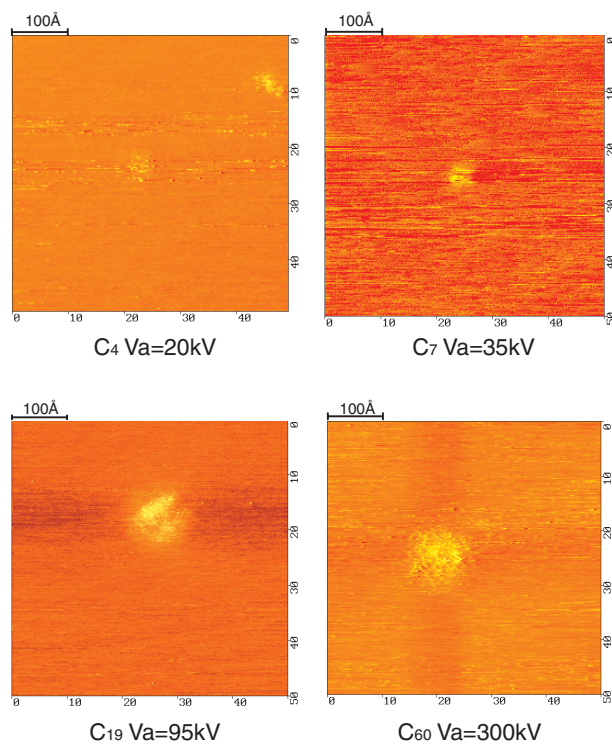


Figure 4.17: STM images of HOPG substrate irradiated with various sizes of carbon clusters. Each cluster is accelerated with 5keV/atom.

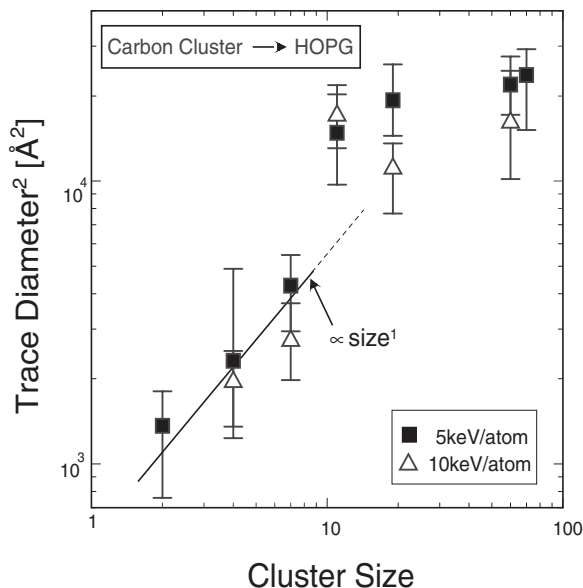


Figure 4.18: Cluster size dependence of the trace area on HOPG surface, measured by STM.

both energies, and increase suddenly for cluster sizes above 10 atoms. These experimental results are in good agreement with the result of MD simulation and damage formation model as shown in figure 4.17.

4.5 Summary

The energy and cluster size dependence of the irradiation effect of a small cluster ion impact was studied by Molecular Dynamics. These results in this chapter are summarized as follows:

1. C_{60} ions with kinetic energy from 100eV/atom to 1keV/atom show deeper penetration than C_1 with the same energy per atom because of the clearing-way (CW) effect. The penetration depth of C_{60} is proportional to the cube root of the energy because of the multiple-collision (MC) effect. This result suggests that C_{60} can be considered as a cluster and its interaction dynamics is similar to that of a large Ar cluster.

2. The stopping power (SP) of C_{60} was found to change dynamically according to the initial impact energy of the cluster. In the initial stage of impact, the CW effect is the dominant process because of the high coherency of the momentum and the kinetic energy of the cluster atoms, and the SP decreases compared to that of monomer ion. Later, implanted cluster atoms disperse into the target in isotropic direction from the impact point due to the MC effect, and the SP increases. For the kinetic energies ranging from 200eV/atom to 2keV/atom, the SP is enhanced by the MC effect. In this energy range, most of the cluster atoms are implanted into the target and many collisions occur to scatter the incident atoms in isotropic direction effectively.
3. The MD simulation and experiments of C_{60} irradiation showed that a C_{60} impact gives 4 to 7 times higher damage formation yield compared with monomer carbon with the same incident energy per atom, at the energy ranging from several hundreds eV/atom to several keV/atom. This energy range is wider than that in which the penetration depth of C_{60} shows the nonlinear effect. At the incident energy of several keV/atom, each cluster atom implants into the substrate independently so that the penetration depth of cluster atoms shows similar to that of monomer ions. However, the cluster atoms cause a large number high-energy substrate atoms with high density at the near surface region and these energetic surface atoms contribute to form a larger number of displacements on the surface.
4. Cluster-size dependence of the impact process of small carbon clusters on carbon substrate was investigated using molecular dynamics simulations and STM observation of HOPG surface irradiated with small carbon clusters. When the cluster size is less than about 10 and the energy is several keV per atom, each cluster atom acts independently and the damage formed in similar way to that from a monomer ion with the same energy-per-atom. On the other hand, a carbon cluster, with a size larger than 10, induces several times larger damage on the surface as compared to a monomer ion.

5. The ‘overlapping model’ is proposed to explain these nonlinear effects in damage formation by small cluster ion impact. The model agrees with the MD results of the time dependence and number of displacements, and also with the STM observations of the HOPG substrate irradiated with various sizes of carbon cluster ions.

Chapter 5

Shallow Implantation by Boron Cluster Ions

5.1 Introduction

As the scale of LSI device decreases, the formation of high-quality shallow p-type junction becomes more important. In order to fabricate a sub- $0.1\mu\text{m}$ p-MOS device, boron atoms are expected to be implanted with less than 1keV ^{65, 66}). However, as the energy of implant energy decreases, it becomes more difficult to obtain enough current for industrial fabrication because of the space charge effect ⁶⁷). Furthermore, the transient enhanced diffusion (TED) of dopant boron atoms becomes a serious problem as the incident energy decreases ⁶⁸).

The boron cluster ion implantation technique using decaborane ($\text{B}_{10}\text{H}_{14}$) has been proposed as one solution for shallow junction formation ^{21, 22}). It has been experimentally observed that the implant range of B atoms using the $\text{B}_{10}\text{H}_{14}$ ion implantation is equivalent to that of monomer B ions accelerated with $1/10$ of the energy of $\text{B}_{10}\text{H}_{14}$ ²²). $\text{B}_{10}\text{H}_{14}$ implantation has great advantages in shallow junction formation because no extra acceleration and deceleration system is needed and charging of the wafer, which causes destruction of devices, is reduced to one tenth of that with monomer ion implantation.

There are other advantages: cluster ion implantation is expected to have a nonlinear effect caused by the high-density irradiation of incident atoms. Considering the irradiation effect of argon and carbon cluster described in chapters 3 and 4, $\text{B}_{10}\text{H}_{14}$ should be considered as a material on the border

between cluster and monomer. Therefore, it is important to examine the similarity and differences between $B_{10}H_{14}$ and B_1 ion implantation.

In this chapter, MD simulations of small boron cluster with the size less than 10, and boron monomer implantation into Si(001) substrate were performed. The dependencies of the implant depth, implant efficiency and damage formation on the size and structure of clusters are examined and the advantages of cluster ion implantation technique are discussed.

5.2 Simulation Model

In order to examine the implant process of small boron clusters, the MD simulations of B_1 , B_2 , B_4 and B_{10} monomer/cluster impacting on a Si(001) substrate are performed. The Stillinger-Weber potential model shown in eqn. (2.15)–(2.17) and table 2.1 is applied to the inter-atomic potential of Si–Si. On the other hand, the ZBL model given by eqn. (2.9)–(2.12) is applied to B–B and B–Si. The cut-off radius for B–B and B–Si under the ZBL model is set at 1.8\AA and 2.08\AA , respectively. A Si(001) substrate is prepared as a target material, which consists of 32768 atoms with a cube side of about 90\AA and is applied with the boundary conditions shown in figure 2.4. Before implantation of the B monomer/cluster, the substrate is heated to 300K in the manner described in section 3.2.

In this work, B_1 , B_2 , B_4 and B_{10} are radiated on the Si substrate with the incident energy of 230eV/atom. As for B_2 , B_4 and B_{10} impact, these clusters are radiated with different geometries as shown in figure 5.1. The reason for this is that, as the cluster size decreases, the structure and orientation of the cluster at impact becomes more significant, whereas large clusters have a spherical structure and no dependency of orientation. In the case of B_4 , two cluster structures were considered; one has a square structure and the other a chain structure, and each B_4 cluster impacts in parallel and perpendicular directions to the Si surface. A B_{10} cluster is implanted as either a horizontal chain, a vertical chain or a spherical f.c.c. structure. The distance between the B atoms is 1.8\AA for each structure, as calculated from the atomic radius of a boron atom.

B_1 monomer and vertical B_2 , B_4 and B_{10} chains are implanted with

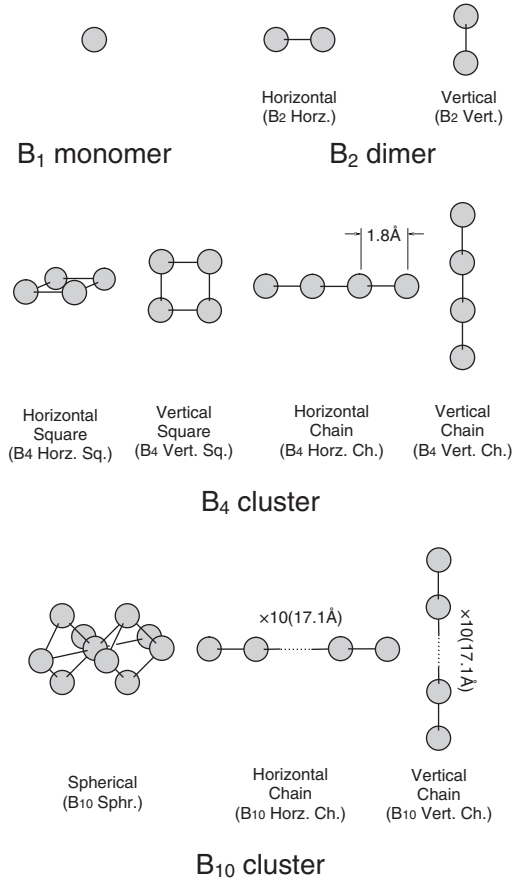


Figure 5.1: Structures and orientations at impact of B_1 , B_2 , B_4 and B_{10} prepared for MD simulation.

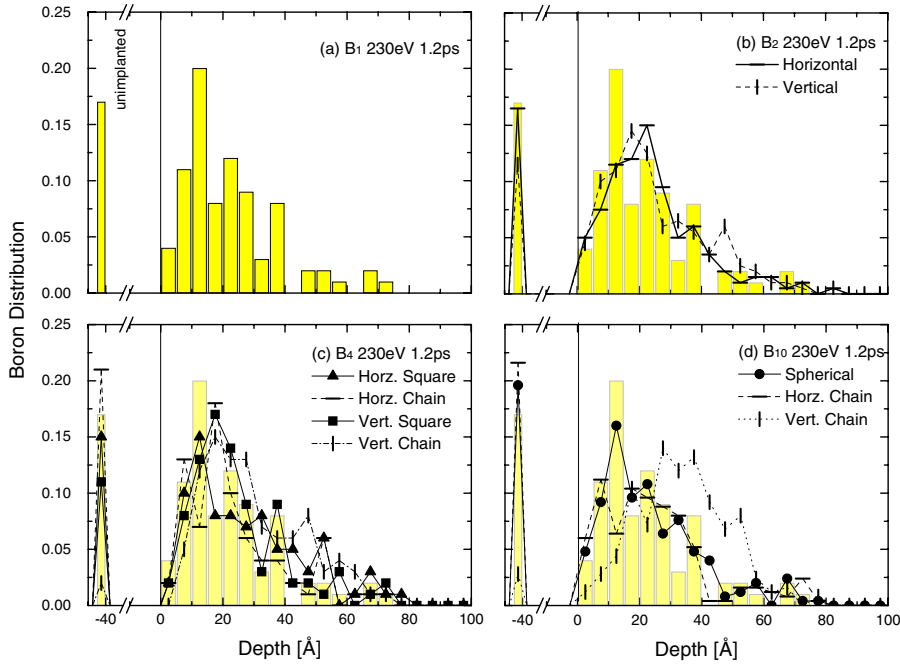



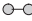
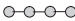



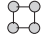




Figure 5.2: Implant profile and efficiency of B atom implantation, by B_1 (a), B_2 (b), B_4 (c) and B_{10} (d). The depth of 0\AA shows the surface of the substrate and the values on the left side indicate the ratio of unimplanted B atoms to total irradiated atoms.

an incident angle of 7° to the surface normal and rotated 30° to the (001) direction to avoid channeling implantation, and other clusters are implanted with normal direction. In order to obtain statistical properties, such as depth profile of implant atoms and displacements, 100 simulations for B_1 and B_2 , and 25 simulations for both B_4 and B_{10} were done at different impact points, respectively.

5.3 Implant Profile and Efficiency

Figure 5.2 shows the depth profile of implanted B atoms from B_1 , B_2 , B_4 and B_{10} impacts, respectively, 1.2ps after impact. In each figure, the region on the RH side where the depth is larger than 0\AA indicates the substrate and the values on the LH side indicate the ratio of unimplanted boron atoms to

Table 5.1: Mean implant depth and implant efficiency of boron cluster.

		Structure of Cluster		Implant Depth [Å]		Implant Efficiency		
Num. of Stacks	B ₁		B ₂		B ₄		B ₁₀	
		<div>18.625 0.83</div>		<div>20.325 0.835</div>		<div>18.25 0.79</div>		<div>18.2 0.784</div>
1						<div>23.125 0.85</div>		
	2			<div>22.287 0.885</div>		<div>21.4 0.89</div>		<div>19.03</div>
	3							<div>0.804</div>
	4						<div>29.025 0.98</div>	
10								<div>32.1</div>
								<div>0.972</div>

the total irradiated atoms. The mean implant depth and implant efficiency for each impact is summarized in table 5.1, where the results are categorized by the properties of cluster; the cluster size and the number of stacked atoms in the perpendicular line to the surface. Each boron atom/cluster is irradiated on the target with the same incident energy of 230eV/atom, so that the total incident energy of B₂, B₄ and B₁₀ are 0.46keV, 0.92keV and 2.3keV, respectively. Figure 5.2 and table 5.1 indicate that, B₂, B₄ and B₁₀ implantation shows the same implant profile and efficiency as B₁, about 82%, except for the case of the vertical B₄ and B₁₀ chains.

In order to understand the enhancement mechanism of implantation depth and efficiency by chain-like cluster impact, the differences in the B implant profile are investigated according to the initial position in the cluster. Figure 5.3 shows the distribution of B atoms implanted by vertical B₁₀ chain, according to the initial position in the cluster. As can be seen, the atoms-1 and -2, which impact on the substrate first, show shallower distribution than atoms-9 and -10, which impact last, and almost all of the

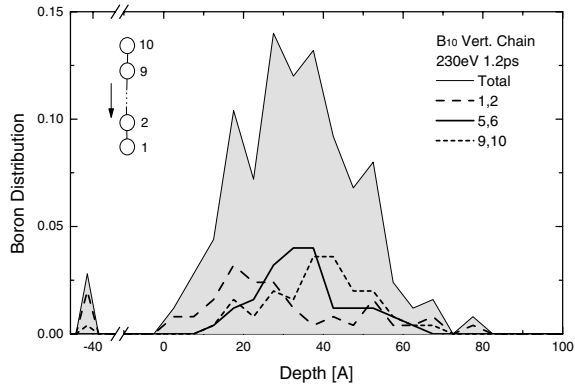


Figure 5.3: Implant profile of B atoms by vertical B_{10} chain cluster according to the initial position in the cluster.

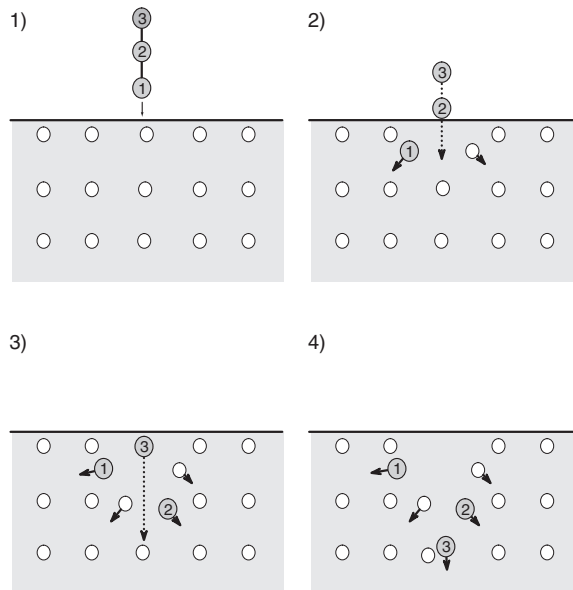


Figure 5.4: Schematic model of the implant process by vertically-stacked B cluster.

backscattered atoms come from atoms-1 and -2. The model of enhancement in implant depth and efficiency by the vertical-chain cluster is shown in figure 5.4, in which the first B atom of a chain cluster knocks-on a substrate Si atom and the following B atoms can penetrate to a deeper region. This collisional process can be considered as the minimum model for the clearing-way effect, which was also shown in argon and carbon cluster impact. Unlike vertical B_4 and B_{10} chain impact, the implant efficiencies of vertical B_2 and vertical square B_4 clusters show a similar value to that of B_1 and horizontal B_4 chain cluster. These results suggest that the stack number of two in B_2 and B_4 square does not have enough density to cause an improvement in implant efficiency, but four is enough for this incident energy of 230eV/atom. This assumption is supported by the spherical B_{10} in which the stack number is two or three and shows similar implant depth and efficiency to that of a horizontal B_{10} chain rather than a vertical B_{10} chain.

As the number of stacks in the cluster increases, the mean implant depth increases. In the case of the vertical B_4 chain cluster impact, the B_4 cluster collapses immediately after it penetrates the first layer of the substrate. However, the B_{10} chain keeps the coherency of velocity in the substrate and each B atom continues to penetrate deeply into the substrate. In these collisional process of small B clusters, the interactions between B atoms are considered to be less probable and each B atom in the cluster acts in a way similar to monomer ions with the same energy per atom. The result of implant efficiency and implant profiles are in agreement with the experimental results from $B_{10}H_{14}$ which has spherical structure and shows the same implant profile as B monomer ions accelerated with 1/10 of the energy of $B_{10}H_{14}$ ²²⁾. These experimental and MD results demonstrate that each B atom in $B_{10}H_{14}$ can be treated as independent B monomer ions.

5.4 Damage Formation by Boron Cluster Impact

5.4.1 Time Evolutions of Damage Formation

Figure 5.5 shows the time dependence of the number of displacements per single B atom. The displacements are defined as these Si atoms which have

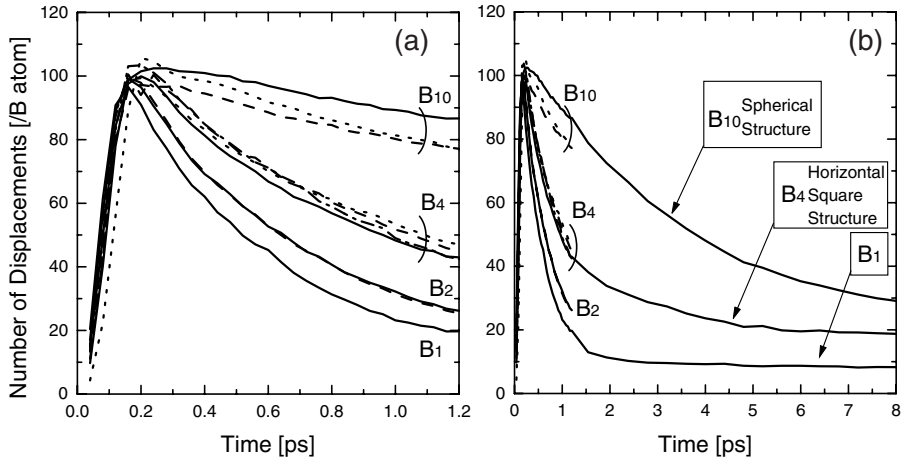


Figure 5.5: Time dependence of the number of displacements per B atom by B clusters with various sizes.

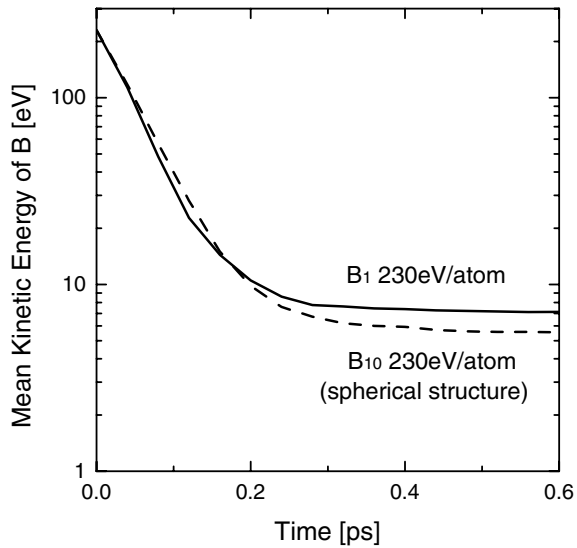


Figure 5.6: Time dependence of the mean kinetic energy of B atom at the impact of B₁ and B₁₀.

a potential energy of 0.4eV above the bulk state⁵³). Figure 5.5(a) shows the transition of the displacement yield by B_1 monomers and various B_2 , B_4 and B_{10} clusters from 0 to 1.2ps. Figure 5.5(b) shows the results from the calculation continued on to 8ps for B_1 , horizontal B_4 square and spherical B_{10} .

Until the time of 0.2ps, almost all of the incident energy from the initial B atoms is transferred to substrate atoms, and the number of displacements reaches the maximum value at around 0.2ps and then decreases. The maximum number of displacements depends neither on cluster size nor on cluster structure. Figure 5.6 shows the time dependence of the mean kinetic energy of B atoms at the impact of B_1 and B_{10} . As can be seen in figure 5.6, the energy transition process of both two shows similar profile. Therefore, it can be considered that each implanted B atom interacts with the substrate atoms individually and the kinetic energy of the incident atoms is transferred to the substrate without overlapping. This suggestion agrees with the aforementioned result that implant profile and implant efficiency do not have size and structure dependency except for the case of the vertical chain cluster.

The damage recovery process takes a longer time than the energy deposition from the projectile to substrate, and is different depending on the cluster size. As shown in figure 5.5(b), the displacements induced by B_1 recover rapidly in 2ps and about eight displacements remain 8ps after impact. However, the damage recovery rate slows down as the cluster size increases. In the case of spherical B_{10} impact, about 30 displacements, which is four times higher than B_1 , remain 8ps after impact. The high yield displacement by cluster ion impact is due to the high-density energy irradiation effect. When a B_{10} cluster impacts the substrate, B_{10} deposits its incident kinetic energy of 2.3keV in a finite region on the surface so that a large number of energetic knocked-on atoms are created. These knocked-on atoms interact with each other, and then these are considered to remain as the deformation of lattice in the substrate. Therefore, the yield of displacement by B_{10} remains several times higher than that of B_1 .

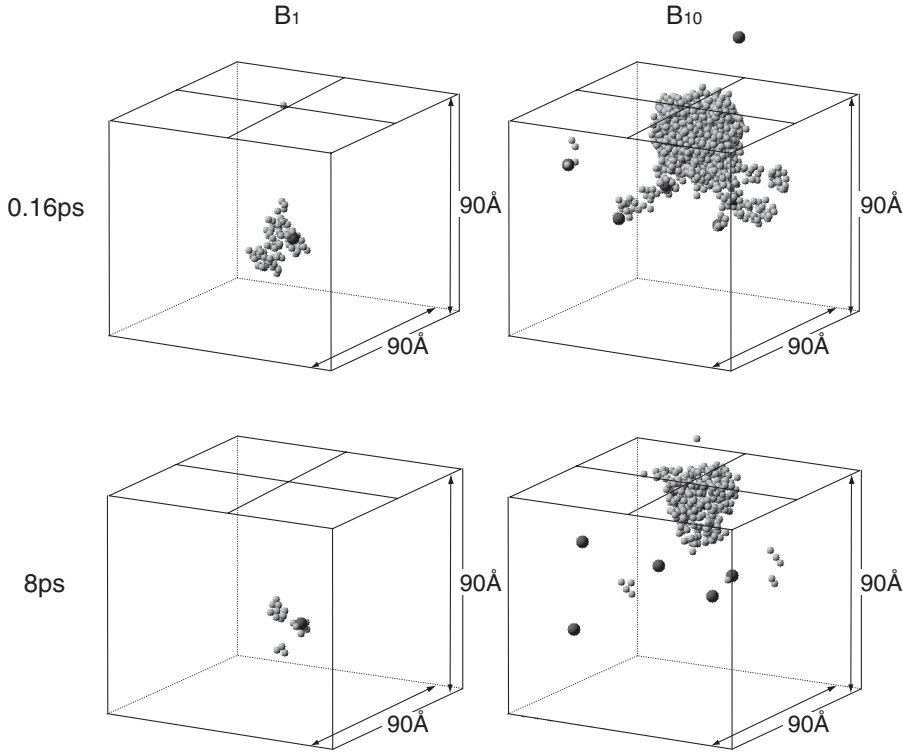


Figure 5.7: Snapshots of B_1 and B_{10} impacting on Si(001) surface, 0.16ps and 8ps after impact.

5.4.2 Depth Profile

Figure 5.7 shows snapshots of B_1 and spherical B_{10} cluster implantation into Si(001) substrate 0.16ps and 8ps after impact. Large black spheres represent the implanted B atoms and gray ones are the displaced Si atoms. Figure 5.8 shows the depth profiles of displacements induced by B_1 , horizontal B_4 and spherical B_{10} cluster. The depth profiles in figure 5.8 are calculated by averaging the results of 50 trials for B_1 and 25 trials for B_4 and B_{10} , respectively.

At 0.16ps after impact, each B monomer and cluster shows a similar profile of damage distribution, like B implant profile and total number of displacements per atom. Figures 5.7 and 5.8 indicate that, at 8ps after impact, a larger number of displacements are formed by B_{10} than by B_1 ,

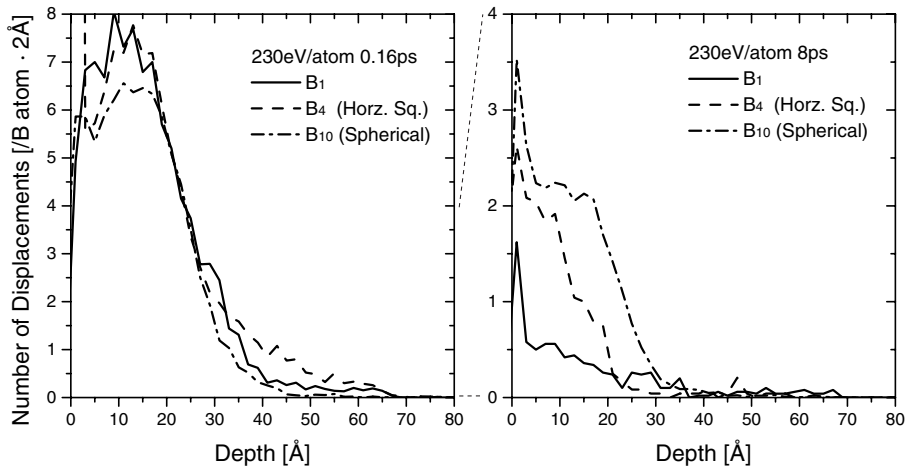


Figure 5.8: Depth profile of displaced Si atoms by the impact of B_1 , B_4 and B_{10} on Si(001) surface, 0.16ps and 8ps after impact.

as indicated in figure 5.5. Furthermore, B monomer and B_{10} clusters show a difference in the distribution of displacements.

In the case of B_1 implantation, transient displacements are formed along the trajectory of incident atom, however, these displacements easily recover because the deposited energy through interaction with incident atom is small. In this case, knocked-on displacements reside around the incident B atom, and this is termed ‘end-of-range’ damage⁶⁹⁾ as shown in figure 5.7. The end-of-range displacements are statistically observed in the region deeper than 30Å in figure 5.8, which shows larger ratio of displacements for B_1 compared to those of B clusters. The end-of-range displacements tend to kick-out the boron atom from a lattice site through annealing and, therefore, the kicked-out B atom diffuses into the deeper region of the substrate. This diffusion mechanism, called ‘Transient Enhanced Diffusion (TED),’ is a serious problem in high-quality shallow junction formation using conventional monomer ion implantation techniques^{68, 69)}.

On the other hand, B_{10} cluster creates a high density of displacements on the surface at the impact point because of the high-density energy irradiation effect. This damaged region is considered to be amorphized and appears as a box-like shape from the surface to a depth of 20Å, which is

comparable with the mean implant depth of the B atoms. This characteristic damage formation by B_{10} is expected to result in significant advantages in shallow junction formation because of reducing TED without pre-amorphization. Through annealing, the reconstruction of a substrate irradiated with B_{10} clusters proceeds from the bottom of the amorphized layer to the surface of the substrate. Therefore, interstitial Si atoms tend to move to the top surface thus avoiding B atom diffusion into deeper regions of the substrate. It has been observed experimentally that low-energy $B_{10}H_{14}$ implantation into a Si substrate does not cause TED^{21, 70)}, similarly to the effect of B monomer implantation into a well pre-amorphized Si substrate.

5.5 Summary

In order to examine the advantages of cluster ion implantation for high-quality shallow junction formation, molecular dynamics simulations of B_1 , B_4 and B_{10} implanting into the Si substrate were performed. The results in this chapter are summarized as follows:

1. B_2 , B_4 and B_{10} provide low-energy ion implantation equivalent to 1/2, 1/4 and 1/10 of the total acceleration energy, respectively. Each B atoms in these clusters show similar implant efficiency and implant profiles to that of B_1 with same acceleration energy per atom, except for the impact of the chain-like structure oriented perpendicular to the substrate. The enhancement of implant efficiency was shown through the impact of vertical chain-like clusters, whose size is larger than four because of coherency of incident velocity.
2. For each case of impact, the number of displaced Si atoms reaches the same maximum value, but decays with different speed. The similarity in the maximum number of displacements is caused by the individuality of the incident B atoms, that is, the kinetic energy of each B atoms is transported to the displacements individually without overlapping. The decay speed is lower as the cluster size is larger because of the high-density energy irradiation effect.

3. In the case of cluster impact such as B_{10} , the impact point is well-amorphized by cluster ion impact and this damage region is expected to stop TED of boron atoms to deeper regions of the substrate. These MD results suggest that the cluster ion implantation technique using $B_{10}H_{14}$ has many advantages for high-quality shallow junction formation through of low-energy implantation and by suppressing TED as a result of high-yield damage formation.

Chapter 6

Reactive Sputtering by Fluorine Cluster Impact

6.1 Introduction

Fluorine is known for its high chemical reactivity and it is well established that fluorine ion irradiation as either ion beam or plasma has much higher yield than non-reactive ions. Furthermore, cluster ion irradiation provides high-density atomic irradiation and high-density energy deposition, which are expected to promote the chemical reaction on the surface.

Figure 6.1 shows the sputtering yield of various target materials at the irradiation by Ar monomer, Ar cluster and SF₆ cluster with total energy of 20keV²⁰⁾ and the predicted sputtering yields by Ar monomer irradiation obtained from the collision cascade theory as the reference⁷¹⁾. For both Ar and SF₆ cluster impact, the mean size is about 2000. Figure 6.1 indicates that, when SF₆ cluster is irradiated on Si and W substrate, the sputtering yield is 10 times higher than that of Ar cluster, which in turn is 10 times higher than monomer ions with the same total acceleration energy.

In order to observe the chemical reaction by SF₆ cluster impact, the evaporated particles during irradiation were measured by quadrupole mass spectrometer (QMS). Figure 6.2(a) shows the mass spectrum after introducing SF₆ cluster beam, and figure 6.2(b) is the spectrum observed during SF₆ cluster irradiation on Si target with the total energy of 20keV. As shown, when the Si substrate is present, a mass peak is observed at 85 amu, which is attributed to SiF₃⁺, the main peak of the SiF₄ spectrum. This result indicates that SF₆ cluster bombardment causes large number

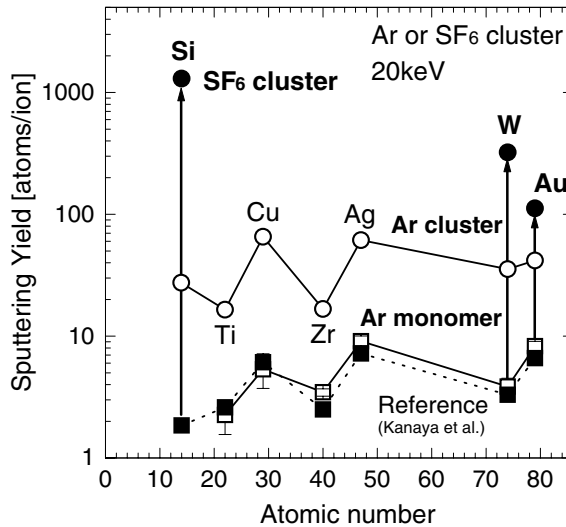


Figure 6.1: Sputtering yield by Ar monomer, Ar cluster and SF₆ cluster impact to various target materials²⁰⁾. The predicted sputtering yields obtained from the collision cascade theory are also shown as the reference⁷¹⁾.

of SiF₄ due to its high chemical reactivity at the impact, and these SiF₄ molecules are ionized and detected as SF₃⁺ at the QMS. At the bombardment of a (SF₆)₂₀₀₀ with total energy of 20keV, each F atom in the cluster has an energy of 1.3eV. However, it causes chemical reaction on the surface and a higher sputtering yield, as shown in figure 6.1. This high-yield etching effect is considered the result of the nonlinear effect by cluster ion impact.

It is important to understand how energetic ions and clusters enhance the sputtering yield, not only from the viewpoint of science but also for industrial applications. In this chapter, MD simulations of fluorine atoms, molecules and clusters impacting on Si(001) and Si mono-fluoride (001) surfaces were performed. The sputtering yield and the sputtered species are compared with those formed by a neon gas cluster, which has similar atomic weight but no chemical reactivity with Si.

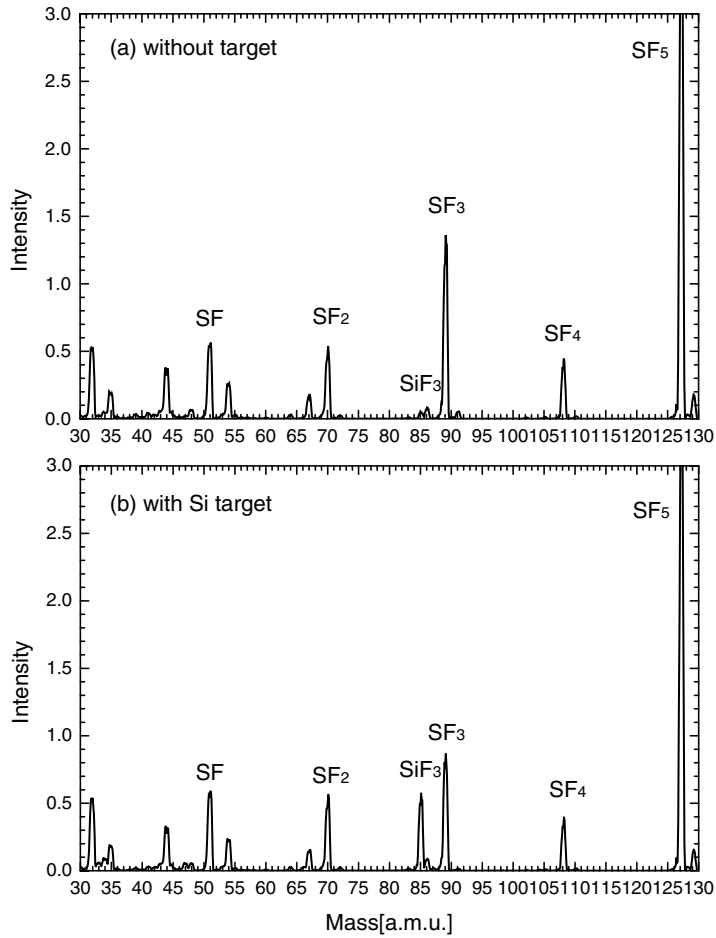


Figure 6.2: QMS mass spectra of the particles after introducing SF_6 cluster beam in the chamber (upper:a), and during SF_6 cluster irradiation on Si target (lower:b). SF_6 cluster is accelerated with the total energy of 20keV.

6.2 Simulation Model

Potential Model

In this work, MD simulations of F_1 , F_2 , $(F_2)_{30}$, Ne_1 and Ne_{60} molecule/dimer/cluster impacting on a Si(001) and a Si mono-fluoride(001) (Si-F(001)) surfaces were performed. In order to describe the interactions between Si and F atoms, the Stillinger–Weber (SW) type potential model was applied. The SW type potentials and their parameters are given by eqn. (2.15)–(2.24) and table 2.1 and 2.2. On the other hand, the interactions between Ne–Ne and Si–Ne are described only in Ziegler, Biersack and Littmark (ZBL) universal potential model²⁷⁾ given by eqn. (2.9)–(2.14), because the binding energies of Ne–Ne and Si–Ne are much lower than those of Si–Si, Si–F, F–F and also lower than the incident energy of projectile atoms in this work. The cut-off radius (r_c) of Ne–Ne interaction was set at 3.2Å, which corresponds to the bond length of Ne–Ne. For the Ne–Si interaction, r_c is 2.75Å, which is the mean bond length of Ne–Ne and Si–Si.

Cluster Modeling

The structure of the F_2 cluster has been reported to consist of a central F_2 which is hexagonally surrounded by six neighboring F_2 molecules in a horizontal plane and is considered to be stable³⁹⁾. In this simulation, $(F_2)_{30}$ cluster was constructed by stacking 3 planes of F_2 molecules. Each F_2 plane contains 7, 16 and 7 molecules respectively. The distance between F_2 molecules in the horizontal plane is 3.12Å and the interplanar distance is 4.53Å, which corresponds to the distance between two aligned F_2 molecules giving minimum potential energy. The shape of Ne_{60} cluster is spherical and it has an icosahedral structure. For both fluorine and neon clusters, each atom in the cluster has the same velocity in both magnitude and direction at the beginning of the impact. In this study, all clusters and molecules are irradiated with the energy ranging from 1eV/atom to 100eV/atom.

Substrate Modeling

The Si(001) target substrate consists of maximum 260,000 atoms and its maximum dimension is $180\text{\AA} \times 180\text{\AA} \times 180\text{\AA}$, which is large enough to receive incident energy of this magnitude. The surface Si atoms construct a stable 2×1 structure⁵⁰). A periodic boundary condition and thermal bath is applied to the substrate, as shown in figure 2.4, and the substrate temperature is set at 300K before impact. For comparison, a Si mono-fluoride (001) surface (Si-F(001) surface) was also prepared as the target material. For the Si-F(001) surface, each surface Si atom has a bond with one F atom.

In order to obtain enough statistics, the simulations of $(F_2)_{30}$ (100eV/atom) and Ne_{60} (100eV/atom) were performed 10 times and the others 100 times with different impact points. Each impact process was calculated for 8ps, a time interval which is long enough to finish the impact process and investigate the adsorption and desorption of molecules. The sputtering yield was calculated by dividing the total number of desorbed Si atoms by the total number of irradiated F atoms in a molecule/cluster.

6.3 Penetration and Sticking Mechanism

6.3.1 The Impact Event

Figure 6.3 shows snapshots of $(F_2)_{30}$ cluster impacting on the Si(001) surface with 1eV/atom (60eV total), 10eV/atom (600eV) and 100eV/atom (6keV), respectively. For each impact energy, the side view at 0, 0.15, 1.5 and 8ps after impact, and top view at 8ps are shown. When the acceleration energy is very low, 1eV/atom, the cluster cannot penetrate the surface and collapses on it. During the impact at this low energy, some F_2 molecules in the cluster dissociate to F atoms and some F atoms remain on the surface. The surface structure of Si(001) 2×1 is almost undisturbed and almost all of adsorbed F atoms have a bond with one Si ad-atom on the surface. This result reconfirms the previous observations that fluorine monomer or dimer are adsorbed on a Si(001) 2×1 ^{72, 73}).

As the incident energy increases, the cluster penetrates the surface and a crater-shaped damage occurs on the surface. Most of the F atoms are

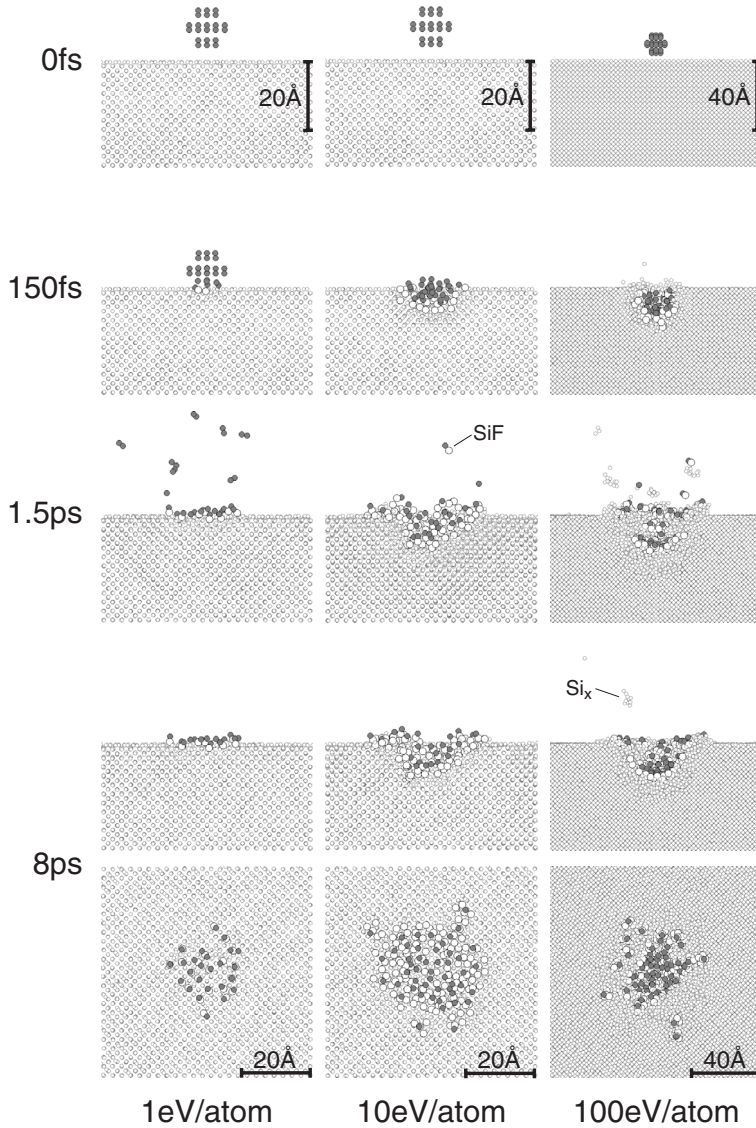


Figure 6.3: Snapshots of $(F_2)_{30}$ cluster impacting on bare Si(001) surface at 1, 10 and 100 eV/atom taken at 0, 0.15, 1.5 and 8 ps after impact as indicated. For 8 ps both side and top view are shown. Gray circle, white circle and large white circle are F, Si and Si atom bonded to F atom, respectively.

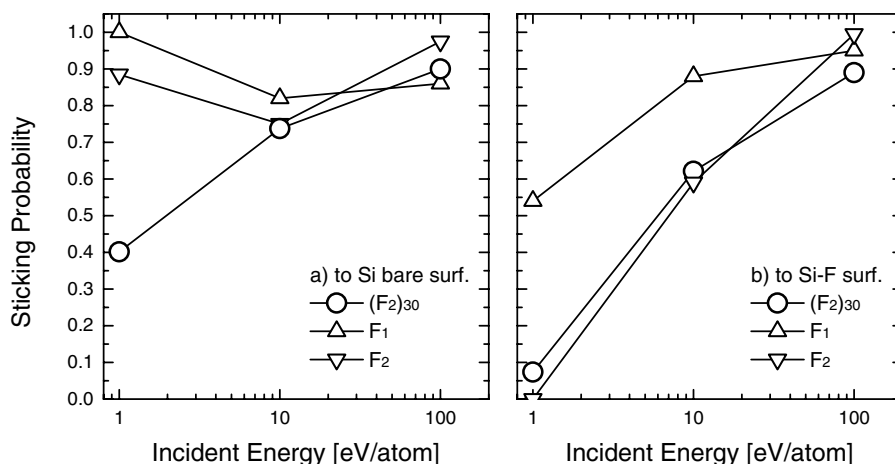


Figure 6.4: Incident energy dependence of the sticking probability of F, F₂ and (F₂)₃₀ to (a) bare Si surface and (b) Si mono-fluoride surface, 8ps after impact.

adsorbed on the wall and the bottom of the crater. The formation of crater-like damage was observed with non-reactive cluster ion impact both by simulations and experimentally as shown in the previous chapters and as also shown by the other groups^{74, 75, 76, 77}. In the case of 10eV/atom, as shown in figure 6.3, one Si atom is sputtered as SiF. When the incident energy is as high as 100eV/atom, a large number of Si atoms are sputtered as a non-fluorine-containing Si cluster, which is significantly different from the result with 10eV/atom.

6.3.2 Sticking Probability

Figures 6.4(a) and 6.4(b) show the energy dependence of the sticking probability of F atoms to a bare Si and a Si-F surface, respectively, at 8ps after impact. When the incident energy is 1eV/atom, almost all of fluorine monomers stick on the bare Si surface and form a stable bond with the surface Si ad-atom. The fluorine dimer also dissociates and both two F atoms adsorb on the bare Si surface. However, the sticking probability of (F₂)₃₀ is much smaller than that of F₁ and F₂; only 40% of incident F atoms are adsorbed on the surface. The diameter of (F₂)₃₀ is about 10Å, which

corresponds to the length of 2 unit cells of silicon. In the case of $(F_2)_{30}$ impact, the F atoms are arriving in such a narrow region, so that some of them cannot interact with surface Si atoms and are expected to leave the surface. As shown in figure 6.3, at the impact with 1eV/atom, F atoms of $(F_2)_{30}$ spread over a square of about $20\text{\AA} \times 20\text{\AA}$ (4 Si unit cell length square) which contains 32 surface ad-atoms and 23 F atoms stick on the surface after 8ps. In this case, many Si-F bonds with high density are formed on the surface. Therefore, the formation of volatile fluoride products such as SiF_4 is prompted and a higher etching rate is expected compared to F monomer or dimer irradiation.

On the other hand, when the Si surface is already covered with F atoms, the sticking probability is low as it is difficult for another F atom to find an F-free site on the surface. In the case of F_2 impact with 1eV/atom, all incident molecules are reflected without dissociation. This result is due to the fact that the bond energy between F-F is 1.66eV⁴⁰⁾ and the F_2 dimer carries 2eV of kinetic energy. A similar result is shown with $(F_2)_{30}$ irradiation; only 2% of incident molecules were dissociated and almost of all are evaporated keeping the F-F bond.

As the incident energy increases, the sticking probability of F_1 and F_2 to bare Si surface first decreases and then increases. When the incident energy is 10eV/atom, some of the incident F atoms are reflected through atomic collisions with surface Si atoms. If the incident energy is 100eV/atom, however, the F atoms can penetrate the surface and most of them are implanted into the substrate. On the other hand, the sticking probability of $(F_2)_{30}$ increases monotonically with the increasing incident energy. At higher energy, $(F_2)_{30}$ can penetrate the surface and the number of Si atoms which interact with F atoms increases. The sticking probability to the Si-F surface also increases as the incident energy increases because of a similar reason to the $(F_2)_{30}$ impact on a bare Si surface. It should also be noted that, at the highest energy, 100eV/atom, the sticking probability for all cases coincide to 1.0, as shown in figure 6.4.

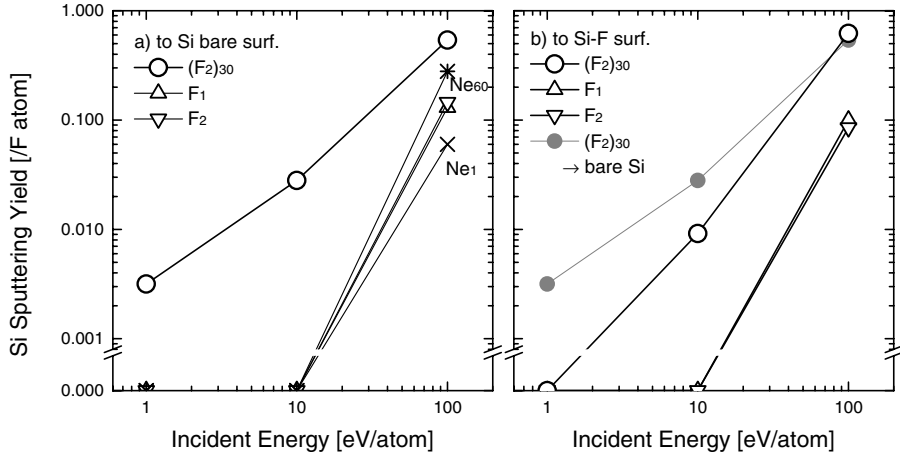


Figure 6.5: Incident energy dependence of the Si sputtering yield of F, F_2 , $(F_2)_{30}$, Ne and Ne_{60} to bare Si surface (left:a), and F, F_2 and $(F_2)_{30}$ to Si mono-fluoride surface (right:b), 8ps after impact.

6.4 Sputtering Effect

6.4.1 Sputtering Yield

Figures 6.5(a) and 6.5(b) show the energy dependence of the sputtering yield of F, F_2 and $(F_2)_{30}$ as well as Ne monomer and Ne_{60} . Figures 6.5(a) and 6.5(b) shows the yield of bare Si and Si-F surfaces, respectively. At 100eV/atom, all incident particles cause sputtering. F_1 and F_2 shows the same sputtering yield per one F atom to both bare Si and Si-F surfaces, which indicates that each F atom in the F_2 molecule interacts with the surface atoms independently, i.e. nonlinear effect does not occur. However, the sputtering yield of $(F_2)_{30}$ is several times higher than F_1 and F_2 . This result suggests that $(F_2)_{30}$ impact causes nonlinear effects in sputtering by high-density particle and energy irradiation.

When a cluster impacts on a substrate with energy high enough to penetrate the surface, the cluster deposits its kinetic energy with high density. Furthermore, high-density atomic irradiation causes a large number of collisions between cluster-cluster, cluster-substrate and substrate-substrate atoms. Because of these multiple collisions, the deposited kinetic energy is

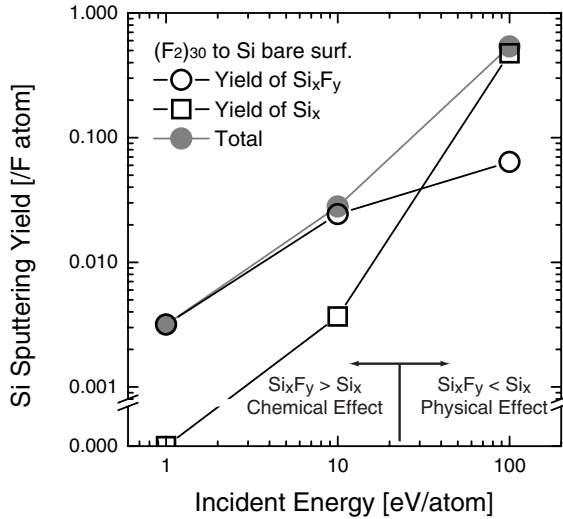


Figure 6.6: Incident energy dependence of the sputtering yield of Si atoms with or without F, at the impact of $(\text{F}_2)_{30}$ on Si(001) surface.

transferred isotropically and the impact point is deformed hemispherically, as shown in figure 6.3 and in other MD simulations of inert gas clusters mentioned in chapter 3 and 4. The nonlinear effect in sputtering is observed in Ne cluster ion impact. In figure 6.5(a), Ne_{60} cluster also shows higher sputtering yield than Ne_1 , like the $(\text{F}_2)_{30}$ cluster.

The difference in sputtering yield between F cluster and F monomer/dimer increases as the incident energy decreases. When the incident energy is below 10 eV/atom, the F monomer and dimer do not cause sputtering but the $(\text{F}_2)_{30}$ cluster shows a relatively high sputtering yield. On the contrary, with 10 eV/atom or less, sputtering is not observed with Ne_{60} accelerated. It is considered that the mechanism of enhancement of sputtering yield by cluster ion is different depending on the incident energy.

6.4.2 Sputtered Species

Figure 6.6 shows the incident energy dependence of the sputtering yield of Si atoms with or without F, at the impact of $(\text{F}_2)_{30}$ on Si(001) surface. Figure 6.6 indicates that, at the low energy impact, almost all of Si atoms

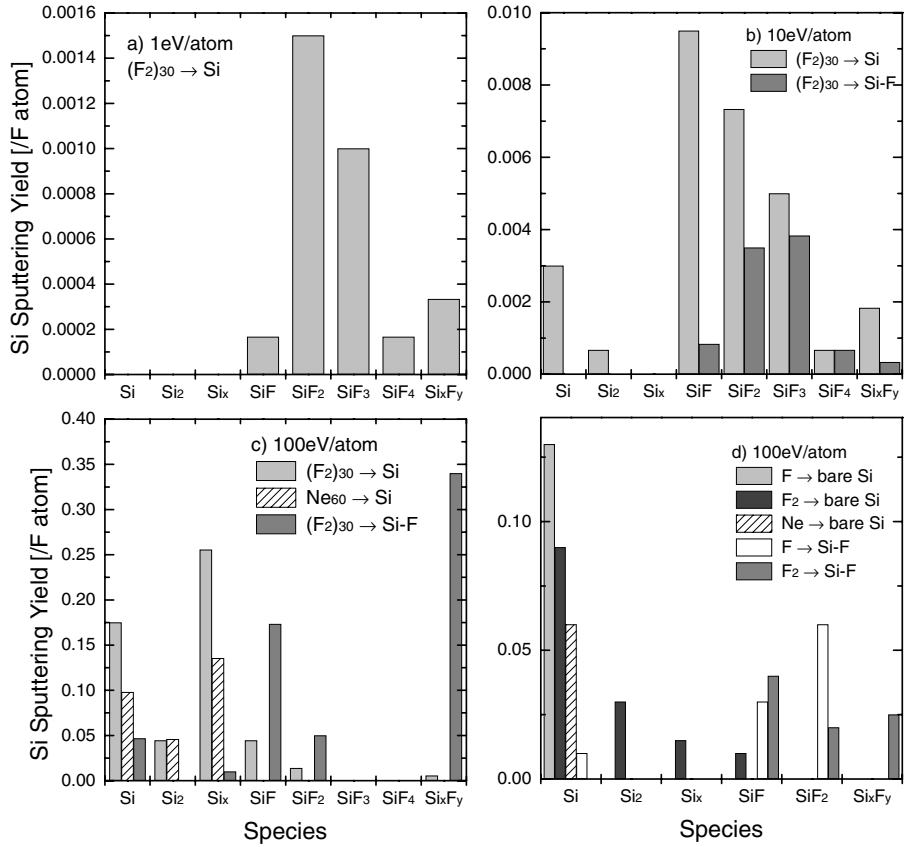


Figure 6.7: Distribution of sputtered species by F cluster with F cluster with 1eV/atom (a), F cluster with 10eV/atom (b), F and Ne cluster with 100eV/atom (c) and F monomer, dimer and Ne monomer with 100eV/atom (d).

are sputtered as a fluorized compound, however, as the incident energy increases, most of Si atoms are sputtered without bonding to F atoms. It can be considered that the major effect to dominate the sputtering mechanism by fluorine cluster will vary according to the incident energy of the cluster.

Figures 6.7(a)~(d) show the distribution of sputtered molecules by impacts of various atom/molecules. The major sputtered product by F cluster impact on a bare Si surface is different with varying incident energy. At 100eV/atom, the major sputtered products by $(F_2)_{30}$ are Si clusters with no fluorine, whereas Si monomer is the main product with F and F_2 irradiation. This tendency is shown also for Ne cluster and Ne monomer with 100eV/atom. It has been shown in figure 3.17 that, when crater-shaped damage is formed by a cluster impact, the surface atoms move in lateral direction and form the rim of a crater. In this collisional process, these surface atoms on the rim have the same kinetic energy and momentum, so that some atoms in rim of crater leave the surface as a cluster, which is termed as 'lateral sputtering.' Therefore, the mechanism of high-yield sputtering with high-energy (100eV/atom) cluster impact can be considered to be mainly a physical atomic collisional process.

As the incident energy decreases, the major sputtered products change to silicon fluorides with more F atoms, i.e. they are more volatile molecules. Considering that F_1 , F_2 and Ne_{60} do not cause sputtering with an energy below 10eV/atom, the high-yield sputtering effect with low-energy (10eV/atom or less) depends on the chemical reactivity due to the high-density atomic irradiation by the cluster impact, which causes high-density Si-F precursors on the surface.

When the incident energy is 100eV/atom, the sputtering yield of fluorine monomer, dimer or cluster on a Si-F surface is similar to that on a bare Si surface, but the sputtered products are different; the major products are SiF_2 , SiF and Si cluster containing some F atoms for F_1 , F_2 and $(F_2)_{30}$, respectively. In any case, considering the sticking probability, almost all of the F atoms in the sputtered particle are considered to be the atoms adsorbed on the surface before impact, as shown in figure 6.4. Therefore, chemical reactivity is not an important factor in bombarding with 100eV/atom particles onto a Si-F surface.

As shown in figure 6.5(b), the sputtering yield of a Si-F surface is lower than that of bare Si at 10eV/atom. At the lowest impact energy for which results were obtained, 1eV/atom, no sputtering occurs. The distribution of sputtered products from a $(F_2)_{30}$ cluster with 10eV/atom to bare Si and Si-F surface are shown in figure 6.7(b). Irradiation onto a Si-F surface does not produce non-fluorine-bonded Si as the sputtered particle. If the incident energy is low, the surface potential barrier has a decisive role in the impact process regarding the sputtering yield. The surface potential barrier of a Si-F surface is higher than that of the bare Si surface, so that the cluster is reflected on the surface without depositing kinetic energy.

6.4.3 High Performance Etching by Reactive Cluster Ion

Figure 6.8 shows the depth profile of displaced Si atoms at the impact of F_1 , F_2 and $(F_2)_{30}$ on a Si(001) surface with various incident energies, 8ps after impact. The displacements are defined atoms which gained 0.4eV of the potential energy above the bulk state. At any incident energy, $(F_2)_{30}$ cluster impact shows larger damage formation yield and deeper profile of displacements compared with F_1 and F_2 . This is because a $(F_2)_{30}$ cluster can penetrate to a deeper region due to the clearing-way effect and deposit its kinetic energy in narrow region, similar to the C_{60} impact mentioned in chapter 4.

The relationship between the yield of sputtering and damage formation in the substrate was examined. Figure 6.9 shows the relationship between the mean damage depth and the sputtering yield by F_1 , F_2 and $(F_2)_{30}$ impact. As can be seen in figure 6.9, $(F_2)_{30}$ impact shows higher sputtering yield but forms shallower damage distribution compared with F_1 and F_2 . These results indicate that the low-energy cluster ion impact enhances the chemical reactivity on the surface and high-yield and low-damage sputtering effect can be achieved.

6.5 Summary

In this chapter, MD simulations of fluorine atom, molecule and cluster impacts on a bare silicon and silicon-fluoride (Si-F) surface were performed

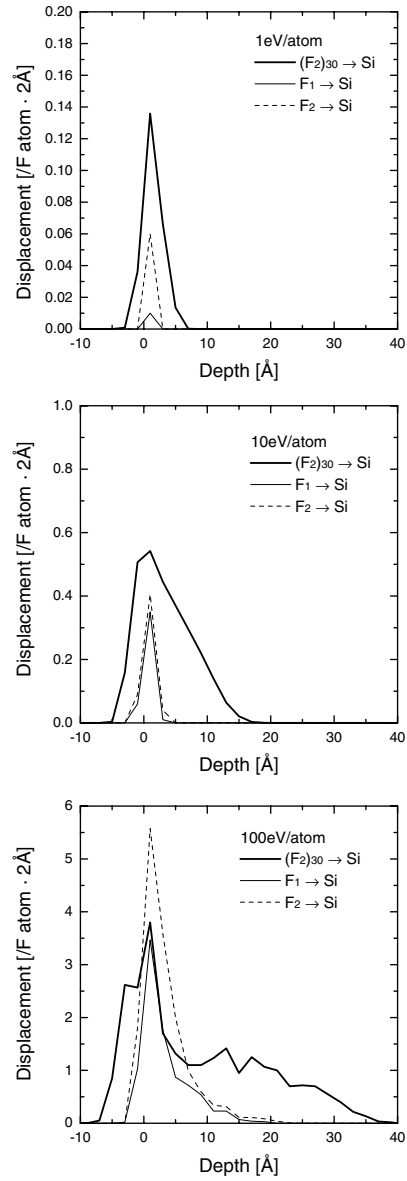


Figure 6.8: Depth profile of displaced Si atoms at the impact of F_1 , F_2 and $(F_2)_{30}$ with various energies, 8ps after impact.

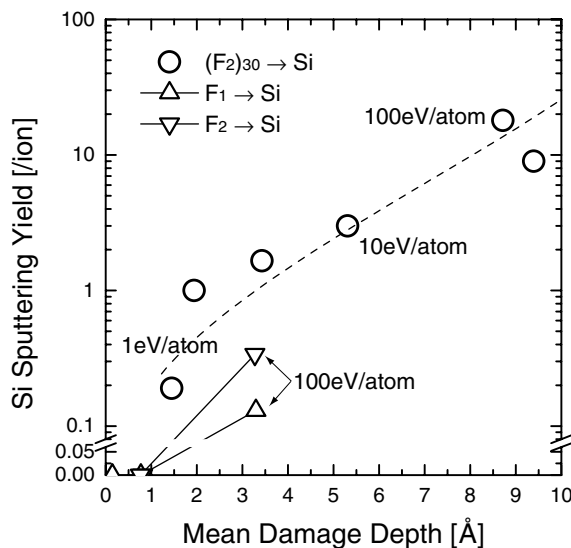


Figure 6.9: Relationship between the mean damage depth and the sputtering yield by F_1 , F_2 and $(F_2)_{30}$ impact.

to elucidate the mechanism of silicon sputtering by fluorine clusters. the results in this chapter are summarized as follows:

1. A $(F_2)_{30}$ cluster impact on a bare Si surface shows sputtering even at the low incident energy of 1eV/atom, whereas F and F_2 only adsorb on the surface at this energy and sputtering does not occur. For cluster impact, Si atoms desorb from the surface as silicon fluoride, which means that chemical sputtering occurs.
2. The effect of the chemical enhancement by cluster impact is due to the fact that the cluster impact brings many atoms into a very narrow region and this causes a large number of Si-F precursors to be formed. Moreover, the kinetic energy of the cluster is deposited with high density and precursors are excited and prompted to create SiF_x species.
3. With increasing incident energy the sputtering yield increases, but the ratio of fluoride particles to the total sputtered particles decreases. At an incident energy of 100eV/atom, Si atoms are sputtered as silicon

cluster without fluorine, in a sputtering mechanism similar to that of the Ne_{60} cluster. This indicates that the sputtering with high energy is preceded by a physical effect through a large number of atomic collisions.

4. The sputtering yield and sticking probability to the bare Si and Si-F surfaces are similar for an incident energy of 100eV/atom. However, if the incident energy is less than 10eV/atom, the sputtering yield of the Si-F surface is significantly lower than that of bare Si. This is attributed to a surface potential barrier which prevents the formation of SiF_x species.
5. $(\text{F}_2)_{30}$ impact causes larger and deeper damaged region compared with F_1 and F_2 impact with the same incident energy per atom. However, from the view point of total sputtering yield and damage depth, the cluster impact provides a higher sputtering yield than monomer and dimer impact which cause the same mean damage depth as the cluster. This result demonstrates that the reactive cluster impact can achieve high-yield and low-damage etching.

Chapter 7

Summary and Conclusions

In this work, the impact processes of cluster ions on solid surface were studied by use of molecular dynamics (MD) simulation. It was demonstrated both in MD simulations and in experiments, that cluster ion causes an interesting collisional process at the impact with a solid target, which cannot be explained by summation of single ion effects and is called ‘non-linear collisional process.’ The nonlinear effects caused by cluster impact are summarized as following.

In chapter 3 and 4, the basic impact processes of cluster ions were discussed using large argon clusters, which consist of several tens to thousand atoms, and small carbon clusters, such as C_4 , C_8 , and C_{60} . In order to explain the collisional process of cluster ion, two effects, the ‘clearing-way’ and the ‘multiple-collision’ effects, are proposed. The ‘clearing-way’ effect occurs with the following mechanism: At the impact of a cluster ion, a large number of cluster atoms are irradiated in a narrow region. In this collisional process, the surface atoms are pushed aside from their original site by the first cluster atoms to hit the surface and the next following cluster atoms penetrate the surface without energy loss. Thus, the cluster can penetrate into the substrate deeper than a monomer ion with the same energy per atom.

On the other hand, implanted cluster atoms collide with a large number of surrounding substrate atoms, which in turn also cause many collisions with other substrate atoms as well as cluster atoms. Because of this ‘multiple-collision’ effect, cluster atoms spread isotropically rather than penetrate to a deeper region in the substrate, so that the mean penetra-

tion depth of cluster is shallower than that of monomer ion with the same total acceleration energy. In the multiple-collision process of cluster ion, the homogeneous damaged region with the shape of crater is formed on the surface. These penetration and damage formation processes are very different from the cascade-collision processes, which occur with monomer ion impact.

Nonlinearity in the penetration depth occurs with the incident energy ranging from several tens to several hundreds eV/atom for Ar cluster on Si substrate impact, and from about one hundred to several thousands keV/atom for C_{60} on diamond substrate. In these energy regimes, the mean penetration depth of cluster atoms and the radius of the crater formed on the surface are proportional to the cubic root of the incident energy. This is because, in the multiple-collision process, the incident energy and momentum are transferred isotropically and the cluster atoms expand hemispherically in the substrate. If the whole incident energy of the cluster is deposited onto the substrate to form displacements, the volume of the displaced region will correspond to the incident energy. Thus, if the shape of the displaced region keeps a similar aspect ratio at any incident energy, it is considered that the penetration depth as well as the radius and the depth of crater obey a cubic-root law.

At low energy impact, with less than the lower threshold energy to show the cubic-root law, the cluster does not penetrate even with the help of the clearing-way effect and it collapses on the surface. On the other hand, if the incident energy is above the higher threshold, cross-section of impact decreases, so that the incident atoms of the cluster are implanted into the substrate independently and do not cause the multiple-collision effect, and the penetration depth approaches that of monomer ions for the same incident energy per atom.

As for the damage formation by cluster impact, the energy range in which the nonlinear effect occurs extends to the cases in which penetration depth does not obey the cubic-root law. In the kinetic energy regime in which the penetration depth obeys the cubic-root law, the energy of cluster is deposited in shallower region compared with the monomer ion with the same total acceleration energy. In addition, because of the multiple-

collisions effect, the kinetic energy of the cluster is transferred homogeneously to the substrate atoms near the impact site by a collective movement. Consequently, a large amorphized crater-shaped damage is formed on the surface.

As the incident energy increases and the multiple-collision effect decreases, each cluster atoms impinges into the substrate independently, but produces a large number of high energy target atoms near the surface region with high density. These high-energy substrate atoms cause a multiple-collision effect in a similar manner to the cluster atoms in the middle range of the kinetic energy. In the case of high energy impact, cluster ion irradiation provides a similar penetration depth, but several times higher displacement yield compared with monomer ion with the same acceleration energy per atom.

The size-dependence of the damage formation under high-energy cluster impact was examined using small carbon clusters ranging from the size 1 to 60. At the incident energy of 2keV/atom, in which these clusters show a similar implant depth to carbon monomer, the damage typical to the cascade-collision mechanism is formed with the size of less than 8, whereas C₁₉ and C₆₀ impacts show homogeneously damaged regions in the surface of the substrate. These results indicate that the threshold cluster-size to cause the nonlinear effect in damage formation is around 10.

In chapter 5, MD simulations of small B cluster and monomer implantation were performed, and the characteristics and advantages of cluster ion implantation were discussed. B₁, B₂, B₄ and B₁₀ are irradiated on Si (001) substrates with acceleration energy of several hundreds eV/atom. In this simulation, the dependence of cluster size and structure on the impact process were examined. It was shown that, in each cluster impact, implant depth and implant efficiency similar to monomer ions were obtained, except for vertical chain-like cluster with the size larger than 4. In this exceptional case, deeper implant depth and higher implant efficiency were observed. The latter can be explained by the following mechanism: The atom which impacts on the substrate first clears the substrate atom and resides in a shallower region in the substrate than the atoms following, which will penetrate the substrate without energy loss like in the clearing-way

effect. This result suggests that each B atom in a B cluster acts like a monomer ion.

Nonlinearity is shown in damage formation similar to that observed for carbon cluster impact. The number of displacements produced by one B atom once increases to the same maximum for both B cluster and B monomer. However, the damage recovery process is different, depending on cluster size. Damage induced by B_{10} recovers more slowly, with 4 times more displacements remaining, compared to B_1 . These displacements by B_{10} clusters concentrate in the near surface region of the impact point, while those by B_1 reside around the implanted B atom as end-of-range damage. This characteristic damage formation by B_{10} cluster is expected to avoid transient-enhanced-diffusion of incident B atoms and achieve the formation of high-quality shallow p-type junction.

In chapter 6, MD simulations of fluorine atoms, molecules and clusters impacting a silicon substrate were performed in order to investigate the impact process of a reactive cluster ion. The results show that when the incident energy of the impacting fluorine atom or molecule is below 10eV/atom, the species are only adsorbed on the surface and sputtering of substrate atoms does not occur. On the other hand, a fluorine cluster consisting of 30 molecules produces sputtering even at a low incident energy of 1eV/atom. At these conditions, the surface atoms are desorbed as fluorine-containing species, such as SiF or SiF₂, indicating that chemical desorption is enhanced by irradiation with fluorine clusters.

As the incident energy of the cluster increases to values as high as 100eV/atom, almost all the fluorine atoms penetrate the surface and a crater-shaped damage is formed. The incident F atoms reside at the bottom region of the crater. In this case, silicon atoms leave the surface as monomers, dimers or clusters without F atoms, i.e. physical sputtering through atomic collisions has a higher probability than chemical reactions in this energy regime, like in the case of Ne or Ar cluster impact.

$(F_2)_{30}$ impact causes larger and deeper damaged region compared with F_1 and F_2 impact with the same incident energy per atom. However, from the view point of total sputtering yield and damage depth, the cluster impact provides higher sputtering yield than monomer and dimer impacts

which cause the same mean damage depth as the cluster. This result demonstrates reactive cluster impact can be used for the high-yield but low-damage etching process.

In this work, the nonlinear characteristics of cluster ions were clarified for varying incident energy, cluster size and species. It is expected that, by proper selection of cluster size, species and energy, new nano-scale processes such as shallow junction implantation, high-yield sputtering and surface modification could be developed.

References

- [1] I. Newton, *Prinpicia*, 1685.
- [2] H. Goldstein, *Classical Mechanics*, 5 ed. (Addison-Wesley Publishing Company Inc., Massachusetts U.S.A., 1957).
- [3] H. Geiger and E. Marsde, Phil. Mag. **25** (1913) 606.
- [4] E. Rutherford, Phil. Mag. **21** (1911) 669.
- [5] N. Bohr, K. Dan. Vidensk. Selsk. Mat. Fys. Medd. **18** (1948) 8.
- [6] L. H. Thomas, Proc. Cambridge Philos. Soc. **23** (1927) 542.
- [7] E. Fermi, Z. Phys. **48** (1928) 73.
- [8] O. B. Firsov, Zh. Eksp. Teor. Fiz. **33** (1957) 696, [Sov. Phys. JETP **6** (1958) 534].
- [9] J. Lindhard and M. Scharff, Phys. Rev. **124** (1961) 128.
- [10] J. Lindhard, M. Scharff and H. E. Schiøtt, K. Dan. Vidensk. Selsk. Mat. Fys. Medd. **33** (1963) 14.
- [11] P. Sigmund, Phys. Rev. **184** (1969) 383.
- [12] M. Benguerba, A. Brunelle, S. Della-Negra, J. Depauw, H. Joret, Y. Le Beyec, M. G. Blain, E. A. Schweikert, G. Ben Assayg and P. Sudraud, Nucl. Instr. and Meth. **B 62** (1991) 8.
- [13] I. Yamada, Mat. Chem. and Phys. **54** (1998) 5.
- [14] I. Yamada, J. Matsuo, N. Toyoda, T. Aoki, E. Jones and Z. Insepov, Mat. Sci. and Engnr. **A 253** (1998) 249.
- [15] I. Yamada, Nucl. Instr. and Meth. **B 148** (1999) 1.
- [16] M. Akizuki, J. Matsuo, W. Qin, T. Aoki, M. Harada, S. Ogasawara, K. Yodoshi and I. Yamada, Mat. Chem. and Phys. **54** (1998) 255.

- [17] W. Qin, R. P. Howson, M. Akizuki, J. Matsuo, G. Takaoka and I. Yamada, *Mat. Chem. and Phys.* **54** (1998) 258.
- [18] N. Toyoda, H. Hagiwara, J. Matsuo and I. Yamada, *Nucl. Instr. and Meth.* **B 148** (1999) 639.
- [19] N. Toyoda, H. Kitani, J. Matsuo and I. Yamada, *Mat. Chem. and Phys.* **54** (1998) 106.
- [20] N. Toyoda, H. Kitani, J. Matsuo and I. Yamada, *Nucl. Instr. and Meth.* **B 121** (1997) 484.
- [21] K. Goto, J. Matuo, T. Sugii, H. Minakata, I. Yamada and T. Hisatsugu, *IEDM Tech. Digst.* (1996) 435.
- [22] K. Goto, J. Matsuo, Y. Tada, Y. Momiyama, T. Sugii and I. Yamada, *IEDM Tech. Digst.* (1997) 471.
- [23] W. Brandt, A. Ratkowski and R. H. Ritchie, *Phys. Rev. Lett.* **33** (1974) 1325.
- [24] O. S. Oen, D. K. Holmes and M. T. Robinson, *J. Appl. Phys.* **34** (1963) 302.
- [25] M. T. Robinson and I. M. Torrens, *Phys. Rev. B* **9** (1974) 5008.
- [26] J. P. Biersack and L. G. Haggmark, *Nucl. Instr. and Meth.* **174** (1980) 257.
- [27] J. F. Ziegler, J. P. Biersack and U. Littmark, *The stopping and range of ions in solids* (Pergamon Press, New York, U.S.A, 1985).
- [28] B. J. Alder and T. E. Wainwrite, *J. Chem. Phys.* **27** (1957) 1208.
- [29] B. J. Alder and T. E. Wainwrite, *J. Chem. Phys.* **31** (1959) 459.
- [30] A. Rahman, *Phys. Rev.* **136** (1964) A405.
- [31] L. Verlet, *Phys. Rev.* **159** (1967) 98.
- [32] V. I. Shulga and P. Sigmund, *Nucl. Instr. and Meth.* **B 47** (1990) 236.
- [33] R. S. Averbach, T. Dias de la Rubia, H. Hsieh and R. Benedek, *Nucl. Instr. and Meth.* **B 59/60** (1991) 709.
- [34] Z. Insepov and B. Kabdiev, *NATO ASI Series B V 1* (1992) 429, (*Proc. of Intern. Conf. on Phys. and Chem. of Finite Systems: from Clusters to Crystals*).

- [35] M. Moseler, J. Nordiek, O. Rattunde and H. Haberland, *Rad. Eff. and Def. in Solids* **142** (1997) 39.
- [36] M. P. Allen and D. J. Tildesley, in *Computer Simulation of Liquids*, paperback ed. (Oxford Science Publications, New York, U.S.A., 1989), Chap. 3.
- [37] R. W. Hockney, *Methods Comput. Phys.* **9** (1970) 136.
- [38] D. Potter, *Computational Physics* (Wiley, New York, U.S.A., 1972).
- [39] F. H. Stillinger and T. A. Weber, *Phys. Rev. B* **31** (1985) 5632.
- [40] F. H. Stillinger and T. A. Weber, *J. Chem. Phys.* **88** (1988) 5123.
- [41] F. H. Stillinger and T. A. Weber, *Phys. Rev. Lett.* **62** (1989) 2144.
- [42] T. A. Weber and F. H. Stillinger, *J. Chem. Phys.* **92** (1990) 6239.
- [43] P. C. Weakliem, C. J. Wu and E. A. Carter, *Phys. Rev. Lett.* **69** (1992) 200.
- [44] J. Tersoff, *Phys. Rev. B* **39** (1989) 5566.
- [45] M. P. Allen and D. J. Tildesley, in *Computer Simulation of Liquids*, paperback ed. (Oxford Science Publications, New York, U.S.A., 1989), Chap. 9.
- [46] T. Munakata, *Statistical Physics (Toukei Butsuri-gaku)* (Asakura Shoten, Kyoto, JAPAN, 1996), in Japanese.
- [47] D. Takeuchi, K. Fukushima, J. Matsuo and I. Yamada, *Nucl. Instr. and Meth. B* **121** (1997) 493.
- [48] T. Seki, T. Kaneko, D. Takeuchi, T. Aoki, J. Matsuo, Z. Insepov and I. Yamada, *Nucl. Instr. and Meth. B* **121** (1997) 498.
- [49] D. Takeuchi, T. Seki, T. Aoki, J. Matsuo and I. Yamada, *Mat. Chem. and Phys.* **54** (1998) 76.
- [50] H. Feil, H. J. W. Zandvliet, M. H. Tsai, J. D. Dow and I. S. T. Tsong, *Phys. Rev. Lett.* **69** (1992) 3076.
- [51] J. Farges, M. de Feraudy, B. Raoult and G. Torchet, *J. Chem. Phys.* **78** (1983) 5067.
- [52] W. Miehe, O. Kandler, T. Leisner and O. Echt, *J. Chem. Phys.* **91** (1989) 5940.

- [53] M. J. Caturla, T. diaz de la Rubia and G. H. Gilmer, Nucl. Instr. and Meth. **B 196** (1995) 1.
- [54] M. Murty and H. A. Atwater, Phys. Rev. B **45** (1992) 1507.
- [55] N. Toyoda, H. Kitani, N. Hagiwara, T. Aoki, J. Matsuo and I. Yamada, Mat. Chem. and Phys. **54** (1998) 262.
- [56] J. Matsuo, N. Toyoda, M. Akizuki and I. Yamada, Nucl. Instr. and Meth. **B 121** (1997) 459.
- [57] S. R. Coon, W. F. Calaway and M. J. Pellin, Surf. Sci. **298** (1993) 161.
- [58] R. P. Webb, M. Kerford, M. Kapses and B. Brauchle, Nucl. Instr. and Meth. **B 122** (1997) 318.
- [59] A. Perez, M. Dobeli and H. A. Synal, Nucl. Instr. and Meth. **B 91** (1994) 187.
- [60] R. P. Webb, R. Smith, I. Chakarov and K. Beardmore, Nucl. Instr. and Meth. **B 112** (1996) 99.
- [61] R. Smith and K. Beardmore, Thin Solid Films **272** (1996) 255.
- [62] R. C. Morwrey, D. W. Brenner, B. I. Dunlap, J. W. Mintmire and C. T. White, Mat. Res. Soc. Symp. Proc. **206** (1991) 357.
- [63] M. Tanomura, D. Takeuchi, J. Matsuo, G. H. Takaoka and I. Yamada, Nucl. Instr. and Meth. **B 121** (1997) 480.
- [64] T. Seki, M. Tanomura, T. Aoki, J. Matsuo and I. Yamada, Mat. Res. Soc. Symp. Proc. **504** (1999) 93.
- [65] Semiconductor Industry Association, National Technology Road Map for Semiconductors (1997).
- [66] M. I. Current, D. Lopes, M. A. Foad, J. England, C. Jones and D. Su, J. Vac. Sci. Tech. **B16** (1998) 327.
- [67] S. Moffatt, Nucl. Instr. and Meth. **B 96** (1995) 1.
- [68] H. U. Jager, J. Appl. Phys. **78** (1995) 176.
- [69] K. S. Jones, P. G. Elliman, M. M. Petravic and P. Kringhoj, Appl. Phys. Lett. **68** (1996) 3111.
- [70] T. Kusaba, N. Shimada, J. Matsuo and I. Yamada, Proceeding of Ion Implantation Technology (1998) 1258.

- [71] K. Kanaya, K. Honjou, K. Koga and F. Toki, Jpn. J. Appl. Phys. **12** (1973) 1297.
- [72] T. A. Schoolcraft and B. J. Garrison, J. Vac. Sci. Tech. **A 8** (1990) 3496.
- [73] C. J. Wu and E. A. Carter, Phys. Rev. B **45** (1992) 9065.
- [74] V. I. Shulga and P. Sigmund, Nucl. Instr. and Meth. **B 62** (1991) 23.
- [75] C. L. Cleveland and U. Landman, Science **257** (1992) 355.
- [76] J. Nordiek and H. Moseler, Michael ad Haberland, Rad. Eff. and Def. in Solids **142** (1997) 27.
- [77] K. Nordlund, J. Keinonen, M. Ghaly and R. S. Averback, Nucl. Instr. and Meth. **B 148** (1999) 74.

List of Publications

Full Length Papers

1. T. Aoki, J. Matsuo, Z. Insepov and I. Yamada
“Molecular Dynamics Simulation of Damage Formation by Cluster Ion Impact”
Nucl. Instr. and Meth. **B 121** (1997) pp. 49–52.
2. T. Seki, T. Kaneko, D. Takeuchi, T. Aoki, J. Matsuo, G. H. Takaoka and I. Yamada
“STM Observation of HOPG Surfaces Irradiated with Ar Cluster Ions”
Nucl. Instr. and Meth. **B 121** (1997) pp. 498–502.
3. D. Takeuchi, T. Seki, T. Aoki, J. Matsuo and I. Yamada
“Cluster Ion Bombardment on Atomically Flat Au(111) Solid Surfaces”
Mat. Chem. and Phys. **54** (1998) pp. 76–79.
4. N. Shimada, T. Aoki, J. Matsuo, I. Yamada, K. Goto and T. Sugii
“Reduction of Boron Transient Enhanced Diffusion in Silicon by Low-Energy Cluster Ion Implantations”
Mat. Chem. and Phys. **54** (1998) pp. 80–83.
5. T. Aoki, T. Seki, J. Matsuo, Z. Insepov and I. Yamada
“Molecular Dynamics Simulation of a Carbon Cluster Ion Impacting on a Carbon Surface”
Mat. Chem. and Phys. **54** (1998) pp. 139–142.
6. T. Seki, T. Aoki, M. Tanomura, J. Matsuo and I. Yamada
“Energy Dependence of a Single Trace Created by C₆₀ Ion Impact”
Mat. Chem. and Phys. **54** (1998) pp. 143–146.
7. M. Akizuki, J. Matsuo, W. Qin, T. Aoki, M. Harada, S. Ogasawara, K. Yodoshi and I. Yamada
“Low-Temperature Formation of Perovskite PbTiO₃ Films by O₂

- Cluster Ion-Assisted Deposition” *Mat. Chem. and Phys.* **54** (1998) pp. 255–257.
8. N. Toyoda, H. Kitani, N. Hagiwara, T. Aoki, J. Matsuo and I. Yamada
“Angular Distributions of the Particles Sputtered with Ar Cluster Ions”
Mat. Chem. and Phys. **54** (1998) pp. 262–265.
 9. I. Yamada, J. Matsuo, N. Toyoda, T. Aoki, E. C. Jones and Z. Insepov
“Non-Linear Processes in the Gas Cluster Ion Beam Modification of Solid Surfaces”
Mat. Sci. and Engrn. **A 253** (1998) pp. 249–257.
 10. T. Aoki, T. Seki, J. Matsuo, Z. Insepov and I. Yamada
“Cluster Size Dependence of the Impact Process on a Carbon Substrate”
Nucl. Instr. and Meth. **B 153** (1999) pp. 264–269.
 11. I. Yamada, J. Matsuo, Z. Insepov, T. Aoki, T. Seki and N. Toyoda
“Nano-Processing with Gas Cluster Ion Beams”
Nucl. Instr. and Meth. to be published.
 12. T. Aoki, J. Matsuo and I. Yamada
“Molecular Dynamics Simulation of Fluorine Cluster Ion Impact”
Nucl. Instr. and Meth. to be published.

Proceedings

1. D. Takeuchi, T. Kaneko, T. Aoki, J. Matsuo and I. Yamada
“Nano Scale Modification by Cluster Ion Beams”
Proc. of the 5th Symp. on Intelligent Materials and the UK-Japan Seminar on Intelligent Materials (1996), pp. 119–121.
2. J. Matsuo, D. Takeuchi, T. Aoki and I. Yamada
“Cluster Ion Implantation for Shallow Junction Formation”
Proceeding of Ion Implantation Technology 1 (1996) pp. 772–775.
3. I. Yamada, J. Matsuo, N. Toyoda, T. Aoki, E. C. Jones and Z. Insepov
“Gas Cluster Ion Beam Processing”
Proc. of the 14th Intl. Conf. on Appl. of Accelerators in Research and Industry (1996) pp. 310–329.

4. T. Aoki, N. Shimada, D. Takeuchi, J. Matsuo, Z. Insepov and I. Yamada
 “The Molecular Dynamics Simulation of Boron Cluster Ion Implantation”
 IEICE Technical Report **96** No.396 (1996) pp. 49–54, in Japanese.
5. I. Yamada, J. Matsuo, E. C. Jones, D. Takeuchi, T. Aoki, K. Goto and T. Sugii
 “Range and Damage Distribution in Cluster Ion Implantation”
 Mat. Res. Soc. Symp. Proc. **438** (1997) pp. 363–374
6. J. Matsuo, T. Aoki, K. Goto, T. Sugii and I. Yamada
 “Ultra Shallow Junction Formation by Cluster Ion Implantation”
 Mat. Res. Soc. Symp. Proc. **532** (1998) pp. 17–22.
7. Z. Insepov, T. Aoki, J. Matsuo and I. Yamada
 “Computer Simulation of Annealing after Cluster Ion Implantation”
 Mat. Res. Soc. Symp. Proc. **532** (1998) pp. 147–152.
8. I. Yamada, J. Matsuo N. Toyoda and T. Aoki
 “Cluster Ion Implantation in Microelectronics Devices”
 Proc. of the 15th Intl. Conf. on Appl. of Accelerators in Research and Industry (1998) pp. 379–382.
9. J. Matsuo, N. Toyoda, M. Saito, T. Aoki, T. Seki and I. Yamada
 “Novel Analysis Techniques using Cluster Ion Beams”
 Proc. of the 15th Intl. Conf. on Appl. of Accelerators in Research and Industry (1998) pp. 429–432.
10. T. Aoki, T. Seki, M. Tanomura, J. Matsuo, Z. Insepov and I. Yamada
 “Molecular Dynamics Simulation of Fullerene Cluster Ion Impact”
 Mat. Res. Soc. Symp. Proc. **504** (1999) pp. 81–86.
11. T. Seki, M. Tanomura, T. Aoki, J. Matsuo and I. Yamada
 “Size Dependence of Bombardment Characteristics Produced by Cluster Ion Beams”
 Mat. Res. Soc. Symp. Proc. **504** (1999) pp. 93–98.
12. Z. Insepov, T. Aoki, J. Matsuo and I. Yamada
 “Computer Simulation of Decaborane Implantation and Rapid Thermal Annealing”
 Proceeding of Ion Implantation Technology (1999) pp. 807–810.
13. T. Aoki, J. Matsuo, Z. Insepov and I. Yamada
 “Molecular Dynamics Study of Implant and Damage Formation in

Low-Energy Boron Cluster Ion Implantation”
Proceeding of Ion Implantation Technology (1999) pp. 1254–1257.

International Conference

1. T. Aoki, J. Matsuo, Z. Insepov and I. Yamada
“Molecular Dynamics Simulation of Damage Formation by Cluster Ion Impact”
The Joint International Symposium of the '96 MRS-J Conference (Symp. N:‘Materials Synthesis and Modification by Ion and/or Laser Beam’) and the 3rd Ion Engineering Conference, Chiba, Japan, May 1996.
2. T. Aoki, J. Matsuo, Z. Insepov and I. Yamada
“Molecular Dynamics Simulation of a Carbon Cluster Ion Impacting on a Carbon Surface”
The 4th IUMRS International Conference in Asia (Symp. H:‘Materials Synthesis and Modification by Ion and/or Laser Beam’), Chiba, Japan, September 1997.
3. T. Aoki, T. Seki, J. Matsuo, Z. Insepov and I. Yamada
“Molecular Dynamics Simulation of Surface Modification Process by Cluster Ion Impact”
Conference of 1997 MRS Fall Meeting (Symp. KK:‘Atomistic Mechanisms in Beam Synthesis and Irradiation of Materials’), Boston, USA, December 1997.
4. T. Aoki, J. Matsuo, Z. Insepov and I. Yamada
“Molecular Dynamics Simulations of Low-energy Boron Cluster Ion Implantation”
The 12th International Conference on Ion Implantation Technology, Kyoto, Japan, June 1998.
5. T. Aoki, J. Matsuo, Z. Insepov and I. Yamada
“Molecular Dynamics Simulation Cluster Ion Impact for Surface Modification Process”
The 9th International Symposium on Small Particles and Inorganic Clusters, Lausanne, Switzerland, September 1998.
6. T. Aoki, T. Seki, J. Matsuo, Z. Insepov and I. Yamada
“Size Dependence on Non-linear Characteristics of Cluster Ion Impact by MD Simulations”
The 4th International Conference on Computer Simulation of Radiation Effects in Solids, Okayama, Japan, September 1998.

7. T. Aoki, J. Matsuo and I. Yamada
“Molecular Dynamics Simulation of Damage Formation and Sputtering by Cluster Ion Impact”
The 14th International Conference on Ion Beam Analysis, Dresden, Germany, July 1999.
8. T. Aoki, J. Matsuo and I. Yamada
“Molecular Dynamics Simulation of a Fluorine Cluster Ion Impact”
The 18th International Conference on Atomic Collisions in Solids, Odense, Denmark, August 1999.

Awards

1. Young Researcher Award
The 4th IUMRS International Conference in Asia, Chiba, Japan, September 1997.
2. Student Award
The 12th International Conference on Ion Implantation Technology, Kyoto, Japan, June 1998.